

Warming does not delay the start of autumnal leaf coloration but slows its progress rate

Nan Jiang

<https://orcid.org/0000-0001-5151-5715>

Miaogen Shen (✉ shen.miaogen@gmail.com)

Philippe Ciais

Matteo Campioli

Josep Peñuelas

Christian Körner

Ruyin Cao

Shilong Piao

Licong Liu

Shiping Wang

Eryuan Liang

Nicolas Delapierre

Kamel Soudani

Yuhan Rao

Leonardo Montagnani

Lukas Hörtnagl

Eugénie Paul-Limoges

Ranga Myneni

Georg Wohlfahrt

Yongshuo Fu

Ladislav Šigut

Andrej Varlagin

Jin Chen

Yanhong Tang

Wenwu Zhao

Research Article

Keywords: autumnal leaf senescence, global warming, leaf coloration onset, Northern Hemisphere, photoperiod

Posted Date: February 15th, 2022

DOI: <https://doi.org/10.21203/rs.3.rs-1352963/v1>

License:  This work is licensed under a Creative Commons Attribution 4.0 International License.

[Read Full License](#)

Version of Record: A version of this preprint was published at Global Ecology and Biogeography on August 14th, 2022. See the published version at <https://doi.org/10.1111/geb.13581>.

1 **Warming does not delay the start of autumnal leaf coloration but slows its progress rate**

2

3 **ABSTRACT**

4 **Aim:** Initiation of autumnal leaf senescence is critical for plant overwintering and ecosystem
5 dynamics. Previous studies focused solely on the advanced stages of autumnal leaf senescence
6 and claimed that climatic warming delays senescence, despite the fundamental differences
7 among the stages of senescence. However, the timing of onset of leaf coloration (D_{LCO}), the
8 earliest visual sign of senescence, has been rarely studied. Our aim is to assess the response of
9 D_{LCO} to temperature across the Northern Hemisphere.

10 **Location:** 30–75°N in the Northern Hemisphere.

11 **Time period:** 2000–2018.

12 **Major taxa studied:** Deciduous vegetation.

13 **Methods:** We retrieved D_{LCO} from high temporal-resolution satellite data, which was then
14 validated by PhenoCam observations. We then investigated the temporal changes in D_{LCO} and
15 the relationship between D_{LCO} and temperature by using D_{LCO} from satellite data and ground
16 phenological observations. We further estimated the timing of onset of autumnal decline in
17 maximum canopy photosynthetic capacity, an indicator of leaf senescence earlier than D_{LCO} ,
18 from FLUXNET CO₂ fluxes data, and assessed its response to temperature.

19 **Results:** D_{LCO} was not significantly ($P < 0.05$) delayed between 2000 and 2018 in 94% of the
20 area. D_{LCO} was positively correlated with pre- D_{LCO} mean daily minimum temperature (T_{min}) in
21 only 9% of the area, likely because of the overriding photoperiodic control, particularly for
22 woody vegetation, whereas the end of leaf coloration (D_{LCE}) was positively correlated with
23 pre- D_{LCE} mean T_{min} over a larger area (34%).

24 **Main conclusions:** The coloration progress rate is more sensitive than its start date to
25 temperature, indicating an extension of the duration of leaf senescence under warming. This
26 study indicates that the leaf coloration onset was not responsive to climate warming and
27 provides observational evidence of photoperiod control of autumnal leaf senescence at biome
28 and continental scales.

29

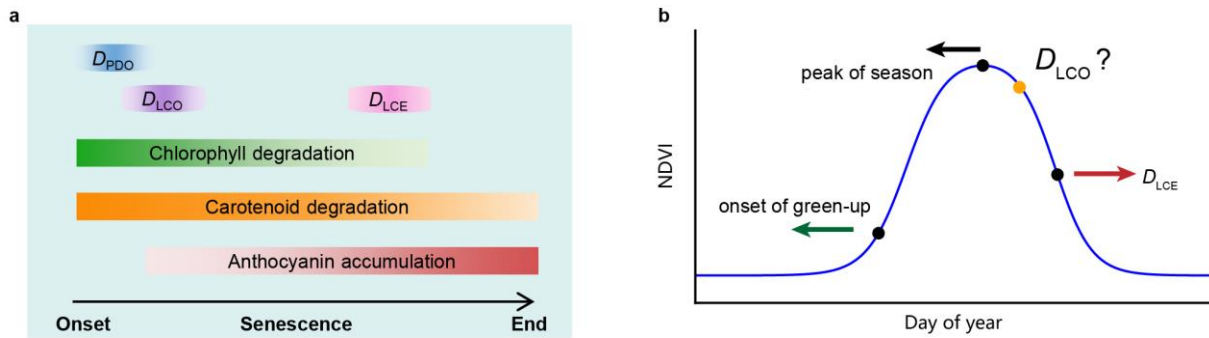
30 **Keywords:** autumnal leaf senescence, global warming, leaf coloration onset, Northern
31 Hemisphere, photoperiod

32

33 1 | INTRODUCTION

34 In contrast to the leaves of evergreen conifers, those of northern deciduous plants are not
35 sufficiently tolerant of freezing to survive cold periods and, therefore, are shed before the onset
36 of winter. This autumnal senescence process is controlled by changes in gene expression and
37 metabolic adjustments that include the degradation of macromolecules (e.g., chlorophyll), a
38 decrease in photosynthesis, and, importantly, the recycling and reallocation of nutrients (Thomas
39 & Stoddart, 1980; Gan & Amasino, 1997). Without timely leaf senescence and abscission, early
40 frost would lead to a loss of leaf resources. In parallel to leaf senescence, carbon sink activity
41 ceases progressively, and plants switch to nutrient recovery and resorption processes (Keskitalo
42 *et al.*, 2005; Estiarte & Peñuelas, 2015). Changes in the timing of key steps of leaf senescence
43 extensively influence ecosystem structure and functions, and this could further affect the climate
44 system (Peñuelas *et al.*, 2009; Richardson *et al.*, 2013). Senescence starts as a cryptic
45 phenological process before any visible symptoms become apparent (Körner & Basler, 2010).
46 The timing of the start of the leaf coloration following senescence varies, depending on the rate
47 of the senescence process, which is related to environmental conditions (e.g., temperature)
48 (Fracheboud *et al.*, 2009). Hence, the process of autumnal leaf senescence has two phases (Fig.
49 1a): (1) a visually indistinguishable ontogenetic stage that precedes (2) a visible change in leaf
50 color (Tang *et al.*, 2016). The timing of leaf coloration is the focus of *in situ* phenological
51 observations and has been the main concern of most autumnal phenological studies to date.

52



53

54 **Fig. 1** Conceptual graphs illustrating (a) the developmental processes in pigments during leaf
 55 senescence that are related to photosynthetic capacity and leaf color; and (b) phenological
 56 changes retrieved from normalized difference vegetation index (NDVI) data in the last few
 57 decades. In (a), D_{PDO} and D_{LCO} are the timings of the onsets of the decrease in maximum canopy
 58 photosynthetic capacity and leaf coloration in autumn, respectively; D_{LCE} is the timing of the
 59 end of leaf coloration. In (b) the onset of green-up corresponds to a 20% increase in NDVI, the
 60 peak of the season corresponds to the maximum NDVI, and D_{LCO} and D_{LCE} correspond to 10%
 61 and 50% decreases, respectively, in NDVI. The leftward and rightward arrows indicate advance
 62 of onset of green-up and peak of season and delay of D_{LCE} over the past few decades. The
 63 question mark indicates a research gap regarding temporal changes in D_{LCO} and their drivers.

64

65 Satellite and ground-based observations indicate that climate warming in the last several
 66 decades has substantially advanced the onset of spring green-up and the peak of the growing
 67 season, and it has slightly delayed the timing of the end of leaf coloration (D_{LCE} , the time when
 68 the normalized difference vegetation index [NDVI] decreases by 50% of its annual amplitude in
 69 the second half of a year in satellite-based studies (White *et al.*, 1997; Ganguly *et al.*, 2010;
 70 Nagai *et al.*, 2010; Yu *et al.*, 2010; Melaas *et al.*, 2013; Lukasová *et al.*, 2019)) in the Northern
 71 Hemisphere (Fig. 1b) (Jeganathan *et al.*, 2014; Fu *et al.*, 2015; Gill *et al.*, 2015; Xu *et al.*, 2016;
 72 Piao *et al.*, 2019; Menzel *et al.*, 2020). In addition to temperature, an increase in precipitation
 73 also delays D_{LCE} in temperate dry grasslands in the northern middle latitudes (Liu *et al.*, 2016).
 74 Besides these abiotic factors, temporal changes in D_{LCE} are also associated with the onset of
 75 green-up in some temperate tree species (Keenan & Richardson, 2015) and in boreal ecosystems

76 (Liu *et al.*, 2016). In contrast to D_{LCE} , the timing of onset of leaf coloration (D_{LCO}) has been
77 inadequately studied (Fig. 1b). In particular, it is not known whether D_{LCO} is sensitive to climate
78 and whether it has been responsive to recent climate change. D_{LCO} is of key importance because
79 it indicates when leaf senescence becomes apparent and its progress accelerates (Fig. 1b). As
80 shown by experiments on young trees, some temperate and boreal woody species use the
81 shortening of the photoperiod as a signal for the onset of leaf senescence (Table S1), but many
82 *in situ* and satellite observations indicate that increased temperature induces delays in the
83 advanced stages of senescence such as D_{LCE} (Estrella & Menzel, 2006; Delpierre *et al.*, 2009;
84 Jeong *et al.*, 2011; Ge *et al.*, 2015; Gill *et al.*, 2015; Liu *et al.*, 2016).

85 The dominant photoperiodic control of early senescence implies that D_{LCO} should not be
86 delayed, even if the temperature increases, because its timing is controlled only by daylength
87 (Hypothesis 1). On the other hand, without photoperiodic control, shifts in D_{LCO} are expected in
88 the case of climatic warming (Hypothesis 2). Alternatively, if D_{LCO} is influenced by both
89 photoperiod and temperature, the relationships between D_{LCO} and temperature should vary
90 among different areas because the strength of the photoperiod signal varies (Hypothesis 3). We
91 tested these hypotheses by investigating temporal changes in D_{LCO} and the interannual
92 relationships between D_{LCO} and pre- D_{LCO} T_{min} (the mean of monthly average daily minimum
93 temperature for an optimized period preceding D_{LCO}) for northern vegetation (30°N–75°N,
94 cropland pixels excluded) during the period 2000–2018. Since only a few *in situ* observational
95 programs or networks have monitored D_{LCO} , we determined D_{LCO} from a 5-day composite time
96 series of the NDVI derived from daily surface spectral reflectance (MOD09CMG) at a spatial
97 resolution of 0.05°, provided by the spaceborne Moderate Resolution Imaging
98 Spectroradiometer (MODIS) (Vermote, 2015). We defined D_{LCO} as the first date when daily
99 NDVI, fitted from 5-day NDVI, decreased by 10% of its annual amplitude during the
100 descending period of each year (Fig. 1b). To complement the NDVI data, we also used 332 time
101 series of D_{LCO} observed by professional observers according to standard observation guidelines
102 (China Meteorological Administration, 1993) in the field in China (Fig. S1a; Table S2) and the
103 timing of onset of autumnal decline in maximum canopy photosynthetic capacity (D_{PDO}) derived
104 from eddy covariance CO₂ flux observations (Gu *et al.*, 2009; Shen *et al.*, 2014) at 36 sites from

105 in the FLUXNET2015 dataset (Pastorello *et al.*, 2017) (Fig. S1b and Table S3).

106 **2 | MATERIALS AND METHODS**

107 **2.1 | D_{LCO} estimated from satellite observations of NDVI time series**

108 The NDVI is a proxy for vegetation greenness and has been widely used for phenological
109 studies at large spatial scales (Myneni *et al.*, 1997). NDVI has also been proved capable of
110 detecting the onset of leaf coloration (Soudani *et al.*, 2012; Yang *et al.*, 2014; Mariën *et al.*, 2019;
111 Soudani *et al.*, 2020; Zhao *et al.*, 2020). Previous studies have usually used half-month/16-day
112 composite NDVI time series to retrieve phenological metrics. However, because the color of
113 leaves often changes abruptly (Wang & Zhu, 2019), NDVI time-series data with higher temporal
114 resolution are required. We estimated phenological metrics (i.e., the timing of the onset and the
115 advanced stages of leaf coloration and the onset of green-up) for 2000–2018 from a 5-day
116 composite NDVI time series produced from the MODIS reflectance product (MOD09CMG
117 Collection 6, available at <https://ladsweb.modaps.eosdis.nasa.gov>, accessed on 29 January 2019)
118 (Vermote, 2015). MOD09CMG provides an estimate of daily surface spectral reflectance at a
119 spatial resolution of 0.05° . The quality of the daily surface reflectance data from MOD09CMG
120 is unsatisfactory owing to cloud and snow contamination (Vermote, 2015), so we used the 5-day
121 maximum value composite approach (Zhang, 2015), combined with a Savitzky-Golay filter
122 (Cao *et al.*, 2018), to produce a high-quality NDVI time series before determining D_{LCO} . First,
123 NDVI values that were lower than the uncontaminated winter (December–February) mean
124 NDVI were replaced by the latter (Beck *et al.*, 2006; Zhang *et al.*, 2007). After that,
125 cloud-contaminated and irregularly high and low NDVI values were identified and reconstructed
126 by using a Savitzky-Golay filter (Cao *et al.*, 2018). Details for preparing the high-quality NDVI
127 time series are given in Section 1 of the Supplementary Methods.

128 We focused on natural vegetation by excluding pixels dominated by cropland, artificial
129 surfaces, permanent snow or ice, and water bodies on the basis of the MODIS land-cover map
130 for the middle year of the time series (2009) (MCD12C1 Version 6) (Friedl & Sulla-Menashe,
131 2015) <https://ladsweb.modaps.eosdis.nasa.gov>, accessed on 20 August 2018). Some pixels were
132 also excluded from analysis because of sparse vegetation coverage, weak seasonality, or NDVI

133 peaking in October–April. We adopted three criteria for pixel exclusion: mean annual NDVI
134 must be > 0.10 , NDVI should peak between May and September in the multiyear mean NDVI
135 time series, and a pixel should be discarded if the mean NDVI for July and August is < 1.15
136 times the mean NDVI for December or for January–February in any year.

137 Two types of method can generally be used to estimate the parameters of vegetation
138 phenology (Chen *et al.*, 2016), including D_{LCO} from annual NDVI profiles. One is based on
139 thresholds (White *et al.*, 1997), whereas the other is based on inflection points (Zhang *et al.*,
140 2003). We applied the threshold-based method by first using a generalized sigmoid function to
141 fit the NDVI annual profile [Equation (7) in Klosterman *et al.* (2014)] and then determined D_{LCO}
142 as the first date when NDVI decreased by 10% of its annual amplitude in the descending period
143 (Leblans *et al.*, 2017; Richardson *et al.*, 2018). Though a smaller decrease in NDVI corresponds
144 to an earlier stage of leaf coloration, consideration of it would introduce more uncertainty. The
145 advanced stages of leaf coloration were determined as the dates when NDVI decreases by 20%,
146 30%, 40%, and 50% (corresponding to the timing of the end of leaf coloration, D_{LCE}),
147 respectively. We defined the timing of the onset of green-up as the date when NDVI increased
148 by 20% (Yu *et al.*, 2010). We also determined D_{LCO} by using the algorithm based on inflection
149 points owing to the slight difference between the methods for detecting phenological parameters.
150 We defined D_{LCO} as the date when the rate of change of the curvature of a double logistic
151 function (Beck *et al.*, 2006; Elmore *et al.*, 2012) fitted to the NDVI time series reached its first
152 local minimum in the descending period (Zhang *et al.*, 2003).

153 It is unreasonable to validate the satellite derived D_{LCO} by comparing it with D_{LCO} of a few
154 plant individuals from ground observation because of mismatch in spatial coverage, different
155 definitions of phenological metrics, and the spatial heterogeneity in phenological phases among
156 individuals for a pixel. Fortunately, pairs of field observations of NDVI and leaf coloration
157 showed well consistency between the start of NDVI decrease and leaf coloration onset (Soudani
158 *et al.*, 2012; Soudani *et al.*, 2020). Moreover, the comparison between start of autumn from
159 satellite observed NDVI and field observations of leaf coloration onset for the entire area
160 covered by the pixel also showed little difference between them (Zhao *et al.*, 2020). Those

161 studies suggest that NDVI is capable to detect the onset of leaf coloration if the observed leaves
162 or individuals are identical between ground and satellite observations. However, there are very
163 limited pairs of compatible observations of NDVI and leaf coloration that can be used for the
164 validation. Considering the high capability of PhenoCam in capturing the variations in leaf
165 coloration onset (Klosterman *et al.*, 2014; Wingate *et al.*, 2015; Klosterman & Richardson, 2017;
166 Nezval *et al.*, 2020), we used the PhenoCam Dataset V2.0 (Richardson *et al.*, 2018;
167 Seyednasrollah *et al.*, 2019a; Seyednasrollah *et al.*, 2019b) to assess the relationships between
168 satellite D_{LCO} and the D_{LCO} derived from GCC (green chromatic coordinate) and VCI
169 (vegetation contrast index) observed by PhenoCam (Section 2 of the Supplementary Methods).

170 **2.2 | D_{LCO} from *in situ* phenological observations**

171 D_{LCO} was extracted at the species level from datasets of *in situ* phenological observations
172 in China provided by the Chinese Academy of Sciences (CAS). The CAS dataset uses the date
173 of first leaf coloring as D_{LCO} . For a given species at a given site, the date of first leaf coloring
174 was identified as the day when the first batch (about 5%) of leaves on more than half of three to
175 five marked individuals started to change color (China Meteorological Administration, 1993).
176 The *in situ* phenological observations were performed according to standard observation
177 guidelines (China Meteorological Administration, 1993) every other day by professional
178 observers trained well by CAS. The CAS dataset is available from National Earth System
179 Science Data Sharing Infrastructure, National Science and Technology Infrastructure of China
180 (<http://www.geodata.cn>, accessed on 25 July 2018).

181 **2.3 | D_{PDO} estimated from maximum canopy photosynthetic capacity**

182 The timing of the onset of the decrease in maximum canopy photosynthetic capacity in
183 autumn (in day of year, D_{PDO}) is defined as the date when the capacity decreases by 10% of its
184 annual amplitude after the data have been fitted to a generalized sigmoid function [Equation (7)
185 in Klosterman *et al.*(2014)]. The capacity was calculated from half-hourly or hourly gross
186 primary productivity (GPP_NT_CUT_MEAN) based on eddy covariance measurements in the
187 FLUXNET2015 dataset (<http://fluxnet.fluxdata.org/data/fluxnet2015-dataset/>, accessed on 10
188 March 2018) (Pastorello *et al.*, 2017). We followed the procedure of Shen *et al.*(2014) to

189 estimate daily canopy photosynthetic capacity, except that the parameters in the rectangular
190 hyperbolic function were estimated by using half-hourly/hourly GPP and incident shortwave
191 radiation calculated by using 15-day moving windows throughout a year. We used data from the
192 sites in non-Mediterranean (Köppen-Geiger climate classification) and non-cultivated
193 (International Geosphere–Biosphere Programme classification) regions at middle and high
194 northern latitudes (30°N–75°N). In a similar way to the pixel exclusion process that was applied
195 to the satellite retrievals, we discarded sites where weak seasonality (i.e., the mean maximum
196 canopy photosynthesis for June–August was <1.15 times that for December or for January and
197 February) was detected in any year and sites where capacity did not peak in May–September.

198 **2.4 | Cold events before D_{LCO} (or D_{PDO})**

199 A sudden drop of nighttime temperature to the freezing point can induce leaf coloration in
200 a few days (Körner, 2007), and this could have interfered with our partial correlation analysis
201 between D_{LCO} (or D_{PDO}) and temperature. In our study, such sudden drops in temperature before
202 D_{LCO} (or D_{PDO}) that induce rapid leaf senescence, named cold events, were determined from
203 daily minimum air temperature (T_{min}). First, we determined the T_{min} threshold below which there
204 could potentially be a cold event for each pixel; this was the lowest T_{min} during the 6 to 35 days
205 before D_{LCO} for all years. If the lowest T_{min} was higher than 0 °C, the T_{min} threshold was set to
206 0 °C. Second, for a given pixel, a year was determined as a candidate cold event year if the
207 lowest T_{min} in the period 1 to 5 days before D_{LCO} was lower than the above-mentioned T_{min}
208 threshold. Then, from the years that were not candidate cold event years, we determined the
209 latest D_{LCO} that was not caused by a cold event for that pixel. Finally, a D_{LCO} was recognized as
210 caused by a cold event if it was both in the candidate cold event years and earlier than the latest
211 D_{LCO} that was not caused by a cold event. This empirical approach may have overestimated the
212 number of years with cold events before D_{LCO} , but our objective was to exclude as many cold
213 events as possible. On clear nights, the temperature of the canopy surface could be lower than
214 the air temperature, so we also evaluated the first step by using 2 °C as the T_{min} threshold. The
215 cold events for *in situ* D_{LCO} and D_{PDO} were determined similarly. The cold event years accounted
216 for a very small fraction of years with phenological data (Table S4).

217 Here, the daily minimum temperature used to determine cold events for satellite-derived
218 D_{LCO} was extracted from the CRU-NCEP dataset (Version 7.2, <https://vesg.ipsl.upmc.fr>,
219 assessed on 10 January 2019), which provides 6-hourly data at a spatial resolution of $0.5^\circ \times 0.5^\circ$
220 through 2016 (Viovy, 2018). The CRU-NCEP 7.2 is a combination of two datasets: the CRU
221 TS3.2 $0.5^\circ \times 0.5^\circ$ monthly data covering the period 1901 to 2002 and the NCEP reanalysis 2.5°
222 $\times 2.5^\circ$ 6-hourly data covering the period 1948 to 2016. We determined daily T_{\min} as the
223 minimum value of the four 6-hourly minimum temperature values for each day. The
224 CRU-NCEP data were resampled at $0.05^\circ \times 0.05^\circ$ by replication to match the D_{LCO} data. Daily
225 T_{\min} for *in situ* observations in China was extracted from the “Daily Surface Climate Variables
226 of China” catalog (a dataset named SURF_CLI_CHN_MUL_DAY_V3.0), which includes daily
227 climate data for 2474 sites in China from January 1951 to July 2014, provided by the Chinese
228 Meteorological Administration via an offline request on 18 January 2015. The distance between
229 phenological and meteorological stations was less than 25 km. Daily T_{\min} for D_{PDO} was
230 calculated from the half-hourly temperature dataset provided by FLUXNET2015.

231 2.5 | Analyses

232 Temporal trends in D_{LCO} were quantified as the slopes of linear regressions between a
233 variable and year by using OLSR. To complement the temporal changes assessed by using
234 OLSR, a non-parametric approach (the Theil-Sen estimator (Sen, 1968; Theil, 1992)) was also
235 used to calculate the trends in D_{LCO} . The temporal trend was calculated for each time series for
236 the ground-based observations and for each pixel for the satellite observations. We focused only
237 on the temporal trends for the pixels and time series of *in situ* phenological observations with a
238 multiyear mean of D_{LCO} occurring after the summer solstice. Phenological records were not
239 available for some of the years of the time series for calculating more trends or correlations,
240 because the time series may have had missing values owing to a lack of observation. However,
241 the time series used for the regressions contained at least 10 years of observational records and
242 at least one record for any 3 consecutive years. If two or more parts of the time series met these
243 criteria, the most recent part was used.

244 T_{\min} has long been recognized as the indicator of the thermal condition that induces
245 autumnal leaf coloration (Tang *et al.*, 2016). We investigated the impacts of temperature and
246 precipitation, respectively, on the satellite-derived D_{LCO} by calculating the R_{TN} values between

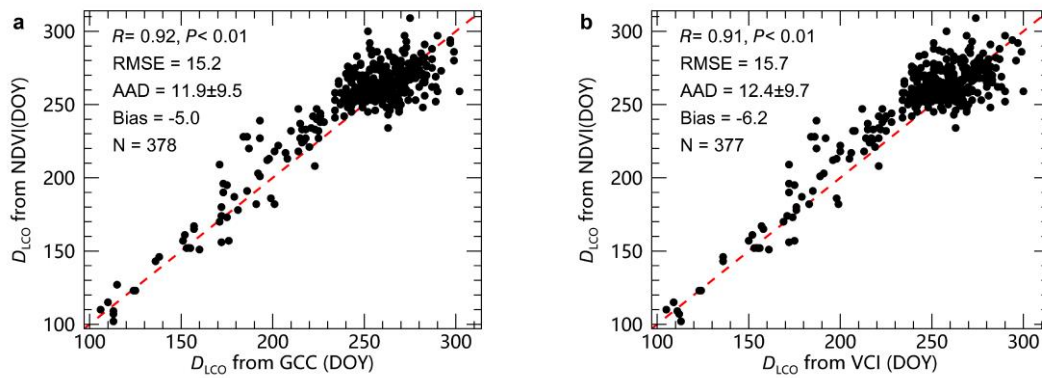
247 D_{LCO} and the mean of monthly average daily minimum temperature (T_{min}) for the pre- D_{LCO}
248 period, with concurrent total precipitation as the control variable, and between D_{LCO} and
249 pre- D_{LCO} total precipitation (R_{PRE}), with concurrent T_{min} as the control variable for 2000–2018.
250 The pre- D_{LCO} period for T_{min} (Fig. S2) was defined as the period preceding the multiyear mean
251 D_{LCO} for which T_{min} had the strongest interannual partial correlation with D_{LCO} , with concurrent
252 total precipitation as a control variable. The candidate period had the earliest start in June and a
253 fixed end at the multiyear mean D_{LCO} , at steps of 1 month. If the multiyear mean D_{LCO} was in
254 the first half of a month, then the pre- D_{LCO} period ended at the month preceding the multiyear
255 mean D_{LCO} . Otherwise, the pre- D_{LCO} period ended at the month of the multiyear mean D_{LCO} .
256 The pre- D_{LCO} period for precipitation was defined similarly. The impacts of climatic factors on
257 the advanced stages of leaf coloration were investigated similarly. The data for T_{min} and
258 precipitation were extracted from the Climatic Research Unit (CRU) Time-Series (TS) 4.03
259 dataset (<http://data.ceda.ac.uk>, accessed on 11 June 2019), which provided monthly data at a
260 spatial resolution of $0.5^\circ \times 0.5^\circ$ until 2018. It should be noted that T_{min} in the dataset is an
261 approximation of the mean of daily minimum temperature for a calendar month, which is
262 arithmetically calculated from gridded monthly mean temperature and the diurnal temperature
263 range (Harris *et al.*, 2014) and does not exactly reflect the interannual variations in the absolute
264 minimum temperature (Körner & Hiltbrunner, 2018) experienced by plants before D_{LCO} . The
265 CRU data were resampled at $0.05^\circ \times 0.05^\circ$ by replication to match the D_{LCO} data. We also
266 investigated the impact of T_{min} and precipitation on D_{LCO} from ground-based observations in
267 China and on D_{PDO} from eddy-covariance sites as complementary to satellite-derived of D_{LCO} .
268 Climatic data from the nearest meteorological station (<25 km), provided by the Chinese
269 Meteorological Administration, were used for *in situ* D_{LCO} in China.

270 **3 | RESULTS**

271 **3.1 | Comparison of satellite D_{LCO} with PhenoCam D_{LCO}**

272 The satellite D_{LCO} explained about 80% of the variations in PhenoCam derived D_{LCO} ($N =$
273 378 and 377 for GCC and VCI) (Fig. 2). The difference between the satellite D_{LCO} and the
274 PhenoCam D_{LCO} are caused by the mismatch between the annual NDVI and GCC (or VCI)
275 trajectories due to difference in spatial coverage between the PhenoCam and satellite pixel in the

276 cases of phenologically heterogeneous land surface (Zhang *et al.*, 2018).



277

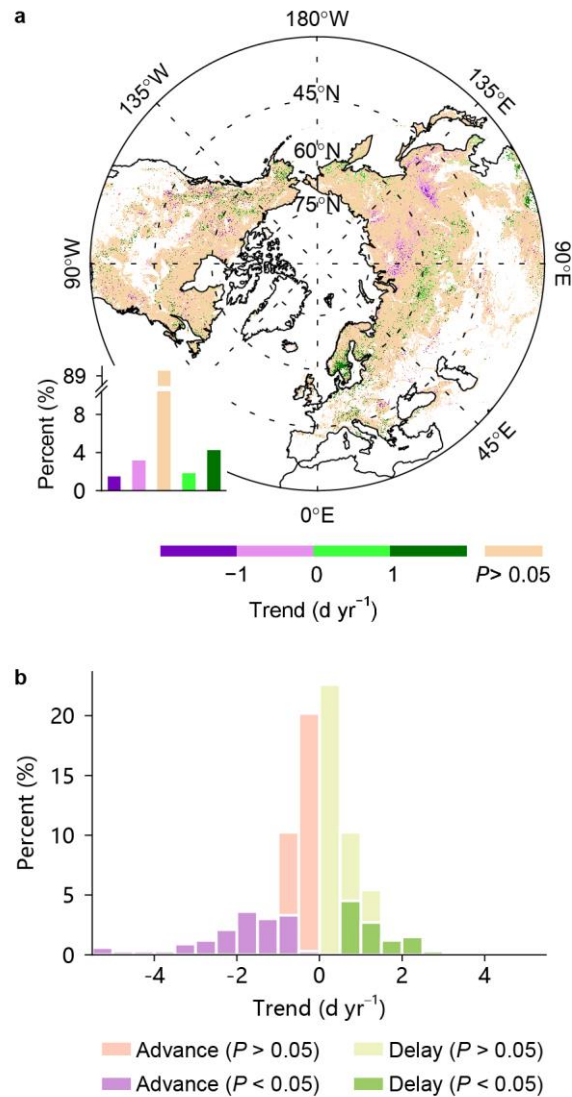
278 **Fig. 2** Comparison between satellite D_{LCO} and PhenoCam D_{LCO} . The PhenoCam D_{LCO} was
279 determined from GCC (a) and VCI (b), respectively. R : Pearson's correlation coefficient; RMSE:
280 root mean square error; AAD: average absolute difference; bias is defined as the difference
281 between the mean of satellite D_{LCO} and the mean of PhenoCam D_{LCO} , and negative bias means
282 the PhenoCam D_{LCO} is earlier than satellite D_{LCO} .

283

284 3.2 | Temporal trends in D_{LCO}

285 D_{LCO} was not significantly delayed in 94% of the area during the study period, as assessed
286 by ordinary least squares regression (OLSR) between satellite-derived D_{LCO} and respective years.
287 The few pixels with a significant delay trend (6%; $P < 0.05$, t -test) were scattered across the
288 Northern Hemisphere (Fig. 3a). Leaf color often changes rapidly owing to cold events in autumn;
289 these rapid changes introduced noise to the D_{LCO} time series and trends. Excluding years with
290 cold events before D_{LCO} produced similar results (Fig. S3 and Table S5). Because the sample
291 size (i.e., the number of years in the D_{LCO} time series) for calculating the trend was small, we
292 also used the Theil-Sen estimator to determine temporal D_{LCO} trends. This method generated
293 results supporting the lack of changes in D_{LCO} (no significant delay in 96% of the area; $P < 0.05$,
294 Mann-Kendall test; Fig. S4a and Table S6). When we redefined D_{LCO} as the date when the rate
295 of change of curvature of a double logistic curve (Beck *et al.*, 2006) fitted to the NDVI series
296 reached its first local minimum in the descending period (Zhang *et al.*, 2003), we obtained
297 similar results (Fig. S4b and c). Complementary to satellite-derived D_{LCO} , we also examined the
298 temporal changes of D_{LCO} by using ground-based leaf coloration data from China. D_{LCO} was not

299 significantly delayed for 90% and 94% of the 332 time series as shown by OLSR (Fig. 3b) and
 300 the Theil-Sen method (Table S6), respectively. As with the remotely sensed data, excluding cold
 301 events from the ground-based data revealed only a few significant delays of D_{LCO} (Table S5).
 302



303

304 **Fig. 3** Temporal trends in the timing of the onset of leaf coloration (D_{LCO}), as retrieved from
 305 satellite and *in situ* observations. a, Satellite-derived D_{LCO} trends over 2000–2018. The bar chart
 306 in the bottom-left corner shows the percentage of area within each interval of the significant
 307 temporal trends and the percentage of area with nonsignificant trends, indicated by the color
 308 scale at the bottom. Positive and negative trend values refer to significantly delayed and
 309 advanced D_{LCO} , respectively. D_{LCO} is defined as the date when NDVI decreases by 10% of its

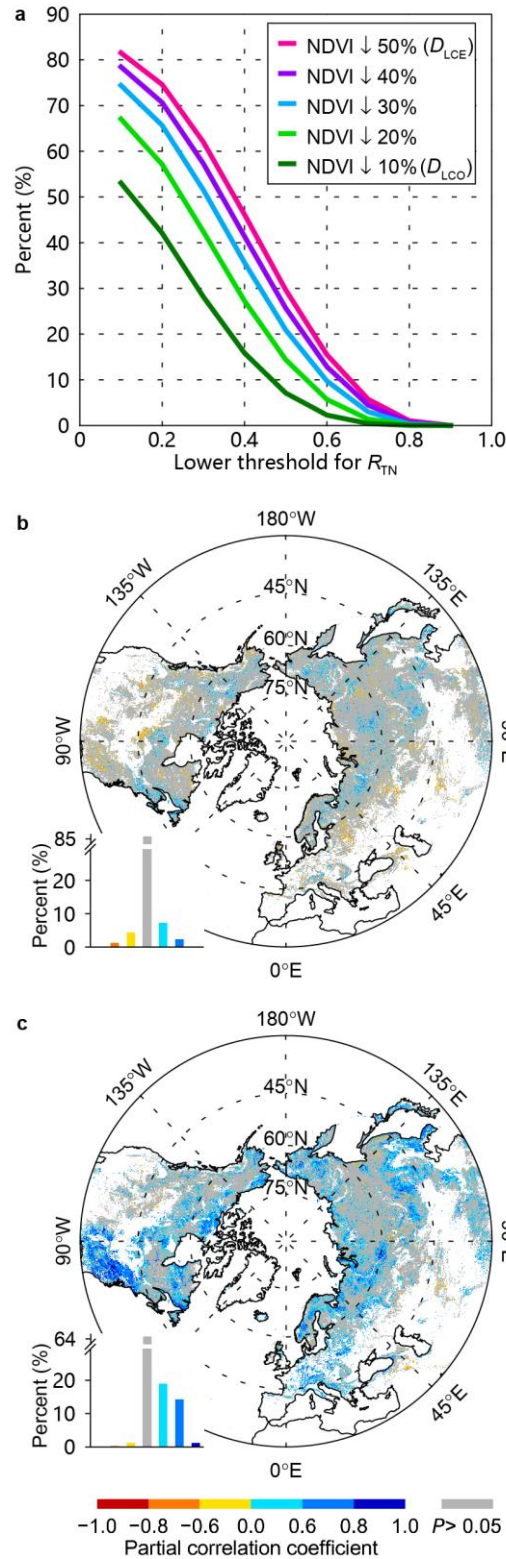
310 annual amplitude in autumn, based on a generalized sigmoid function fitted from the annual
311 NDVI profile. Pixels dominated by croplands or with low vegetation coverage, weak seasonality,
312 or peak NDVI in October–April were discarded. b, Ground-observed D_{LCO} trends derived over
313 1971–1997 from *in situ* leaf coloration observations in China. Significant temporal trends were
314 determined by using *t*-tests at $P < 0.05$ and OLSR between D_{LCO} and respective years.

315

316 **3.3 | Correlation between D_{LCO} and temperature**

317 With the same data that were used for D_{LCO} assessment, we verified that a delay in D_{LCE}
318 was correlated with an increase in temperature for the period preceding D_{LCE} (Estrella & Menzel,
319 2006; Delpierre *et al.*, 2009; Gill *et al.*, 2015; Liu *et al.*, 2016; Fu *et al.*, 2018) (Fig. 4a and c). In
320 addition, since in a few studies (Ren *et al.*, 2017; Berman *et al.*, 2020), end of leaf coloration was
321 defined as the dates when NDVI drops by 60% or 90% of its annual amplitude, we also
322 calculated the partial correlations between each of those dates and the temperature, respectively,
323 and the correlations were similar to the that between D_{LCE} and the pre- D_{LCE} temperature (Fig.
324 S5). D_{LCO} , however, was not correlated with pre- D_{LCO} T_{min} , with only 9% of the area in scattered
325 pixels showing a significant positive correlation and 5% showing a significant negative
326 correlation (Fig. 4b). D_{LCO} was positively partially correlated with pre- D_{LCO} total precipitation
327 in 13% of the area, mainly in the temperate grassland of Northern America and in the middle
328 latitudes of Eurasia, sub-arctic grassland, and alpine steppe of the Tibetan Plateau (Fig. S6).
329 Therefore, neither pre- D_{LCO} T_{min} nor precipitation was a useful predictor of D_{LCO} in most areas.
330 We obtained similar results when using a pre- D_{LCO} period with a fixed length (1 month
331 preceding D_{LCO}) to calculate pre- D_{LCO} T_{min} (Fig. S7). Moreover, a shorter pre- D_{LCO} period (15
332 days preceding D_{LCO}) showed similar results, with only 5% of the area showing a significant
333 positive correlation between D_{LCO} and pre- D_{LCO} T_{min} (Fig. S8). We also investigated the
334 relationship between D_{LCO} and the lowest daily minimum temperature during the 15 days before
335 the multiyear mean D_{LCO} . We found that only 3% of the area showed a significant positive
336 correlation (Fig. S9). A few studies have suggested that the date of onset of green-up may affect
337 leaf coloration through legacy effects (Fu *et al.*, 2014; Keenan & Richardson, 2015; Liu *et al.*,
338 2016), but including this date as an extra control variable in the partial correlation analyses did

339 not affect the results (Fig. S10). The *in situ* phenological records in China indicated that
340 ground-observed D_{LCO} was positively partially correlated with pre- $D_{LCO} T_{min}$ for 13% of the time
341 series and was not correlated with pre- $D_{LCO} T_{min}$ for 82% of the time series (Table 1). Excluding
342 D_{LCO} caused by cold events produced similar results (Fig. S11 and Table S7). Overall, these
343 results suggest that an increase in pre- $D_{LCO} T_{min}$ is not likely to delay D_{LCO} in most areas in the
344 middle and high northern latitudes.



345

346 **Fig. 4** Relationships between the timing of different stages of leaf coloration (retrieved from
 347 satellite images) and the mean daily minimum temperature (T_{min}) for an optimized period
 348 preceding the respective stage over the period 2000–2018. a, Percentage of area for which the
 349 partial correlation coefficient (R_{TN}) between the timing of a given stage of leaf coloration

350 (defined by NDVI decrease) and T_{\min} for an optimized period preceding the stage is higher than
 351 a given threshold indicated by the horizontal axis. For example, R_{TN} for the onset of leaf
 352 coloration (D_{LCO} , 10% decrease in NDVI) is higher than 0.2 in about 40% of the area. b, Spatial
 353 pattern of the partial correlation coefficient between D_{LCO} and pre- D_{LCO} T_{\min} . c, Spatial pattern
 354 of the partial correlation coefficient between timing of the end of leaf coloration (D_{LCE} , 50%
 355 decrease in NDVI) and pre- D_{LCE} T_{\min} . The bar charts in (b) and (c) show the percentage of area
 356 for each interval of the partial correlation coefficient ($P < 0.05$), with the coefficient indicated
 357 by the color scale at the bottom. Non-significant correlations ($P > 0.05$) are in gray. Pixels
 358 dominated by croplands or with low vegetation coverage, weak seasonality, or peak NDVI in
 359 October–April were discarded.

360
 361 **Table 1.** Percentage of correlations between D_{LCO} or D_{PDO} and each climate factor for each
 362 interval of the partial correlation coefficient.

Metric	Number of time series	Climate factor	Interval of the partial correlation coefficient ($P < 0.05$)						$P > 0.05$
			[-1.0, -0.8]	[-0.8, -0.6]	[-0.6, 0]	(0, 0.6]	(0.6, 0.8]	(0.8, 1.0]	
<i>in situ</i> D_{LCO}	332	Temperature	0	2	3	4	8	1	82
China		Precipitation	0	3	3	4	5	0	85
FLUXNET2015	36	Temperature	0	5	3	0	3	0	89
D_{PDO}		Precipitation	0	6	0	8	3	5	78

363 D_{PDO} , timing of the onset of the decrease in maximum canopy photosynthetic capacity in autumn; D_{LCO} , timing of
 364 the onset of leaf coloration in autumn. The relationships between D_{LCO} (or D_{PDO}) and temperature were determined
 365 by using a partial correlation analysis between D_{LCO} (or D_{PDO}) and pre- D_{LCO} (or pre- D_{PDO}) mean daily minimum
 366 temperature, with concurrent total precipitation as the control variable. The relationships between D_{LCO} (or D_{PDO})
 367 and pre- D_{LCO} (or pre- D_{PDO}) precipitation were determined similarly. The data in the farthest right column indicate
 368 the percentages of area or time series with non-significant correlations.

369
 370 In previous analyses of *in situ* and satellite observations (Garonna *et al.*, 2014; Gill *et al.*,
 371 2015; Liu *et al.*, 2016), the advanced stage of autumnal leaf senescence, indicated by D_{LCE} , was
 372 significantly delayed in a larger proportion of areas, or time series, than was D_{LCO} in our study.

373 In the current study, D_{LCE} was also significantly delayed in more areas than D_{LCO} (Fig. S12),
374 probably because the timings of the earlier stages of leaf coloration determined from satellite
375 data were less affected by T_{min} than the later stages (Fig. 4a and Fig. S13). Evidence for
376 photoperiodic control of the start of leaf senescence (Keskitalo *et al.*, 2005; Fracheboud *et al.*,
377 2009) suggests that the early phases of leaf senescence are insensitive to warming, in contrast to
378 the later phases. Since the degradation of chlorophyll starts earlier than leaf coloration (Lim *et*
379 *al.*, 2007; Tang *et al.*, 2016), the timing of autumnal phenological metrics that closely follow
380 chlorophyll degradation before D_{LCO} should be less delayed by temperature increase than D_{LCO}
381 if chlorophyll degradation is triggered by the photoperiod. To test this deduction, we analyzed
382 the relationship between D_{PDO} in autumn and pre- D_{PDO} T_{min} (determined in a similar way to
383 pre- D_{LCO} T_{min}), since D_{PDO} is notably strongly controlled by chlorophyll concentration. Indeed,
384 D_{PDO} was positively correlated with pre- D_{PDO} T_{min} in 3% of the 36 eddy-covariance towers and
385 was not correlated with pre- D_{PDO} T_{min} in 89% of the eddy-covariance records (Table 1).
386 Excluding D_{PDO} caused by cold events produced similar results (Table S7). Moreover, D_{PDO} and
387 pre- D_{PDO} T_{min} were less positively correlated than were NDVI-derived D_{LCO} and pre- D_{LCO} T_{min}
388 at the same sites during the same periods (3% and 6% of the sites for D_{PDO} and D_{LCO} ,
389 respectively, Table S8), probably because the start of autumnal chlorophyll degradation was
390 controlled by photoperiod and was not delayed by higher temperature (Keskitalo *et al.*, 2005;
391 Fracheboud *et al.*, 2009; Bauerle *et al.*, 2012).

392 4 | DISCUSSION

393 4.1 | Whether summer NDVI decline contributed to the absence of D_{LCO} delay and 394 D_{LCO} -temperature relationship

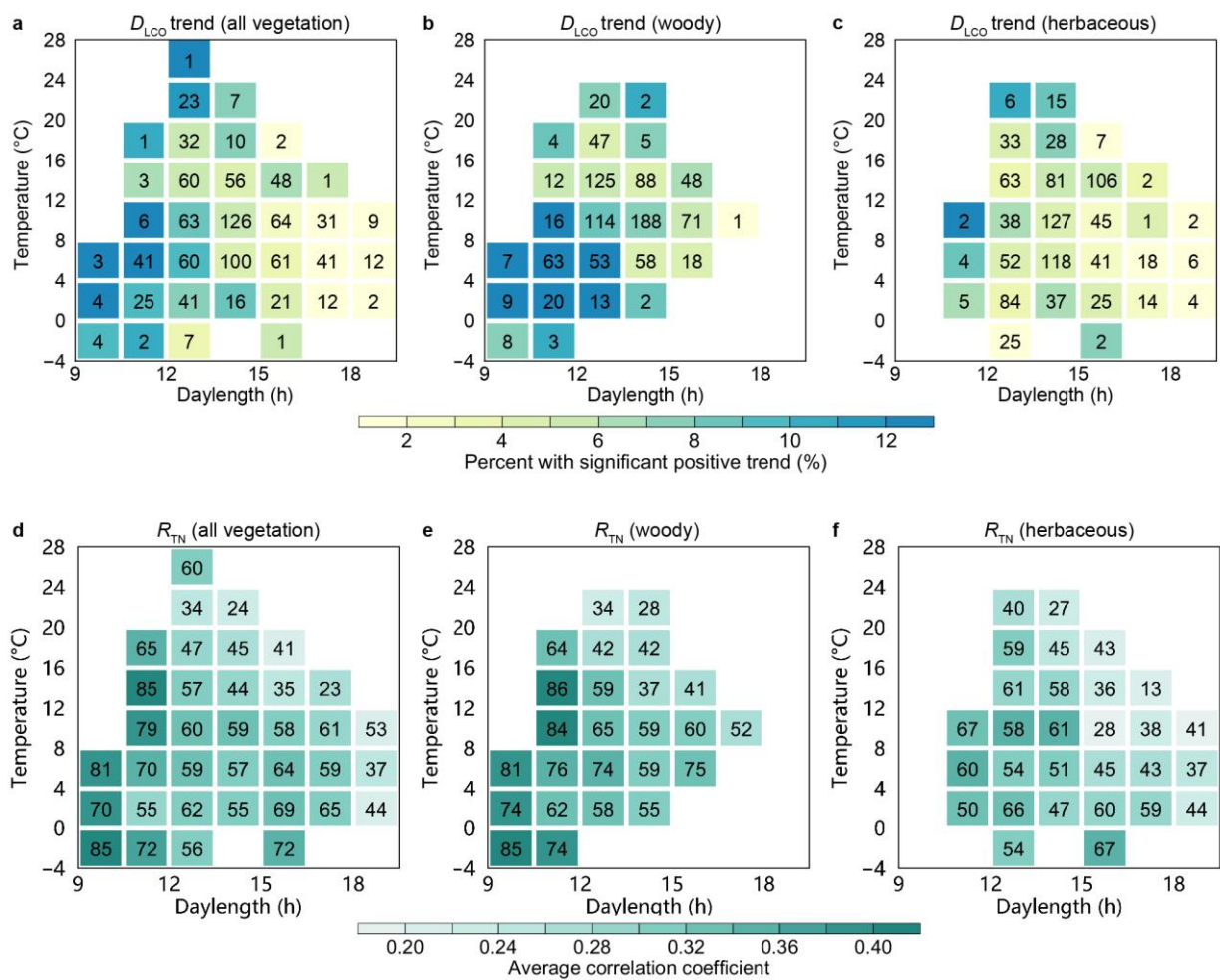
395 Our findings are mainly based on D_{LCO} determined on the annual trajectory of NDVI. In
396 some deciduous forest, NDVI may decline in early summer (i.e., late May–July) before leaf
397 coloration, and this may potentially interfere with the determination of D_{LCO} to some extent
398 (Elmore *et al.*, 2012). To test whether early summer NDVI decline would affect the results in
399 our study, for the pixels classified as deciduous broadleaf forest in the MODIS land-cover
400 product in 2009, we redefined independently D_{LCO} in three different ways: (1) We used a
401 modified double logistic model that considers early summer NDVI decline (Elmore *et al.*, 2012)

402 to fit the NDVI time series instead of the original double logistic function for the pixels
403 classified as deciduous broadleaf forest. D_{LCO} was then determined as the date when the rate of
404 change of the curvature of a double logistic function fitted to the NDVI time series reached its
405 first local minimum in the descending period; (2) D_{LCO} was defined as the date when NDVI
406 decreased by 10% of its annual amplitude from 1 August. The maximum value used to
407 determine the annual amplitude was the mean value of the upper quartile of the fitted NDVI
408 values in August; and (3) D_{LCO} was defined as the date when NDVI decreased by 10% of its
409 annual amplitude from 16 August. The maximum value used to determine the annual amplitude
410 was the mean value of the upper quartile of the fitted NDVI values in the second half of August.
411 The results with deciduous broadleaf forest pixels redefined in these three ways (Figs. S14–S22)
412 were similar to those calculated without considering the effect of early summer NDVI decline
413 (Figs. 3–6; Fig. S4).

414 **4.2 | Dependence of leaf senescence on daylength**

415 Overall, these results suggest that temperature does not initiate senescence in autumn in
416 most areas; rather, it influences the speed of senescence after it starts (Fracheboud *et al.*, 2009).
417 The lack of a positive correlation between D_{LCO} (or D_{PDO}) and pre- D_{LCO} (or pre- D_{PDO})
418 temperature suggests an overriding photoperiodic control that makes the timing of the onset of
419 leaf senescence stable. In the areas with longer daylengths (calculated for each pixel/location at
420 multiyear mean D_{LCO} over 2000–2018), there were proportionally fewer significant D_{LCO} delays
421 during 2000–2018 (Fig. 5a and Fig. S23a), and the positive relationship between D_{LCO} and
422 pre- D_{LCO} T_{min} was slightly weaker, as indicated by the smaller partial correlation coefficient
423 between them (Fig. 5d). Such patterns were more prominent for woody vegetation than for
424 herbaceous vegetation (Fig. 5b, c, e and f; Fig. S23b and c), in agreement with experimental
425 findings suggesting that the initiation of leaf senescence in woody plants is likely controlled by
426 photoperiod (Keskitalo *et al.*, 2005; Fracheboud *et al.*, 2009). These findings indicate stronger
427 photoperiodic control in areas where daylength at D_{LCO} is longer (i.e., shorter nights), possibly
428 because plants respond to the length of uninterrupted darkness rather than daylength (Hamner,
429 1940; Borthwick & Hendricks, 1960; Paus *et al.*, 1986; Howe *et al.*, 1995). Interestingly, for
430 vegetation with a daylength at D_{LCO} of more than 13.5 h, D_{LCO} was more positively correlated

431 with pre- D_{LCO} T_{min} in colder areas at a given daylength (Fig. 5d–f), indicating a stronger effect
 432 of temperature in areas with harsh temperature conditions, consistent with experimental studies
 433 (Zohner *et al.*, 2016; Ford *et al.*, 2017). Therefore, although for these types of vegetation the
 434 correlation between D_{LCO} and temperature is weak, probably because of stronger photoperiodic
 435 control, there is still a signal of temperature influence on D_{LCO} , reflecting a stronger selection
 436 pressure in harsher temperature environments. The correlation between D_{LCO} and pre- D_{LCO} total
 437 precipitation was independent of photoperiod and was slightly stronger for the areas with a
 438 higher daily minimum temperature before D_{LCO} , mostly because of the stronger effect of
 439 precipitation in delaying D_{LCO} in herbaceous vegetation (Figs. S5 and S24). The dependences of
 440 D_{LCO} trends on photoperiod and of the correlation between D_{LCO} and pre- D_{LCO} T_{min} on
 441 photoperiod were also found when years with cold events before D_{LCO} were excluded (Fig.
 442 S25).



443
 444 **Fig. 5** Dependence of temporal trends in the timing of the onset of leaf coloration (D_{LCO} , a–c)

445 and of the partial correlation coefficient (R_{TN} , d–f) between D_{LCO} and pre- D_{LCO} mean daily
446 minimum temperature (T_{min}) on daylength and temperature at D_{LCO} over the period 2000–2018.
447 Daylength (indicated by the horizontal axis) was calculated for each pixel (location) at multiyear
448 mean D_{LCO} over 2000–2018 ($D_{LCO-MEAN}$), and temperature (indicated by the vertical axis) is the
449 mean of daily minimum temperature in the month preceding $D_{LCO-MEAN}$. a, All vegetation. Color
450 indicates the percentage of area with significant ($P < 0.05$) D_{LCO} delays in each cell (i.e., a
451 specific temperature \times daylength combination), as indicated in the scale at the bottom. The
452 number in each cell indicates the ratio (unit: %) of the area in each cell to the total area with
453 D_{LCO} retrieval (i.e., Northern Hemisphere from 30°N–75°N). The temporal trends and their
454 significances were determined with ordinary least squares regression and t -tests. b and c, The
455 same as (a) but for woody and herbaceous vegetation, respectively. d, All vegetation. Color
456 indicates the average of the positive R_{TN} , as indicated in the scale at the bottom. The number in
457 each cell indicates the percentage of area with a positive correlation in each cell. e and f, The
458 same as (d) but for woody and herbaceous vegetation, respectively. Each cell represents 4 °C of
459 temperature and 1.5 h of daylength. Only cells where the ratio of the area of the cell to the total
460 area is $>1\%$ are represented. Woody and herbaceous vegetation are merged from Classes 1–6
461 and Class 10, respectively, in the MODIS land-cover product (MCD12C1, Version 6) for 2009.

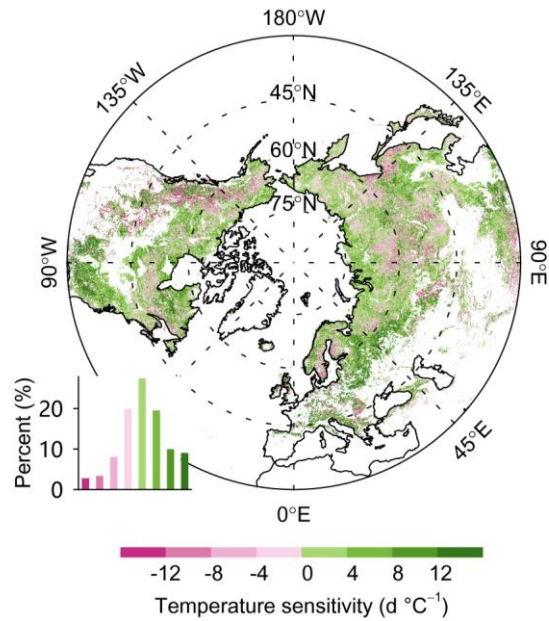
462

463 Although observational evidence is limited, experimental results have been reported for
464 the photoperiodic induction of leaf senescence in several, mostly woody, species (Table S1).
465 However, in those manipulative experiments, daylength was altered by several hours (>4 h,
466 Table S1), which is more extreme than the natural conditions plants are likely to experience.
467 Daylength depends only on the day of year and location. Because of the inter-annual limited
468 variations in the timings of leaf coloration or senescence onset, the fluctuation in daylength
469 under natural conditions is far less than that in manipulative experiments. Therefore, the role of
470 photoperiod in leaf senescence identified under such experimental conditions does not
471 necessarily apply to plants under natural conditions. The results in this study support
472 experimental findings in wild plants at the biome and continental scales and show that

473 photoperiod influences the onset of leaf coloration, which closely follows the initial of leaf
474 senescence.

475 **4.3 | Implications**

476 Autumnal leaf senescence in preparation for overwintering is an evolutionary trade-off
477 between the reallocation of leaf nutrients before leaf shed to reduce the risk of frost damage and
478 the assimilation of carbon (Estiarte & Peñuelas, 2015). The response of leaf senescence to an
479 increase in temperature in autumn influences this trade-off. The absence of delays over time in
480 the onset of leaf coloration and in the onset of decrease in maximum canopy photosynthetic
481 capacity in response to climate warming, as observed in our study, may limit the detrimental
482 effects of frost in autumn (Liu *et al.*, 2018) and may also pose limited impacts on the start of the
483 remobilization and resorption of nutrients (Estiarte & Peñuelas, 2015). The stronger positive
484 correlation between the advanced stage of leaf coloration and the T_{\min} for an optimized period
485 preceding that stage (Fig. 4 and Fig. S13), implies that climatic warming may help to extend the
486 period from the onset to the end of leaf coloration in extensive areas across the middle and high
487 northern latitudes (Fig. 6); this in turn may increase the efficiency of nitrogen resorption
488 (Rennenberg *et al.*, 2010) and increase the vegetation greenness in this period, which will
489 modify on the surface energy balance through biophysical processes (Shen *et al.*, 2015). The
490 extended period of leaf coloration may also prolong the plant transpiration time and increase soil
491 water consumption. The impact of autumn warming on net ecosystem productivity is dual,
492 increasing both respiratory flux to the atmosphere (Piao *et al.*, 2008) and forest gross primary
493 photosynthesis (Keenan *et al.*, 2014). The relatively static onset date of leaf coloration and its
494 weak response to temperature would preclude the vegetation from fully using the potential
495 increase in CO₂ assimilation in early autumn induced by warming (Stinziano & Way, 2017).
496 Combined with a delay in the end of the season and a respiration increase due to warming, this
497 suggests that additional warming will probably not result in a continuous increase in autumn
498 CO₂ assimilation.



499

500 **Fig. 6** Difference in temperature sensitivity between the end and onset of leaf coloration (D_{LCE}
 501 and D_{LCO}) over the period 2000–2018. The temperature sensitivity of D_{LCO} is defined as the
 502 coefficient for pre- D_{LCO} mean daily minimum temperature (T_{min}) in a linear regression in which
 503 D_{LCO} is set as the dependent variable and pre- D_{LCO} T_{min} and pre- D_{LCO} total precipitation are
 504 independent variables. The temperature sensitivity of D_{LCE} is calculated in a similar way. D_{LCO}
 505 and D_{LCE} are determined as the dates when NDVI decreases by 10% and 50%, respectively, of
 506 its annual amplitude, based on a generalized sigmoid function fitted from the annual NDVI
 507 profile. The bar chart in the bottom-left corner shows the percentage of area for each interval of
 508 the temperature sensitivity indicated by the color scale at the bottom. Positive values (green)
 509 indicate that D_{LCE} is more sensitive to temperature than D_{LCO} , whereas negative values (pink)
 510 indicate that D_{LCO} is more sensitive to temperature than D_{LCE} .

511 4.4 | Concluding remarks

512 In summary, satellite NDVI time series and ground-based phenological observations
 513 indicated no significant delay in the start of autumnal leaf coloration for most areas covered by
 514 natural vegetation over middle and high northern latitudes. Neither pre- D_{LCO} temperature nor
 515 pre- D_{LCO} precipitation significantly affected the interannual variations of the start of leaf
 516 coloration in most areas, indicating that the start of leaf senescence is triggered by photoperiod.
 517 Interestingly, there was a weaker positive correlation between the start of autumnal leaf

518 coloration and pre- D_{LCO} T_{min} for vegetation in regions with longer daylength, indicating strong
519 photoperiodic control of the start of leaf senescence. For vegetation with a given daylength at
520 D_{LCO} longer than 13.5 h, the positive correlation between D_{LCO} and pre- D_{LCO} T_{min} was slightly
521 stronger in colder areas, suggesting that there is strong selection pressure in harsher temperature
522 environments on the timing of leaf coloration onset and that autumn warming could have a
523 stronger delaying effect on leaf coloration onset in colder areas than in warmer areas. This study
524 suggests that autumnal warming will not change the start date of leaf senescence, but it might
525 slow the rate of senescence. A slower senescence speed possibly could extend the period of
526 senescence and provide more time to reallocate nutrients and prepare for overwintering. Such
527 changes could substantially affect carbon and nutrient cycles. Our study provides a foundation
528 for understanding the complex relationships among nutrient cycling, vegetation growth, energy
529 exchange, and climate change in autumn in temperate and boreal regions dominated by winter
530 deciduous vegetation.

531 **Data Availability**

532 The data supporting the findings of this study are available through the links given in the paper.

533 **References**

- 534 Bauerle, W.L., Oren, R., Way, D.A., Qian, S.S., Stoy, P.C., Thornton, P.E., Bowden, J.D., Hoffman, F.M. &
535 Reynolds, R.F. (2012) Photoperiodic regulation of the seasonal pattern of photosynthetic capacity
536 and the implications for carbon cycling. *Proceedings of the National Academy of Sciences*, **109**,
537 8612-7.
- 538 Beck, P.S.A., Atzberger, C., Høgda, K.A., Johansen, B. & Skidmore, A.K. (2006) Improved monitoring of
539 vegetation dynamics at very high latitudes: A new method using MODIS NDVI. *Remote Sensing*
540 *of Environment*, **100**, 321-334.
- 541 Berman, E.E., Graves, T.A., Mickle, N.L., Merkle, J.A., Johnston, A.N. & Chong, G.W. (2020) Comparative
542 Quality and Trend of Remotely Sensed Phenology and Productivity Metrics across the Western
543 United States. *Remote Sensing*, **12**
- 544 Borthwick, H.A. & Hendricks, S.B. (1960) Photoperiodism in Plants. *Science*, **132**, 1223-1228.
- 545 Cao, R., Chen, Y., Shen, M., Chen, J., Zhou, J., Wang, C. & Yang, W. (2018) A simple method to improve
546 the quality of NDVI time-series data by integrating spatiotemporal information with the
547 Savitzky-Golay filter. *Remote Sensing of Environment*, **217**, 244-257.
- 548 Chen, J., Rao, Y., Shen, M., Wang, C., Zhou, Y., Ma, L., Tang, Y. & Yang, X. (2016) A simple method for
549 detecting phenological change from time series of vegetation index. *IEEE Transactions on*
550 *Geoscience and Remote Sensing*, **54**, 3436-3449.
- 551 China Meteorological Administration (1993) *Observation criterion of agricultural meteorology*. China
552 Meteorological Press, Beijing (in Chinese).

- 553 Delpierre, N., Dufrêne, E., Soudani, K., Ulrich, E., Cecchini, S., Boé, J. & François, C. (2009) Modelling
554 interannual and spatial variability of leaf senescence for three deciduous tree species in France.
555 *Agricultural and Forest Meteorology*, **149**, 938-948.
- 556 Elmore, A.J., Guinn, S.M., Minsley, B.J. & Richardson, A.D. (2012) Landscape controls on the timing of
557 spring, autumn, and growing season length in mid-Atlantic forests. *Global Change Biology*, **18**,
558 656-674.
- 559 Estiarte, M. & Peñuelas, J. (2015) Alteration of the phenology of leaf senescence and fall in winter
560 deciduous species by climate change: effects on nutrient proficiency. *Global Change Biology*, **21**,
561 1005-1017.
- 562 Estrella, N. & Menzel, A. (2006) Responses of leaf colouring in four deciduous tree species to climate and
563 weather in Germany. *Climate Research*, **32**, 253-267.
- 564 Ford, K.R., Harrington, C.A. & Clair, J.B.S. (2017) Photoperiod cues and patterns of genetic variation limit
565 phenological responses to climate change in warm parts of species' range: Modeling
566 diameter-growth cessation in coast Douglas-fir. *Global Change Biology*, **23**, 3348-3362.
- 567 Fracheboud, Y., Luquez, V., Björkén, L., Sjödin, A., Tuominen, H. & Jansson, S. (2009) The control of
568 autumn senescence in European aspen. *Plant Physiology*, **149**, 1982-1991.
- 569 Friedl, M. & Sulla-Menasse, D. (2015) MCD12C1 MODIS/Terra+Aqua Land Cover Type Yearly L3 Global
570 0.05Deg CMG V006 In: *NASA EOSDIS Land Processes DAAC*.
571 <http://doi.org/10.5067/MODIS/MCD12C1.006>
- 572 Fu, Y.H., Piao, S., Delpierre, N., Hao, F., Hänninen, H., Liu, Y., Sun, W., Janssens, I.A. & Campioli, M.
573 (2018) Larger temperature response of autumn leaf senescence than spring leaf-out phenology.
574 *Global Change Biology*, **24**, 2159-2168.
- 575 Fu, Y.H., Zhao, H., Piao, S., Peaucelle, M., Peng, S., Zhou, G., Ciais, P., Huang, M., Menzel, A., Penuelas,
576 J., Song, Y., Vitasse, Y., Zeng, Z. & Janssens, I.A. (2015) Declining global warming effects on the
577 phenology of spring leaf unfolding. *Nature*, **526**, 104-107.
- 578 Fu, Y.S.H., Campioli, M., Vitasse, Y., De Boeck, H.J., Van den Berge, J., AbdElgawad, H., Asard, H., Piao,
579 S., Deckmyn, G. & Janssens, I.A. (2014) Variation in leaf flushing date influences autumnal
580 senescence and next year's flushing date in two temperate tree species. *Proceedings of the*
581 *National Academy of Sciences*, **111**, 7355-7360.
- 582 Gan, S.S. & Amasino, R.M. (1997) Making sense of senescence - Molecular genetic regulation and
583 manipulation of leaf senescence. *Plant Physiology*, **113**, 313-319.
- 584 Ganguly, S., Friedl, M.A., Tan, B., Zhang, X. & Verma, M. (2010) Land surface phenology from MODIS:
585 Characterization of the Collection 5 global land cover dynamics product. *Remote Sensing of*
586 *Environment*, **114**, 1805-1816.
- 587 Garonna, I., De Jong, R., De Wit, A.J.W., Múcher, C.A., Schmid, B. & Schaepman, M.E. (2014) Strong
588 contribution of autumn phenology to changes in satellite-derived growing season length estimates
589 across Europe (1982-2011). *Global Change Biology*, **20**, 3457-3470.
- 590 Ge, Q.S., Wang, H.J., Rutishauser, T. & Dai, J.H. (2015) Phenological response to climate change in
591 China: a meta-analysis. *Global Change Biology*, **21**, 265-274.
- 592 Gill, A.L., Gallinat, A.S., Sanders-DeMott, R., Rigden, A.J., Short Gianotti, D.J., Mantooth, J.A. & Templer,
593 P.H. (2015) Changes in autumn senescence in northern hemisphere deciduous trees: a
594 meta-analysis of autumn phenology studies. *Annals of Botany*, **116**, 875-888.
- 595 Gu, L., Post, W.M., Baldocchi, D.D., Black, T.A., Suyker, A.E., Verma, S.B., Vesala, T. & Wofsy, S.C. (2009)
596 Characterizing the seasonal dynamics of plant community photosynthesis across a range of
597 vegetation types. *Phenology of Ecosystem Processes* (ed. by A. Noormets), pp. 35-58. Springer,

598 New York, NY.

599 Hamner, K.C. (1940) Interrelation of light and darkness in photoperiod. *Botanical Gazette*, **101**, 658-687.

600 Harris, I., Jones, P.D., Osborn, T.J. & Lister, D.H. (2014) Updated high-resolution grids of monthly climatic
601 observations – the CRU TS3.10 Dataset. *International Journal of Climatology*, **34**, 623-642.

602 Howe, G.T., Hackett, W.P., Furnier, G.R. & Klevorn, R.E. (1995) Photoperiodic responses of a northern
603 and southern ecotype of black cottonwood. *Physiologia Plantarum*, **93**, 695-708.

604 Jeganathan, C., Dash, J. & Atkinson, P.M. (2014) Remotely sensed trends in the phenology of northern
605 high latitude terrestrial vegetation, controlling for land cover change and vegetation type. *Remote
606 Sensing of Environment*, **143**, 154-170.

607 Jeong, S.J., Ho, C.H., Gim, H.J. & Brown, M.E. (2011) Phenology shifts at start vs. end of growing season
608 in temperate vegetation over the Northern Hemisphere for the period 1982–2008. *Global Change
609 Biology*, **17**, 2385-2399.

610 Keenan, T.F. & Richardson, A.D. (2015) The timing of autumn senescence is affected by the timing of
611 spring phenology: implications for predictive models. *Global Change Biology*, **21**, 2634-2641.

612 Keenan, T.F., Gray, J., Friedl, M.A., Toomey, M., Bohrer, G., Hollinger, D.Y., Munger, J.W., O'Keefe, J.,
613 Schmid, H.P., Wing, I.S., Yang, B. & Richardson, A.D. (2014) Net carbon uptake has increased
614 through warming-induced changes in temperate forest phenology. *Nature Climate Change*, **4**,
615 598-604.

616 Keskitalo, J., Bergquist, G., Gardeström, P. & Jansson, S. (2005) A cellular timetable of autumn
617 senescence. *Plant Physiol*, **139**, 1635-1648.

618 Klosterman, S. & Richardson, A.D. (2017) Observing Spring and Fall Phenology in a Deciduous Forest
619 with Aerial Drone Imagery. *Sensors (Basel)*, **17**

620 Klosterman, S.T., Hufkens, K., Gray, J.M., Melaas, E., Sonnentag, O., Lavine, I., Mitchell, L., Norman, R.,
621 Friedl, M.A. & Richardson, A.D. (2014) Evaluating remote sensing of deciduous forest phenology
622 at multiple spatial scales using PhenoCam imagery. *Biogeosciences*, **11**, 4305-4320.

623 Körner, C. (2007) Significance of temperature in plant life. *Plant Growth and Climate Change* (ed. by J.I.L.
624 Morison and M.D. Morecroft), pp. 48-69.

625 Körner, C. & Basler, D. (2010) Response-warming, photoperiods, and tree phenology. *Science*, **329**,
626 278-278.

627 Körner, C. & Hiltbrunner, E. (2018) The 90 ways to describe plant temperature. *Perspectives in Plant
628 Ecology, Evolution and Systematics*, **30**, 16-21.

629 Leblans, N.I.W., Sigurdsson, B.D., Vicca, S., Fu, Y.S., Penuelas, J. & Janssens, I.A. (2017) Phenological
630 responses of Icelandic subarctic grasslands to short-term and long-term natural soil warming.
631 *Global Change Biology*, **23**, 4932-4945.

632 Lim, P.O., Kim, H.J. & Nam, H.G. (2007) Leaf Senescence. *Annual Review of Plant Biology*, **58**, 115-136.

633 Liu, Q., Fu, Y.H., Zhu, Z., Liu, Y., Liu, Z., Huang, M., Janssens, I.A. & Piao, S. (2016) Delayed autumn
634 phenology in the Northern Hemisphere is related to change in both climate and spring phenology.
635 *Global Change Biology*, **22**, 3702-3711.

636 Liu, Q., Piao, S., Janssens, I.A., Fu, Y., Peng, S., Lian, X., Ciais, P., Myneni, R.B., Penuelas, J. & Wang, T.
637 (2018) Extension of the growing season increases vegetation exposure to frost. *Nature
638 Communications*, **9**, 426.

639 Lukasová, V., Bucha, T., Škvareninová, J. & Škvarenina, J. (2019) Validation and Application of European
640 Beech Phenological Metrics Derived from MODIS Data along an Altitudinal Gradient. *Forests*, **10**,
641 60.

642 Mariën, B., Balzarolo, M., Dox, I., Leys, S., Lorène, M.J., Geron, C., Portillo-Estrada, M., AbdElgawad, H.,

643 Asard, H., Campioli, M., Mariën, B., Balzarolo, M., Dox, I., Leys, S., Lorène, M.J., Geron, C., Portillo -
644 Estrada, M., AbdElgawad, H., Asard, H. & Campioli, M. (2019) Detecting the onset of autumn leaf
645 senescence in deciduous forest trees of the temperate zone. *New Phytologist*, **224**, 166-176.
646 Melaas, E.K., Friedl, M.A. & Zhu, Z. (2013) Detecting interannual variation in deciduous broadleaf forest
647 phenology using Landsat TM/ETM+ data. *Remote Sensing of Environment*, **132**, 176-185.
648 Menzel, A., Yuan, Y., Matiu, M., Sparks, T., Scheifinger, H., Gehrig, R. & Estrella, N. (2020) Climate
649 change fingerprints in recent European plant phenology. *Global Change Biology*, **26**, 2599-2612.
650 Myneni, R.B., Keeling, C.D., Tucker, C.J., Asrar, G. & Nemani, R.R. (1997) Increased plant growth in the
651 northern high latitudes from 1981 to 1991. *Nature*, **386**, 698-702.
652 Nagai, S., Nasahara, K.N., Muraoka, H., Akiyama, T. & Tsuchida, S. (2010) Field experiments to test the
653 use of the normalized-difference vegetation index for phenology detection. *Agricultural and Forest
654 Meteorology*, **150**, 152-160.
655 Nezval, O., Krejza, J., Světlík, J., Šigut, L. & Horáček, P. (2020) Comparison of traditional ground-based
656 observations and digital remote sensing of phenological transitions in a floodplain forest.
657 *Agricultural and Forest Meteorology*, **291**
658 Pastorello, G.Z., Papale, D., Chu, H., Trotta, C., Agarwal, D.A., Canfora, E., Baldocchi, D.D. & Torn, M.S.
659 (2017) A new data set to keep a sharper eye on land-air exchanges. In: *Eos*
660 Paus, E., Nilsen, J. & Junttila, O. (1986) Bud dormancy and vegetative growth in *Salix-Polaris* as affected
661 by temperature and photoperiod. *Polar Biology*, **6**, 91-95.
662 Peñuelas, J., Rutishauser, T. & Filella, I. (2009) Phenology Feedbacks on Climate Change. *Science*, **324**,
663 887-888.
664 Piao, S., Liu, Q., Chen, A., Janssens, I.A., Fu, Y., Dai, J., Liu, L., Lian, X., Shen, M. & Zhu, X. (2019) Plant
665 phenology and global climate change: Current progresses and challenges. *Global Change
666 Biology*, **25**, 1922-1940.
667 Piao, S., Ciais, P., Friedlingstein, P., Peylin, P., Reichstein, M., Luysaert, S., Margolis, H., Fang, J., Barr,
668 A., Chen, A., Grelle, A., Hollinger, D.Y., Laurila, T., Lindroth, A., Richardson, A.D. & Vesala, T.
669 (2008) Net carbon dioxide losses of northern ecosystems in response to autumn warming. *Nature*,
670 **451**, 49-52.
671 Ren, J., Campbell, J. & Shao, Y. (2017) Estimation of SOS and EOS for Midwestern US Corn and
672 Soybean Crops. *Remote Sensing*, **9**
673 Rennenberg, H., Wildhagen, H. & Ehltng, B. (2010) Nitrogen nutrition of poplar trees. *Plant Biology*, **12**,
674 275-291.
675 Richardson, A.D., Hufkens, K., Milliman, T. & Froking, S. (2018) Intercomparison of phenological
676 transition dates derived from the PhenoCam Dataset V1.0 and MODIS satellite remote sensing.
677 *Scientific Reports*, **8**
678 Richardson, A.D., Keenan, T.F., Migliavacca, M., Ryu, Y., Sonnentag, O. & Toomey, M. (2013) Climate
679 change, phenology, and phenological control of vegetation feedbacks to the climate system.
680 *Agricultural and Forest Meteorology*, **169**, 156-173.
681 Sen, P.K. (1968) Estimates of the Regression Coefficient Based on Kendall's Tau. *Journal of the American
682 Statistical Association*, **63**, 1379-1389.
683 Seyednasrollah, B., Young, A.M., Hufkens, K., Milliman, T., Friedl, M.A., Froking, S. & Richardson, A.D.
684 (2019a) Tracking vegetation phenology across diverse biomes using Version 2.0 of the
685 PhenoCam Dataset. *Sci Data*, **6**, 222.
686 Seyednasrollah, B., Young, A.M., Hufkens, K., Milliman, T., Friedl, M.A., Froking, S., Richardson, A.D.,
687 Abraha, M., Allen, D.W., Apple, M., Arain, M.A., Baker, J., Baker, J.M., Baldocchi, D., Bernacchi,

688 C.J., Bhattacharjee, J., Blanken, P., Bosch, D.D., Boughton, R., Boughton, E.H., Brown, R.F.,
689 Browning, D.M., Brunsell, N., Burns, S.P., Cavagna, M., Chu, H., Clark, P.E., Conrad, B.J.,
690 Cremonese, E., Debinski, D., Desai, A.R., Diaz-Delgado, R., Duchesne, L., Dunn, A.L.,
691 Eissenstat, D.M., El-Madany, T., Ellum, D.S.S., Ernest, S.M., Esposito, A., Fenstermaker, L.,
692 Flanagan, L.B., Forsythe, B., Gallagher, J., Gianelle, D., Griffis, T., Groffman, P., Gu, L., Guillemot,
693 J., Halpin, M., Hanson, P.J., Hemming, D., Hove, A.A., Humphreys, E.R., Jaimes-Hernandez, A.,
694 Jaradat, A.A., Johnson, J., Keel, E., Kelly, V.R., Kirchner, J.W., Kirchner, P.B., Knapp, M.,
695 Krassovski, M., Langvall, O., Lanthier, G., Maire, G.I., Magliulo, E., Martin, T.A., McNeil, B., Meyer,
696 G.A., Migliavacca, M., Mohanty, B.P., Moore, C.E., Mudd, R., Munger, J.W., Murrell, Z.E., Nestic,
697 Z., Neufeld, H.S., O'Halloran, T.L., Oechel, W., Oishi, A.C., Oswald, W.W., Perkins, T.D., Reba,
698 M.L., Rundquist, B., Runkle, B.R., Russell, E.S., Sadler, E.J., Saha, A., Saliendra, N.Z.,
699 Schmalbeck, L., Schwartz, M.D., Scott, R.L., Smith, E.M., Sonnentag, O., Stoy, P., Strachan, S.,
700 Suvocarev, K., Thom, J.E., Thomas, R.Q., Van den berg, A.K., Vargas, R., Verfaillie, J., Vogel,
701 C.S., Walker, J.J., Webb, N., Wetzell, P., Weyers, S., Whipple, A.V., Whitham, T.G., Wohlfahrt, G.,
702 Wood, J.D., Wolf, S., Yang, J., Yang, X., Yenni, G., Zhang, Y., Zhang, Q. & Zona, D. (2019b)
703 PhenoCam Dataset v2.0: Vegetation Phenology from Digital Camera Imagery, 2000-2018. In.
704 ORNL Distributed Active Archive Center

705 Shen, M., Tang, Y., Desai, A.R., Gough, C. & Chen, J. (2014) Can EVI-derived land-surface phenology be
706 used as a surrogate for phenology of canopy photosynthesis? *International Journal of Remote*
707 *Sensing*, **35**, 1162-1174.

708 Shen, M.G., Piao, S.L., Jeong, S.J., Zhou, L.M., Zeng, Z.Z., Ciais, P., Chen, D.L., Huang, M.T., Jin, C.S.,
709 Li, L.Z.X., Li, Y., Myneni, R.B., Yang, K., Zhang, G.X., Zhang, Y.J. & Yao, T.D. (2015) Evaporative
710 cooling over the Tibetan Plateau induced by vegetation growth. *Proceedings of the National*
711 *Academy of Sciences*, **112**, 9299-9304.

712 Soudani, K., Delpierre, N., Berveiller, D., Hmimina, G., Pontailier, J.-Y., Seureau, L., Vincent, G. & Dufrêne,
713 É. (2020) A survey of proximal methods for monitoring leaf phenology in
714 temperate deciduous forests. *Biogeosciences Discuss. [preprint]*,
715 <https://doi.org/10.5194/bg-2020-389>, in review,

716 Soudani, K., Hmimina, G., Delpierre, N., Pontailier, J.Y., Aubinet, M., Bonal, D., Caquet, B., de Grandcourt,
717 A., Burban, B., Flechard, C., Guyon, D., Granier, A., Gross, P., Heinesh, B., Longdoz, B., Loustau,
718 D., Moureaux, C., Ourcival, J.M., Rambal, S., Saint André, L. & Dufrêne, E. (2012) Ground-based
719 Network of NDVI measurements for tracking temporal dynamics of canopy structure and
720 vegetation phenology in different biomes. *Remote Sensing of Environment*, **123**, 234-245.

721 Stinziano, J.R. & Way, D.A. (2017) Autumn photosynthetic decline and growth cessation in seedlings of
722 white spruce are decoupled under warming and photoperiod manipulations. *Plant Cell and*
723 *Environment*, **40**, 1296-1316.

724 Tang, J., Körner, C., Muraoka, H., Piao, S., Shen, M., Thackeray, S.J. & Yang, X. (2016) Emerging
725 opportunities and challenges in phenology: a review. *Ecosphere*, **7**, e01436.

726 Theil, H. (1992) A rank-invariant method of linear and polynomial regression analysis. *Henri Theil's*
727 *Contributions to Economics and Econometrics: Econometric Theory and Methodology* (ed. by B.
728 Raj and J. Koerts), pp. 345-381. Springer Netherlands, Dordrecht.

729 Thomas, H. & Stoddart, J.L. (1980) Leaf Senescence. *Annual Review of Plant Physiology and Plant*
730 *Molecular Biology*, **31**, 83-111.

731 Vermote, E.F. (2015) MOD09CMG MODIS/Terra Surface Reflectance Daily L3 Global 0.05Deg CMG
732 V006. In: *NASA EOSDIS Land Processes DAAC*

733 Viovy, N. (2018) CRUNCEP Version 7 - Atmospheric Forcing Data for the Community Land Model. In:
734 *Research Data Archive at the National Center for Atmospheric Research, Computational and*
735 *Information Systems Laboratory*, Boulder CO.

736 Wang, C. & Zhu, K. (2019) Misestimation of growing season length due to inaccurate construction of
737 satellite vegetation index time series. *IEEE Geoscience and Remote Sensing Letters*, **16**,
738 1185-1189.

739 White, M.A., Thornton, P.E. & Running, S.W. (1997) A continental phenology model for monitoring
740 vegetation responses to interannual climatic variability. *Global Biogeochemical Cycles*, **11**,
741 217-234.

742 Wingate, L., Ogée, J., Cremonese, E., Filippa, G., Mizunuma, T., Migliavacca, M., Moisy, C., Wilkinson, M.,
743 Moureaux, C., Wohlfahrt, G., Hammerle, A., Hörtnagl, L., Gimeno, C., Porcar-Castell, A.,
744 Galvagno, M., Nakaji, T., Morison, J., Kolle, O., Knohl, A., Kutsch, W., Kolari, P., Nikinmaa, E.,
745 Ibrom, A., Gielen, B., Eugster, W., Balzarolo, M., Papale, D., Klumpp, K., Köstner, B., Grünwald,
746 T., Joffre, R., Ourcival, J.M., Hellstrom, M., Lindroth, A., George, C., Longdoz, B., Genty, B.,
747 Levula, J., Heinesch, B., Sprintsin, M., Yakir, D., Manise, T., Guyon, D., Ahrends, H.,
748 Plaza-Aguilar, A., Guan, J.H. & Grace, J. (2015) Interpreting canopy development and physiology
749 using a European phenology camera network at flux sites. *Biogeosciences*, **12**, 5995-6015.

750 Xu, C., Liu, H., Williams, A.P., Yin, Y. & Wu, X. (2016) Trends toward an earlier peak of the growing
751 season in Northern Hemisphere mid-latitudes. *Global Change Biology*, **22**, 2852-2860.

752 Yang, X., Tang, J. & Mustard, J.F. (2014) Beyond leaf color: Comparing camera-based phenological
753 metrics with leaf biochemical, biophysical, and spectral properties throughout the growing season
754 of a temperate deciduous forest. *Journal of Geophysical Research: Biogeosciences*, **119**,
755 181-191.

756 Yu, H., Luedeling, E. & Xu, J. (2010) Winter and spring warming result in delayed spring phenology on the
757 Tibetan Plateau. *Proceedings of the National Academy of Sciences*, **107**, 22151-22156.

758 Zhang, X. (2015) Reconstruction of a complete global time series of daily vegetation index trajectory from
759 long-term AVHRR data. *Remote Sensing of Environment*, **156**, 457-472.

760 Zhang, X., Tarpley, D. & Sullivan, J.T. (2007) Diverse responses of vegetation phenology to a warming
761 climate. *Geophysical Research Letters*, **34**

762 Zhang, X., Friedl, M.A., Schaaf, C.B., Strahler, A.H., Hodges, J.C., Gao, F., Reed, B.C. & Huete, A. (2003)
763 Monitoring vegetation phenology using MODIS. *Remote Sensing of Environment*, **84**, 471-475.

764 Zhang, X., Jayavelu, S., Liu, L., Friedl, M.A., Henebry, G.M., Liu, Y., Schaaf, C.B., Richardson, A.D. &
765 Gray, J. (2018) Evaluation of land surface phenology from VIIRS data using time series of
766 PhenoCam imagery. *Agricultural and Forest Meteorology*, **256-257**, 137-149.

767 Zhao, B., Donnelly, A. & Schwartz, M.D. (2020) Evaluating autumn phenology derived from field
768 observations, satellite data, and carbon flux measurements in a northern mixed forest, USA.
769 *International Journal of Biometeorology*, **64**, 713-727.

770 Zohner, C.M., Benito, B.M., Svenning, J.-C. & Renner, S.S. (2016) Day length unlikely to constrain
771 climate-driven shifts in leaf-out times of northern woody plants. *Nature Climate Change*, **6**,
772 1120-1123.

773

1
2
3
4
5
6
7
8
9
10
11
12

Supplementary Information for

Warming does not delay the start of autumnal leaf coloration but slows its progress rate

This PDF file includes:

Figures S1 to S25

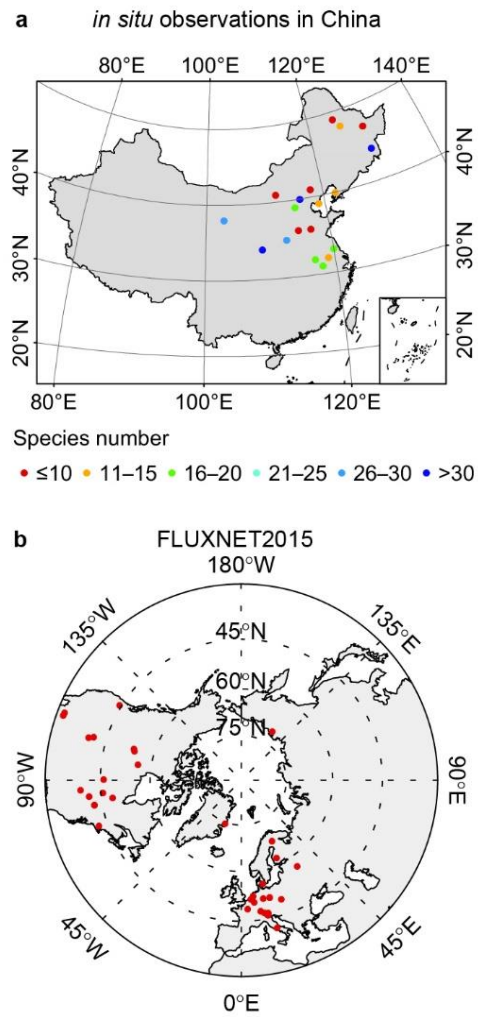
Tables S1 to S8

Supplementary Methods

Supplementary References

13 **Supplementary Figures**

14
15

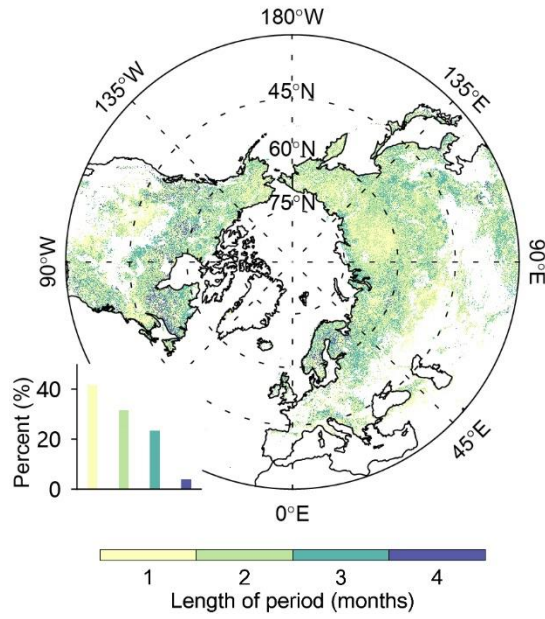


16

17 **Figure S1.** Locations of the sites of *in situ* observations used in this study. a, phenological observation

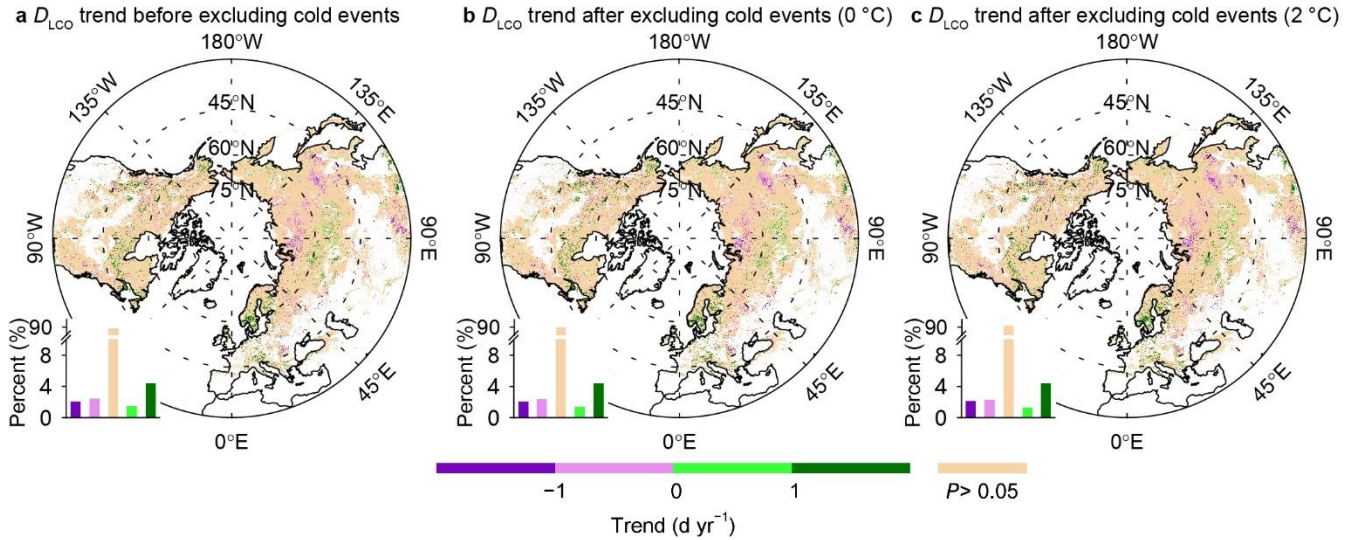
18 sites in China. b, FLUXNET2015 flux tower sites.

19



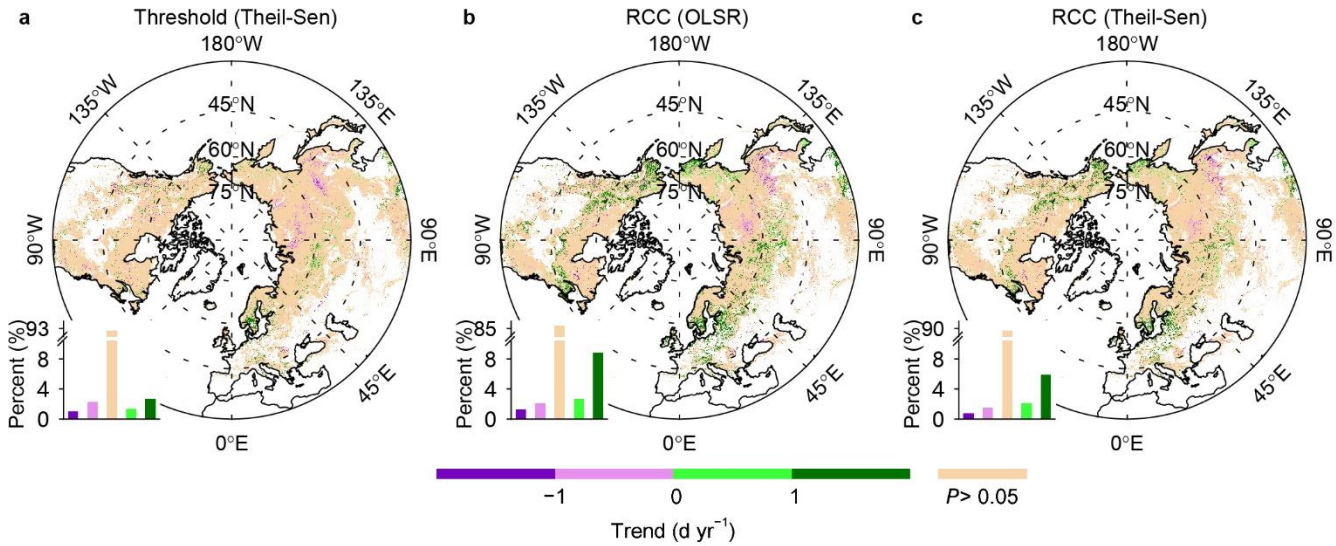
20
21
22
23
24

Figure S2. Spatial pattern of the length of the pre- D_{LCO} period for mean daily minimum temperature (T_{min}). The bar chart shows the percentage of area for each interval of the length of the pre- D_{LCO} period, with the length indicated by the color scale at the bottom.

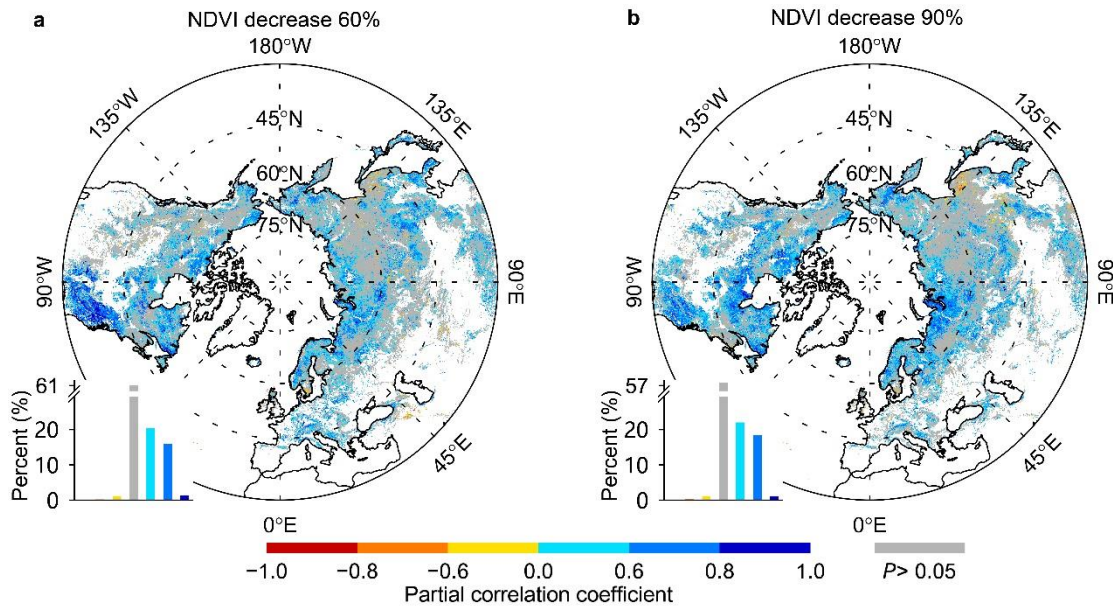


25
 26 **Figure S3.** Temporal trends in timing of the onset of leaf coloration (D_{LCO}), retrieved from satellite
 27 images over the period 2000–2016 before (a) and after (b and c) the exclusion of years with cold events
 28 before D_{LCO} . Cold events were determined mainly by using a threshold-based method with daily
 29 minimum temperatures of 0 °C (b) or 2 °C (c). The bar chart in each panel shows the percentage of area
 30 within each interval of the significant ($P < 0.05$) temporal trends and the percentage of area with
 31 nonsignificant trends, indicated by the color scale at the bottom. The percentage for each interval of the
 32 trend (positive and negative trend values refer to significantly delayed and advanced D_{LCO} , respectively)
 33 is provided in Table S5. D_{LCO} is defined as the date when NDVI decreases by 10% of its annual
 34 amplitude in autumn, on the basis of a generalized sigmoid function fitted from the annual NDVI profile.
 35 Significant temporal trends were determined by using t -tests at $P < 0.05$ and ordinary least squares
 36 regression between D_{LCO} and the respective years. Pixels dominated by croplands or with low vegetation
 37 coverage, weak seasonality, or peak NDVI in October–April were discarded.

38



39
 40 **Figure S4.** Temporal trends in timing of the onset of leaf coloration (D_{LCO}), retrieved from satellite
 41 images over the period 2000–2018. The bar chart in each panel shows the percentage of area within each
 42 interval of the significant ($P < 0.05$) temporal trends and the percentage of area with nonsignificant
 43 trends, indicated by the color scale at the bottom. Positive and negative trend values refer to significantly
 44 delayed and advanced D_{LCO} , respectively. D_{LCO} in (a) was defined as the date when NDVI decreased by
 45 10% of its annual amplitude in each autumn (threshold), on the basis of a generalized sigmoid function
 46 fitted from the annual NDVI profile. D_{LCO} in (b) and (c) was determined as the date when the rate of
 47 change of the curvature (RCC) of a double logistic-function-fitted NDVI curve reached its first local
 48 minimum value in the descending period. In (a) and (c), significant temporal trends were determined by
 49 using Mann-Kendall tests at $P < 0.05$ and a Theil-Sen estimator between D_{LCO} and the respective years;
 50 in (b), significant temporal trends were determined by using t -tests at $P < 0.05$ and ordinary least squares
 51 regression (OLSR) between D_{LCO} and respective years. Pixels dominated by croplands or with low
 52 vegetation coverage, weak seasonality, or peak NDVI in October–April were discarded.

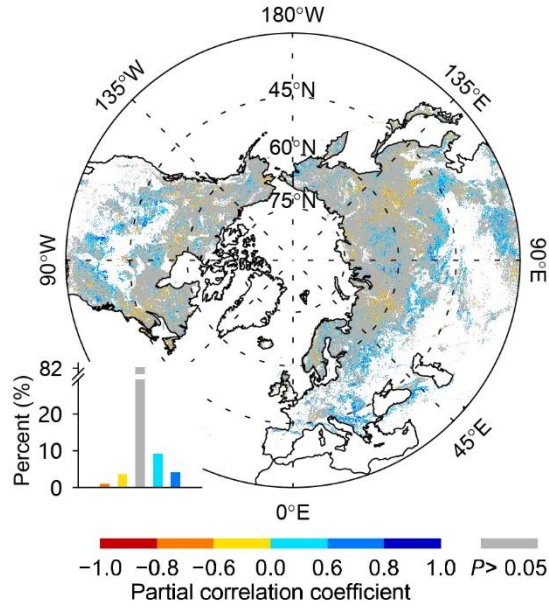


53

54 **Figure S5.** Spatial pattern of the partial correlation coefficient between the timing of the end of leaf
 55 coloration (D_{LCE}) and pre- D_{LCE} T_{min} over the period 2000–2018. D_{LCE} was determined as the date when
 56 NDVI drops by 60% (a) and 90% (b), respectively. The bar chart in the bottom-left corner shows the
 57 percentage of area for each interval of the partial correlation coefficient, with the coefficient values
 58 indicated by the color scale at the bottom. Non-significant correlations ($P > 0.05$) are in gray.

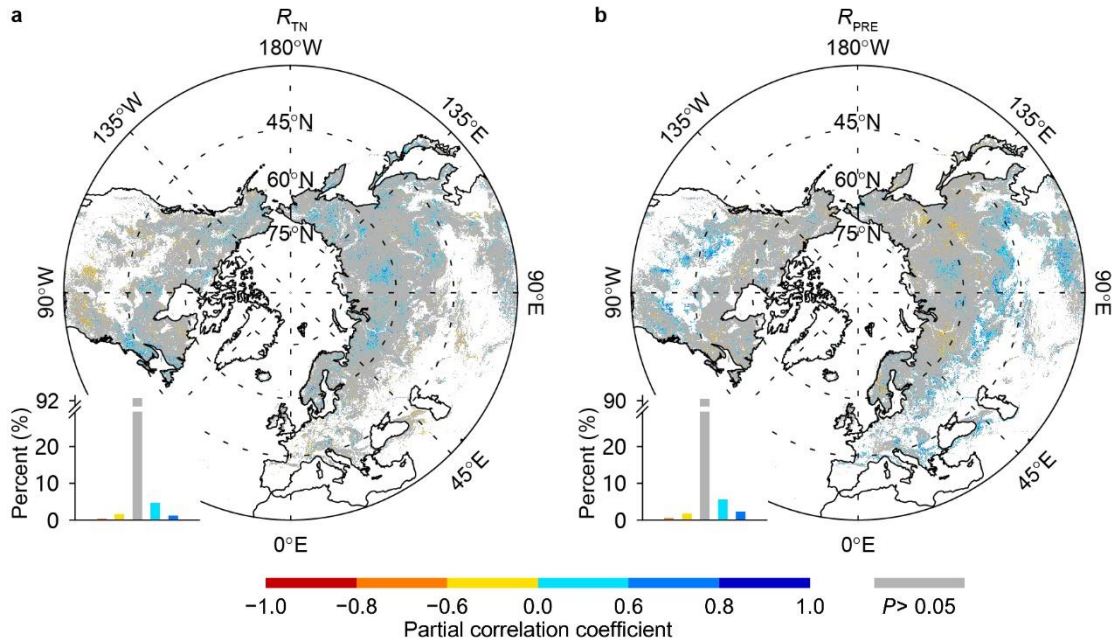
59

60

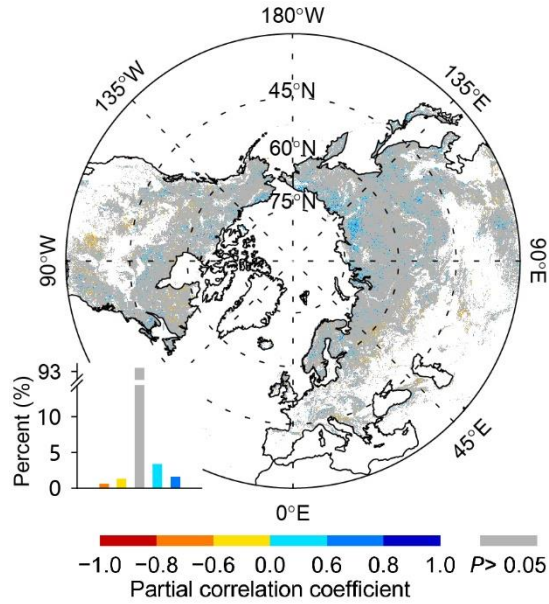


61
 62 **Figure S6.** Spatial pattern of the partial correlation coefficient between the timing of onset of leaf
 63 coloration (D_{LCO}) and pre- D_{LCO} total precipitation over the period 2000–2018. The bar chart in the
 64 bottom-left corner shows the percentage of area for each interval of the partial correlation coefficient,
 65 with the coefficient values indicated by the color scale at the bottom. Non-significant correlations ($P >$
 66 0.05) are in gray, and the percentage for each interval is provided in Table 1.

67



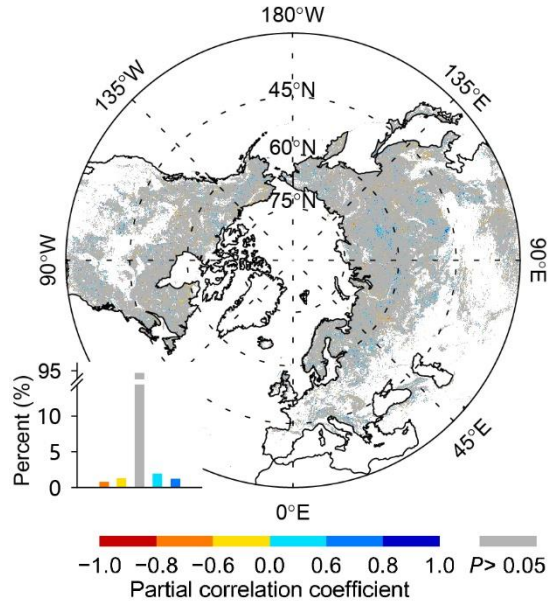
68
69 **Figure S7.** Spatial pattern of the partial correlation coefficient between the timing of onset of leaf
70 coloration (D_{LCO}) and pre- D_{LCO} (1 month preceding the multiyear mean D_{LCO}) climatic factors over the
71 period 2000–2018. a, Spatial pattern of the partial correlation coefficient (R_{TN}) between D_{LCO} and pre-
72 D_{LCO} mean daily minimum temperature (T_{min}) while controlling for the corresponding total precipitation.
73 b, Spatial pattern of the partial correlation coefficient (R_{PRE}) between D_{LCO} and pre- D_{LCO} total
74 precipitation while controlling for the corresponding T_{min} . The bar chart in each panel shows the
75 percentage of area for each interval of the partial correlation coefficient, with the coefficient value
76 indicated by the color scale at the bottom. Non-significant correlations ($P > 0.05$) are in gray.
77



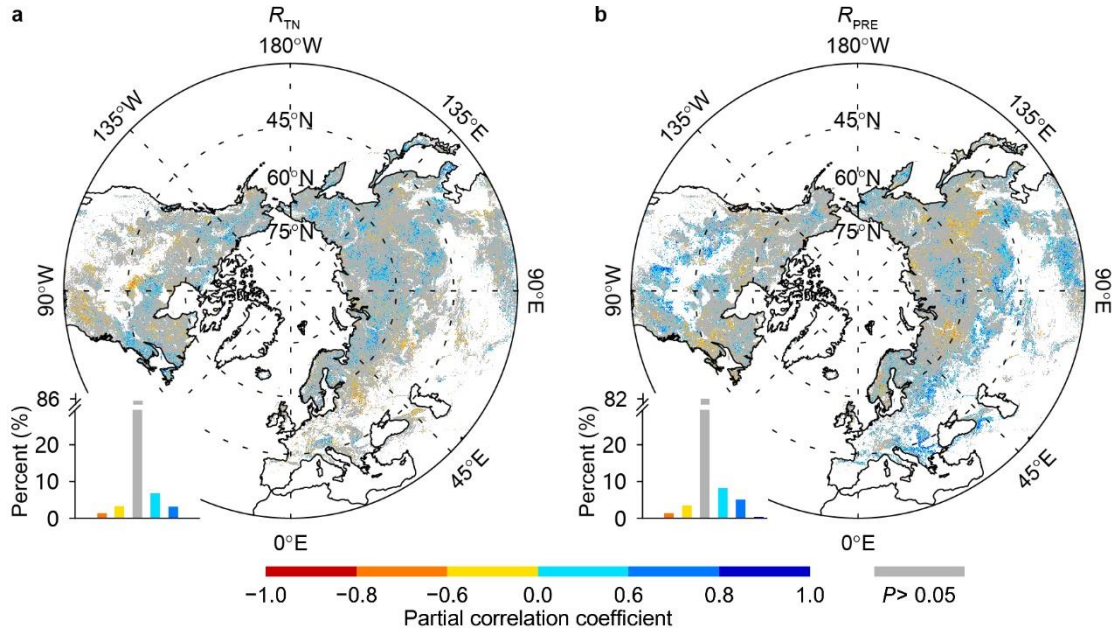
78

79 **Figure S8.** Spatial pattern of the partial correlation coefficient between the timing of onset of leaf
 80 coloration (D_{LCO}) and $pre-D_{LCO}$ (15 days preceding the multiyear mean D_{LCO}) mean daily minimum
 81 temperature while controlling for the corresponding total precipitation over the period 2000–2016. The
 82 bar chart shows the percentage of area for each interval of partial correlation coefficient, with the
 83 coefficient value indicated by the color scale at the bottom. Non-significant correlations ($P > 0.05$) are in
 84 gray. Daily minimum temperature was extracted from the CRU-NCEP 7.2 6-hourly dataset and
 85 determined as the minimum value of the four 6-hourly minimum temperature values for each day.

86



87
 88 **Figure S9.** Spatial pattern of the partial correlation coefficient between the timing of the onset of leaf
 89 coloration (D_{LCO}) and the lowest daily minimum temperature (T_{min}) during the 15 days before the
 90 multiyear mean D_{LCO} , with the concurrent mean T_{min} (mean of the remaining 14 T_{min} values after
 91 removal of the lowest T_{min} during the period) and total precipitation as control variables over the period
 92 2000–2016. The bar chart shows the percentage of area for each interval of the partial correlation
 93 coefficient ($P < 0.05$), with the coefficient indicated by the color scale at the bottom. Non-significant
 94 correlations ($P > 0.05$) are in gray. Daily minimum temperature was extracted from the CRUNCEP 7.2
 95 6-hourly dataset and determined as the minimum value of the four 6-hourly minimum temperature
 96 values for each day.
 97

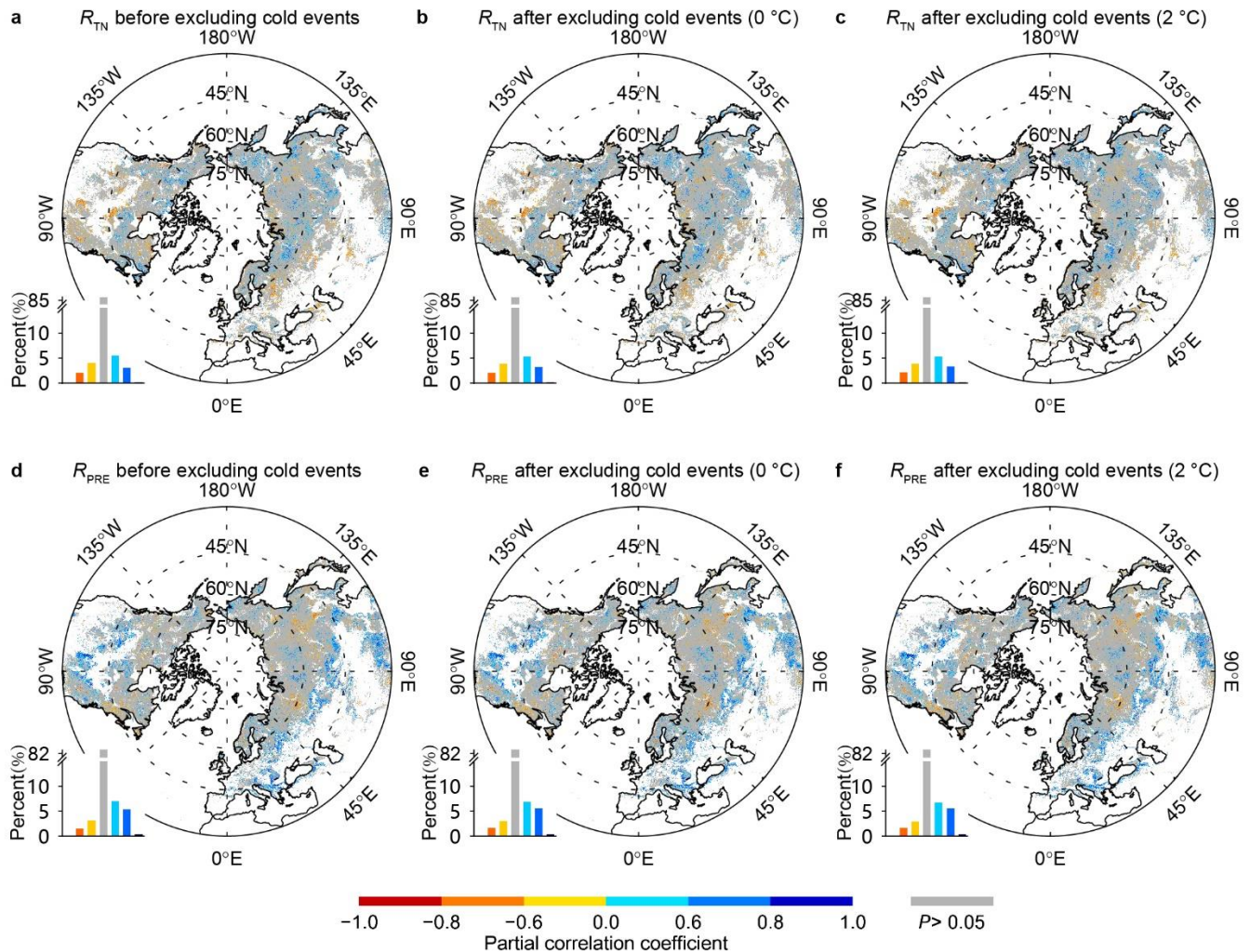


98

99

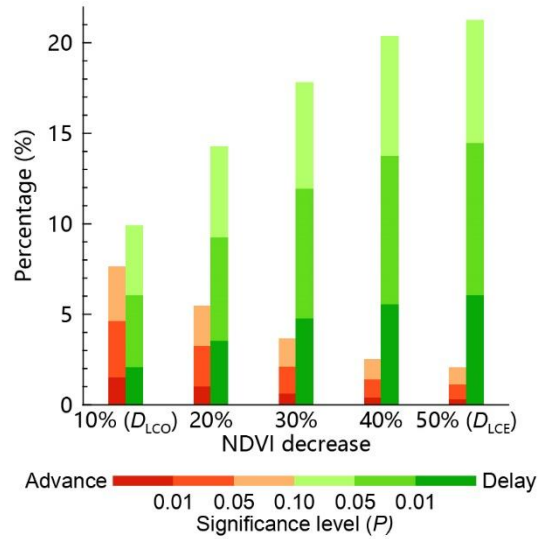
Figure S10. Spatial pattern of the partial correlation coefficient between the timing of onset of leaf coloration (D_{LCO}) and pre- D_{LCO} climatic factors, with green-up onset date as an extra control variable over the period 2000–2018. a, Spatial pattern of the partial correlation coefficient (R_{TN}) between D_{LCO} and pre- D_{LCO} mean daily minimum temperature (T_{min}) while controlling for the corresponding total precipitation and green-up onset date. b, Spatial pattern of the partial correlation coefficient (R_{PRE}) between D_{LCO} and pre- D_{LCO} total precipitation while controlling for the corresponding T_{min} and green-up onset date. The bar chart in each panel shows the percentage of area for each interval of the partial correlation coefficient, with the coefficient value indicated by the color scale at the bottom. Non-significant correlations ($P > 0.05$) are in gray.

108

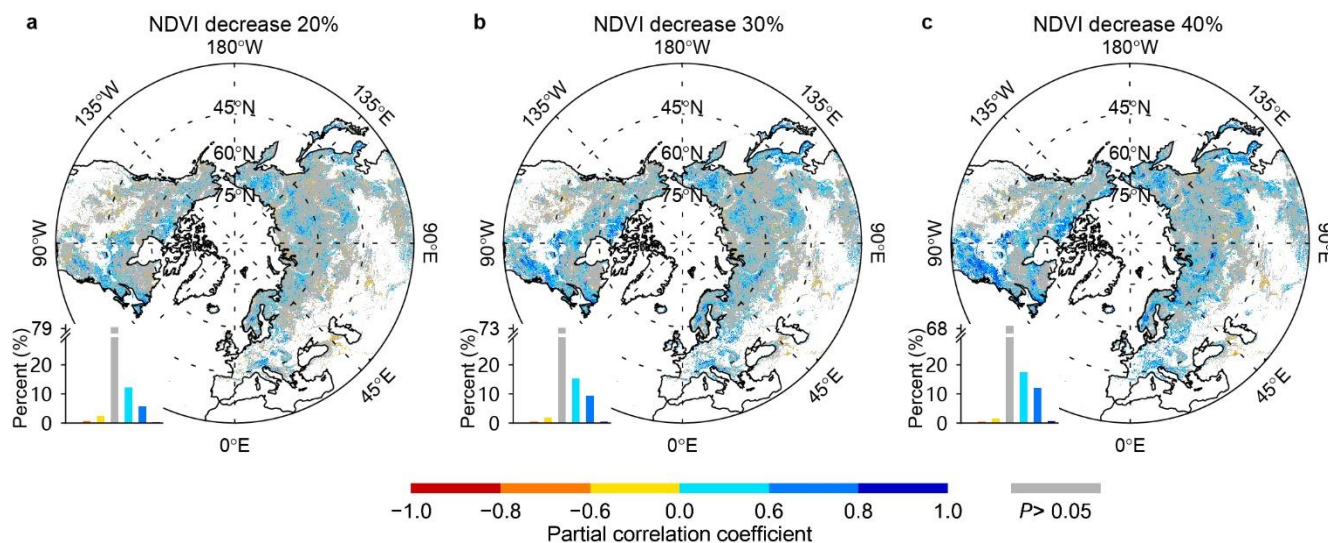


109
 110 **Figure S11.** Spatial pattern of the partial correlation coefficient between the timing of onset of leaf
 111 coloration (D_{LCO}) and pre- D_{LCO} climatic factors over the period 2000–2016 before and after the
 112 exclusion of years with cold events before D_{LCO} . a–c, Spatial pattern of the partial correlation coefficient
 113 (R_{TN}) between D_{LCO} and pre- D_{LCO} mean daily minimum temperature (T_{min}) before (a) and after (b and c)
 114 the exclusion of years with cold events. d–f, The same as (a–c), but for the partial correlation between
 115 D_{LCO} and pre- D_{LCO} total precipitation (R_{PRE}). The bar chart in each panel shows the percentage of area
 116 for each interval of the partial correlation coefficient, with the coefficient value indicated by the color
 117 scale at the bottom. Non-significant correlations ($P > 0.05$) are in gray, and the percentage for each
 118 interval is provided in Table S7. Cold events were determined mainly by using a threshold-based
 119 method with a daily minimum temperature of 0 °C (b and e) or 2 °C (c and f).

120



121
 122 **Figure S12.** Percentage of area with significant temporal trends in the timing of different stages of leaf
 123 coloration, as retrieved from satellite images. Significance levels of the temporal trends were determined
 124 by using *t*-tests for ordinary least squares regression over the period 2000–2018 at middle and high
 125 northern latitudes (30°N–75°N). The timings of the different stages of leaf coloration were defined as
 126 the dates when NDVI decreased by 10% (i.e., D_{LCO}), 20%, 30%, 40%, or 50% (i.e., D_{LCE}) of its annual
 127 amplitude in autumn, on the basis of a generalized sigmoid function fitted from the annual NDVI profile.
 128



130

131

132

133

134

135

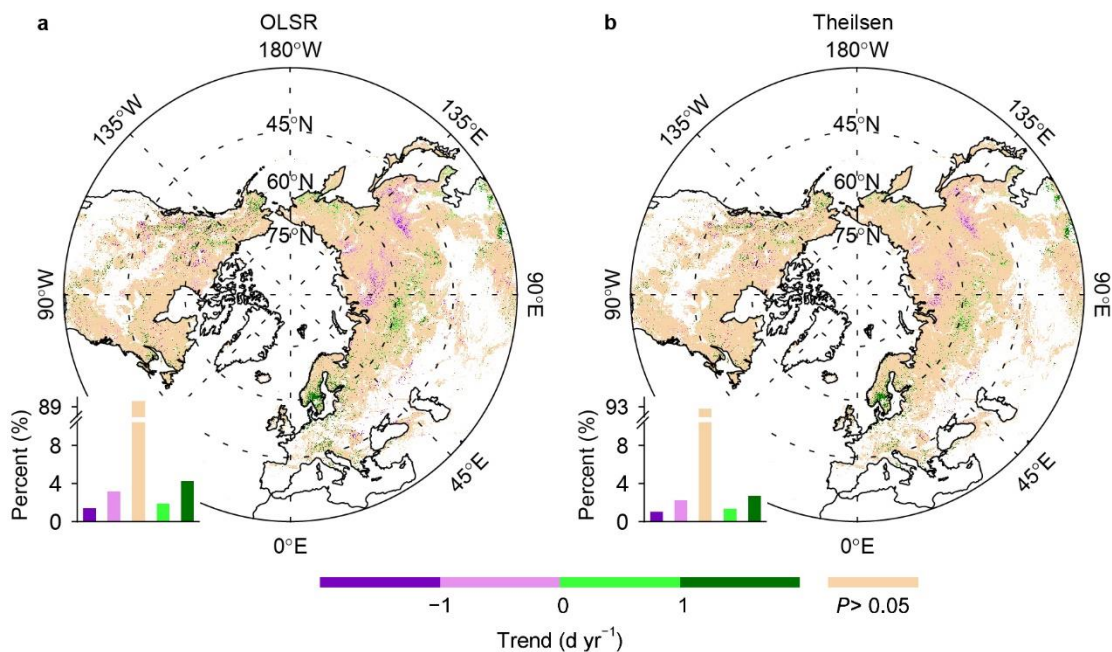
136

137

138

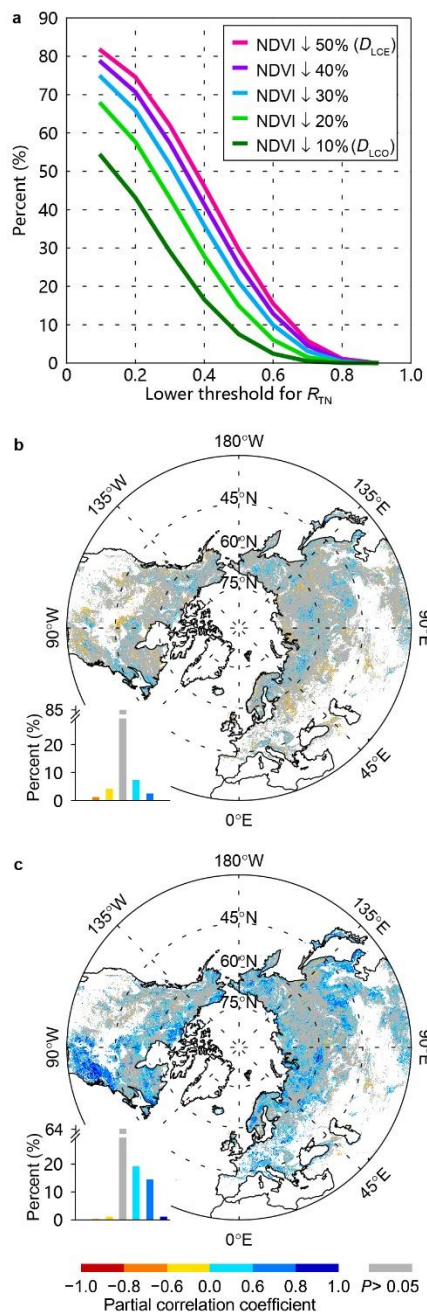
Figure S13. Spatial pattern of the partial correlation coefficient between the timing of different stages of leaf coloration and the mean daily minimum temperature for an optimized period preceding each stage for 2000–2018. The timings of different stages of leaf coloration are determined as the first dates when NDVI decreased by 20% (a), 30% (b), or 40% (c) of its annual amplitude in autumn. The bar chart in each panel shows the percentage of area for each interval of the partial correlation coefficient, with the coefficient value indicated by the color scale at the bottom. Non-significant correlations ($P > 0.05$) are in gray.

139
140



141
142 **Figure S14.** Temporal trends in the timing of onset of leaf coloration (D_{LCO}), retrieved from satellite
143 images for 2000–2018. The bar chart in each panel shows the percentage of area within each interval of
144 the significant ($P < 0.05$) temporal trends and the percentage of area with nonsignificant trends,
145 indicated by the color scale at the bottom. Positive and negative trend values refer to significantly
146 delayed and advanced D_{LCO} , respectively. For the pixels identified as deciduous broadleaved forests,
147 D_{LCO} was defined as the date when NDVI decreased by 10% of its annual amplitude from 1 August on
148 the basis of a generalized sigmoid function fitted from the annual NDVI profile; the maximum value
149 used to determine the annual amplitude was defined as the mean value of the upper quartile of the fitted
150 NDVI values in August. For the other pixels, D_{LCO} was defined as the date when NDVI decreased by 10%
151 of its annual amplitude; the maximum value of the fitted curve was used to determine the annual
152 amplitude. In (a), significant temporal trends were determined by using t -tests at $P < 0.05$ and OLSR
153 between D_{LCO} and the respective years. In (b), significant temporal trends were determined by using
154 Mann-Kendall tests at $P < 0.05$ and a Theil-Sen estimator between D_{LCO} and the respective years. Pixels
155 dominated by croplands or with low vegetation coverage, weak seasonality, or peak NDVI in October–
156 April were discarded.

157



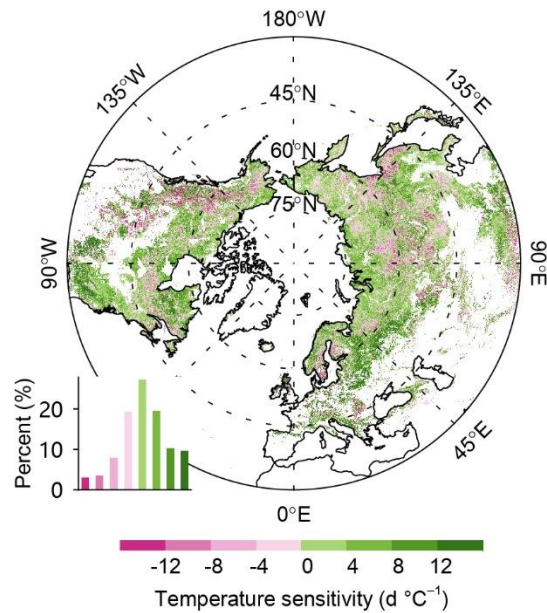
158
 159 **Figure S15.** Relationships between the timing of different stages of leaf coloration, as retrieved from
 160 satellite images, and the mean daily minimum temperature (T_{\min}) for an optimized period preceding the
 161 respective stage over the period 2000–2018. a, Percentage of area for which the partial correlation
 162 coefficient (R_{TN}) between the timing of a certain stage of leaf coloration (defined by NDVI decrease)
 163 and T_{\min} for an optimized period preceding the stage was higher than a certain threshold indicated by the
 164 horizontal axis. For example, R_{TN} for the onset of leaf coloration (D_{LCO} , 10% decrease in NDVI) is
 165 higher than 0.2 in about 40% of the area. b, Spatial pattern of the partial correlation coefficient between

166 D_{LCO} and pre- D_{LCO} T_{min} . c, Spatial pattern of the partial correlation coefficient between timing of the end
167 of leaf coloration (D_{LCE} , 50% decrease in NDVI) and pre- D_{LCE} T_{min} . For pixels identified as deciduous
168 broadleaved forests, D_{LCO} was defined as the date when NDVI decreased by 10% of its annual
169 amplitude from 1 August on the basis of a generalized sigmoid function fitted from the annual NDVI
170 profile. The maximum value used to determine the annual amplitude was defined as the mean value of
171 the upper quartile of the fitted NDVI values in August. For the other pixels, D_{LCO} was defined as the
172 date when NDVI decreased by 10% of its annual amplitude; the maximum value of the fitted curve was
173 used to determine the annual amplitude. The bar charts in (b) and (c) show the percentage of area for
174 each interval of the partial correlation coefficient ($P < 0.05$), with the coefficient indicated by the color
175 scale at the bottom. Nonsignificant correlations ($P > 0.05$) are in gray. Pixels dominated by croplands or
176 with low vegetation coverage, weak seasonality, or peak NDVI in October–April were discarded.

177

192 herbaceous vegetation, respectively. For the pixels identified as deciduous broadleaved forests, D_{LCO}
193 was defined as the date when NDVI decreased by 10% of its annual amplitude from 1 August on the
194 basis of a generalized sigmoid function fitted from the annual NDVI profile. The maximum value used
195 to determine the annual amplitude was defined as the mean value of the upper quartile of the fitted
196 NDVI values in August. For the other pixels, D_{LCO} was defined as the date when NDVI decreased by 10%
197 of its annual amplitude; the maximum value of the fitted curve was used to determine the annual
198 amplitude. Each cell represents 4 °C of temperature and 1.5 h of daylength. Only cells where the ratio of
199 the area of the cell to the total area is >1% are represented. Woody and herbaceous vegetation are
200 merged from Classes 1–6 and Class 10, respectively, in the MODIS land-cover product (MCD12C1,
201 Version 6) for 2009.

202



203

204

205

206

207

208

209

210

211

212

213

214

215

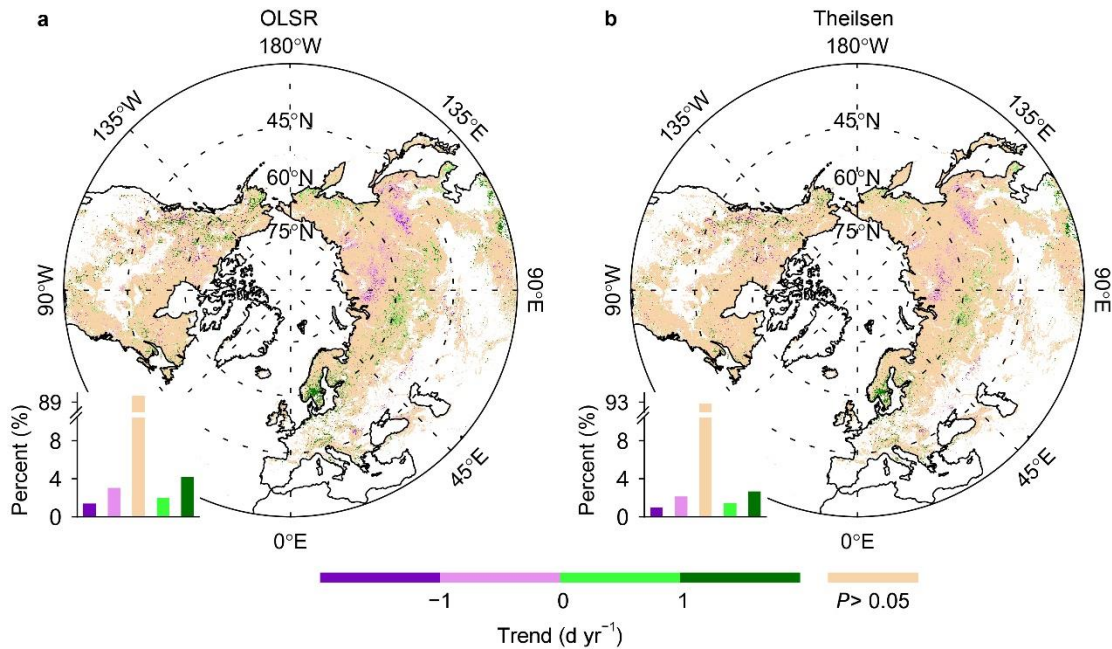
216

217

218

219

Figure S17. Difference in temperature sensitivity between the end and the onset of leaf coloration (D_{LCE} and D_{LCO}) over the period 2000–2018. The temperature sensitivity of D_{LCO} was defined as the coefficient for pre- D_{LCO} mean daily minimum temperature (T_{min}) in a linear regression in which D_{LCO} was set as the dependent variable and pre- D_{LCO} T_{min} and pre- D_{LCO} total precipitation were independent variables. The temperature sensitivity of D_{LCE} was calculated in a similar way. D_{LCO} and D_{LCE} were determined as the dates when NDVI decreased by 10% and 50%, respectively, of its annual amplitude based on a generalized sigmoid function fitted from the annual NDVI profile. For the pixels identified as deciduous broadleaved forests, D_{LCO} was defined as the date when NDVI decreased by 10% of its annual amplitude from 1 August, on the basis of a generalized sigmoid function fitted from the annual NDVI profile. The maximum value used to determine the annual amplitude was defined as the mean value of the upper quartile of the fitted NDVI values in August. For the other pixels, D_{LCO} was defined as the date when NDVI decreased by 10% of its annual amplitude; the maximum value of the fitted curve was used to determine the annual amplitude. The bar chart in the bottom-left corner shows the percentage of area for each interval of the temperature sensitivity indicated by the color scale at the bottom. Negative values (pink) indicate that D_{LCO} was more sensitive than D_{LCE} to temperature.



220

221

222

223

224

225

226

227

228

229

230

231

232

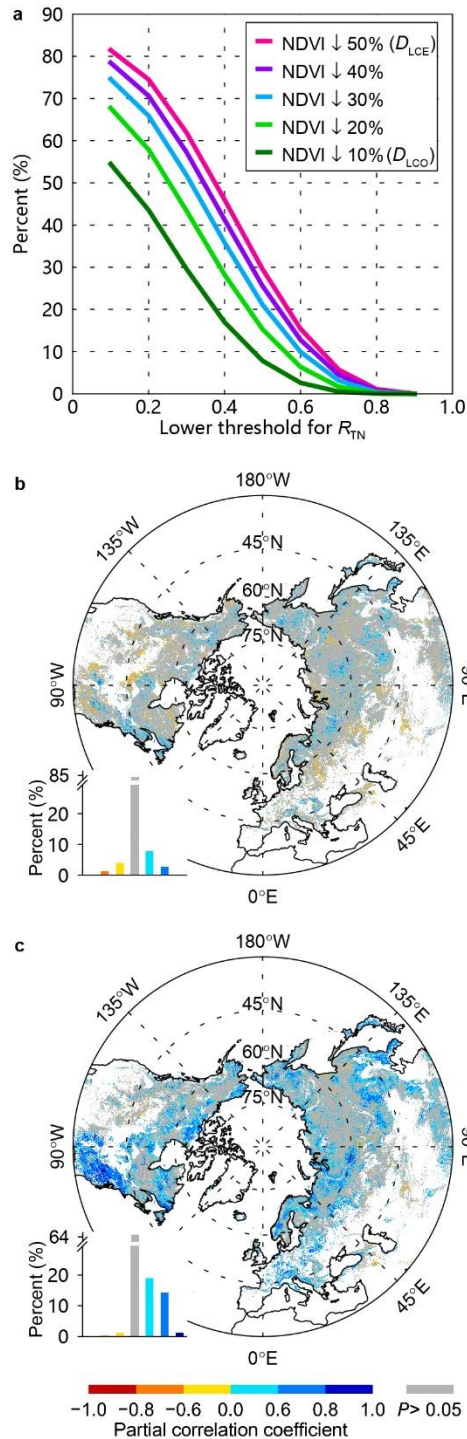
233

234

235

236

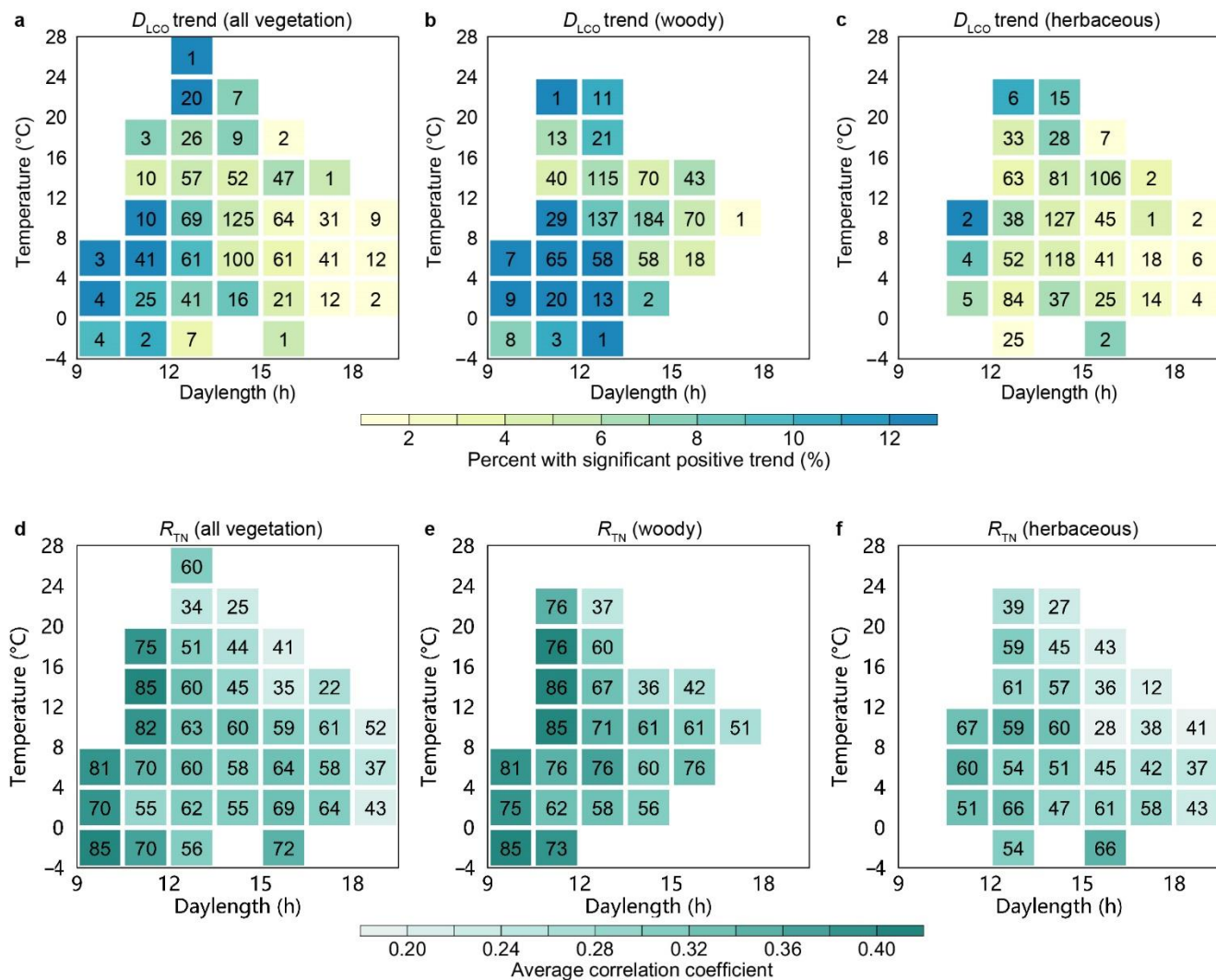
Figure S18. Temporal trends in the timing of onset of leaf coloration (D_{LCO}), as retrieved from satellite images for the period 2000–2018. The bar chart in each panel shows the percentage of area within each interval of the significant ($P < 0.05$) temporal trends and the percentage of area with nonsignificant trends, indicated by the color scale at the bottom. Positive and negative trend values refer to significantly delayed and advanced D_{LCO} , respectively. For the pixels identified as deciduous broadleaved forests, D_{LCO} was defined as the date when NDVI decreased by 10% of its annual amplitude from 16 August, on the basis of a generalized sigmoid function fitted from the annual NDVI profile. The maximum value used to determine the annual amplitude was defined as the mean value of the upper quartile of the fitted NDVI values in the second half of August. For the other pixels, D_{LCO} was defined as the date when NDVI decreased by 10% of its annual amplitude; the maximum value of the fitted curve was used to determine the annual amplitude. In (a), significant temporal trends were determined by using t -tests at $P < 0.05$ and OLSR between D_{LCO} and respective years. In (b), significant temporal trends were determined by using Mann-Kendall tests at $P < 0.05$ and a Theil-Sen estimator between D_{LCO} and the respective years. Pixels dominated by croplands or with low vegetation coverage, weak seasonality, or peak NDVI in October–April were discarded.



237
 238 **Figure S19.** Relationships between the timing of different stages of leaf coloration, as retrieved from
 239 satellite images, and the mean daily minimum temperature (T_{min}) for an optimized period preceding the
 240 respective stage over the period 2000–2018. a, Percentage of area for which the partial correlation
 241 coefficient (R_{TN}) between the timing of a given stage of leaf coloration (defined by NDVI decrease) and
 242 T_{min} for an optimized period preceding the stage was higher than a given threshold, indicated by the

243 horizontal axis. For example, R_{TN} for the onset of leaf coloration (D_{LCO} , 10% decrease in NDVI) is
244 higher than 0.2 in about 40% of the area. b, Spatial pattern of the partial correlation coefficient between
245 D_{LCO} and pre- $D_{LCO} T_{min}$. c, Spatial pattern of the partial correlation coefficient between timing of the end
246 of leaf coloration (D_{LCE} , 50% decrease in NDVI) and pre- $D_{LCE} T_{min}$. For the pixels identified as
247 deciduous broadleaved forests, D_{LCO} was defined as the date when NDVI decreased by 10% of its
248 annual amplitude from 16 August, on the basis of a generalized sigmoid function fitted from the annual
249 NDVI profile. The maximum value used to determine the annual amplitude was defined as the mean
250 value of the upper quartile of the fitted NDVI values in the second half of August. For the other pixels,
251 D_{LCO} was defined as the date when NDVI decreased by 10% of its annual amplitude; the maximum
252 value of the fitted curve was used to determine the annual amplitude. The bar charts in (b) and (c) show
253 the percentage of area for each interval of the partial correlation coefficient ($P < 0.05$), with the
254 coefficient indicated by the color scale at the bottom. Non-significant correlations ($P > 0.05$) are in gray.
255 Pixels dominated by croplands or with low vegetation coverage, weak seasonality, or peak NDVI in
256 October–April were discarded.

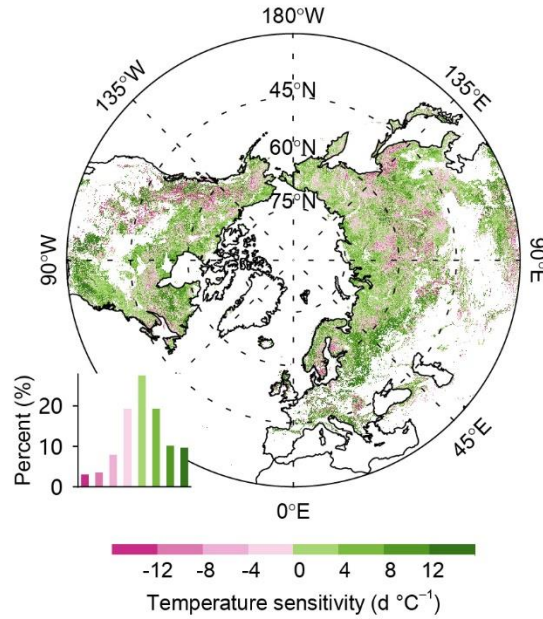
257



258
 259 **Figure S20.** Dependence of temporal trends in the timing of onset of leaf coloration (D_{LCO} , a–c) and of
 260 the partial correlation coefficient (R_{TN} , d–f) between D_{LCO} and pre- D_{LCO} mean daily minimum
 261 temperature (T_{min}) on daylength and temperature at D_{LCO} over the period 2000–2018. Daylength
 262 (indicated by the horizontal axis) was calculated for each pixel (location) at multiyear mean D_{LCO} over
 263 the period 2000–2018 ($D_{LCO-MEAN}$), and temperature (indicated by the vertical axis) is the mean daily
 264 minimum temperature of the month preceding $D_{LCO-MEAN}$. a, Color indicates the percentage of area with
 265 significant ($P < 0.05$) D_{LCO} delays in each cell (i.e., a specific temperature \times daylength combination), as
 266 indicated by the color scale at the bottom. The number in each cell indicates the ratio (unit: %) of the
 267 area in each cell to the total area with D_{LCO} retrieval (i.e., Northern Hemisphere from 30°N–75°N). The
 268 temporal trends and their significances were determined by ordinary least squares regression and t -tests.
 269 b and c, The same as (a) but for woody and herbaceous vegetation, respectively. d, Color indicates the
 270 average of the positive R_{TN} , as indicated by the color scale at the bottom. The number indicates the

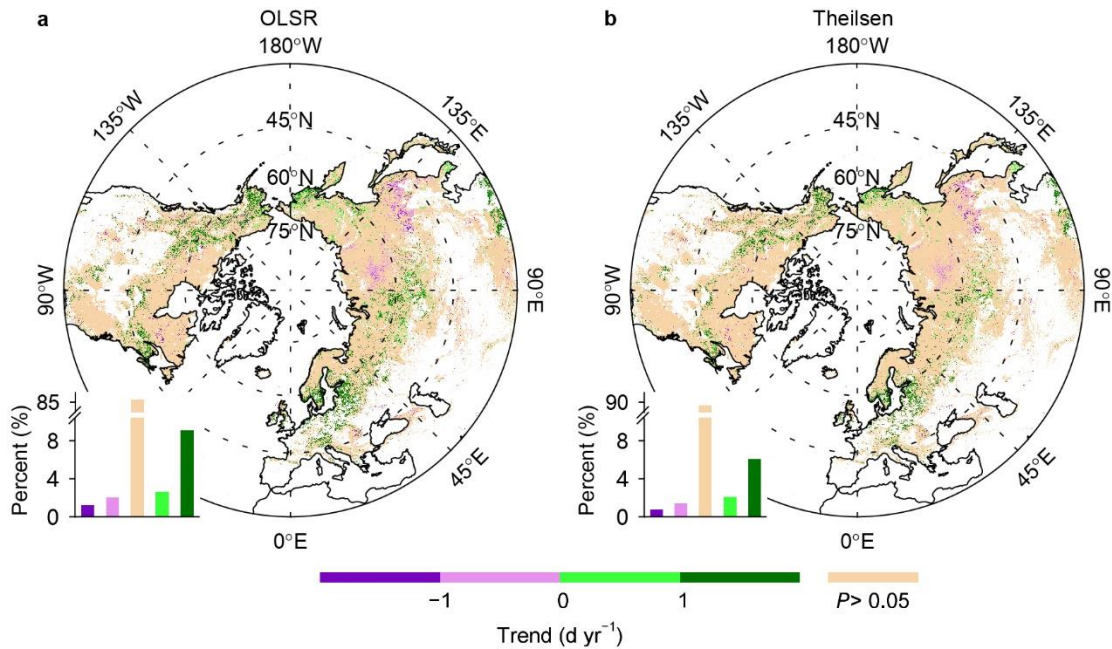
271 percentage of area with a positive correlation in each cell. e and f, The same as (d) but for woody and
272 herbaceous vegetation, respectively. For the pixels identified as deciduous broadleaved forests, D_{LCO}
273 was defined as the date when NDVI decreased by 10% of its annual amplitude from 16 August, on the
274 basis of a generalized sigmoid function fitted from the annual NDVI profile. The maximum value used
275 to determine the annual amplitude was defined as the mean value of the upper quartile of the fitted
276 NDVI values in the second half of August. For the other pixels, D_{LCO} was defined as the date when
277 NDVI decreased by 10% of its annual amplitude; the maximum value of the fitted curve was used to
278 determine the annual amplitude. Each cell represents 4 °C of temperature and 1.5 h of daylength. Only
279 cells where the ratio of the area of the cell to the total area is >1‰ are represented. Woody and
280 herbaceous vegetation are merged from Classes 1–6 and Class 10, respectively, in the MODIS land-
281 cover product (MCD12C1, Version 6) for 2009.

282
283

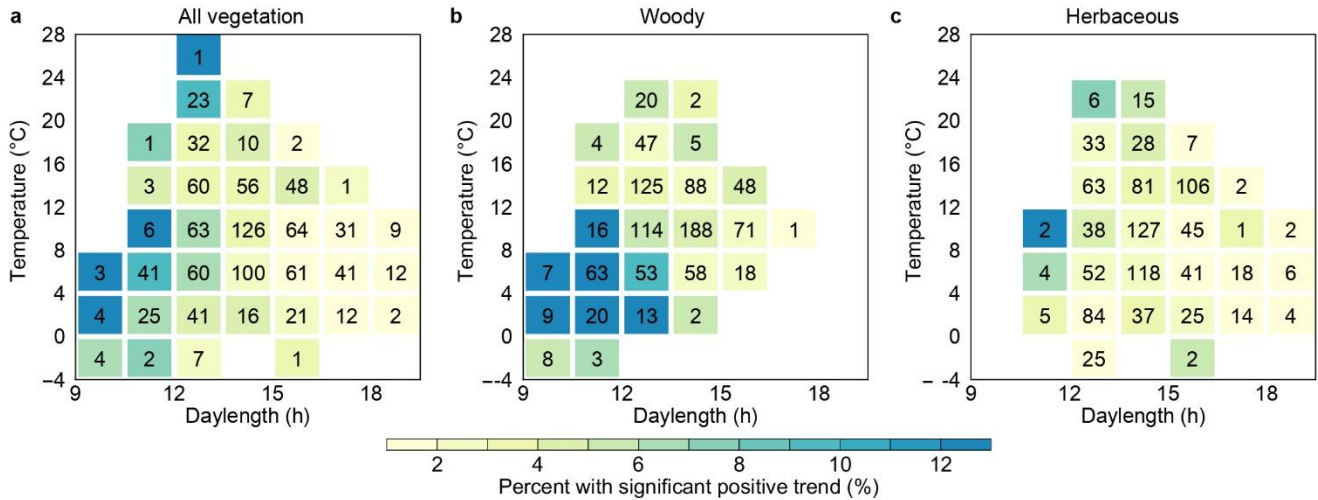


284
 285 **Figure S21.** Difference in temperature sensitivity between the end and the onset of leaf coloration (D_{LCE}
 286 and D_{LCO}) over the period 2000–2018. The temperature sensitivity of D_{LCO} was defined as the coefficient
 287 for pre- D_{LCO} mean daily minimum temperature (T_{min}) in the linear regression in which D_{LCO} was set as
 288 the dependent variable and pre- D_{LCO} T_{min} and pre- D_{LCO} total precipitation were independent variables.
 289 The temperature sensitivity of D_{LCE} was calculated in a similar way. D_{LCO} and D_{LCE} were determined as
 290 the dates when NDVI decreased by 10% and 50%, respectively, of its annual amplitude, on the basis of
 291 a generalized sigmoid function fitted from the annual NDVI profile. For the pixels identified as
 292 deciduous broadleaved forests, D_{LCO} was defined as the date when NDVI decreased by 10% of its
 293 annual amplitude from 16 August, on the basis of a generalized sigmoid function fitted from the annual
 294 NDVI profile, The maximum value used to determine the annual amplitude was defined as the mean
 295 value of the upper quartile of the fitted NDVI values in the second half of August. For the other pixels,
 296 D_{LCO} was defined as the date when NDVI decreased by 10% of its annual amplitude; the maximum
 297 value of the fitted curve was used to determine the annual amplitude. The bar chart in the bottom-left
 298 corner shows the percentage of area for each interval of the temperature sensitivity indicated by the
 299 color scale at the bottom. Negative values (pink) indicate that D_{LCO} was more sensitive than D_{LCE} to
 300 temperature.

301



302
 303 **Figure S22.** Temporal trends in the timing of onset of leaf coloration (D_{LCO}), as retrieved from satellite
 304 images for 2000–2018. The bar chart in each panel shows the percentage of area within each interval of
 305 the significant ($P < 0.05$) temporal trends and the percentage of area with nonsignificant trends,
 306 indicated by the color scale at the bottom. Positive and negative trend values refer to significantly
 307 delayed and advanced D_{LCO} , respectively. D_{LCO} was determined as the date when the rate of change of
 308 the curvature (RCC) of the fitted NDVI curve reached its first local minimum value in the descending
 309 period. For the pixels identified as deciduous broadleaved forests, the fitting function was a modified
 310 double logistic function that considered summer NDVI green-down (Elmore *et al.*, 2012), whereas the
 311 fitting function was a double logistic function for the other pixels(Beck *et al.*, 2006). In (a), significant
 312 temporal trends were determined by using t -tests at $P < 0.05$ and OLSR between D_{LCO} and the respective
 313 years. In (b), significant temporal trends were determined by using Mann-Kendall tests at $P < 0.05$ and a
 314 Theil-Sen estimator between D_{LCO} and the respective years. Pixels dominated by croplands or with low
 315 vegetation coverage, weak seasonality, or peak NDVI in October–April were discarded.

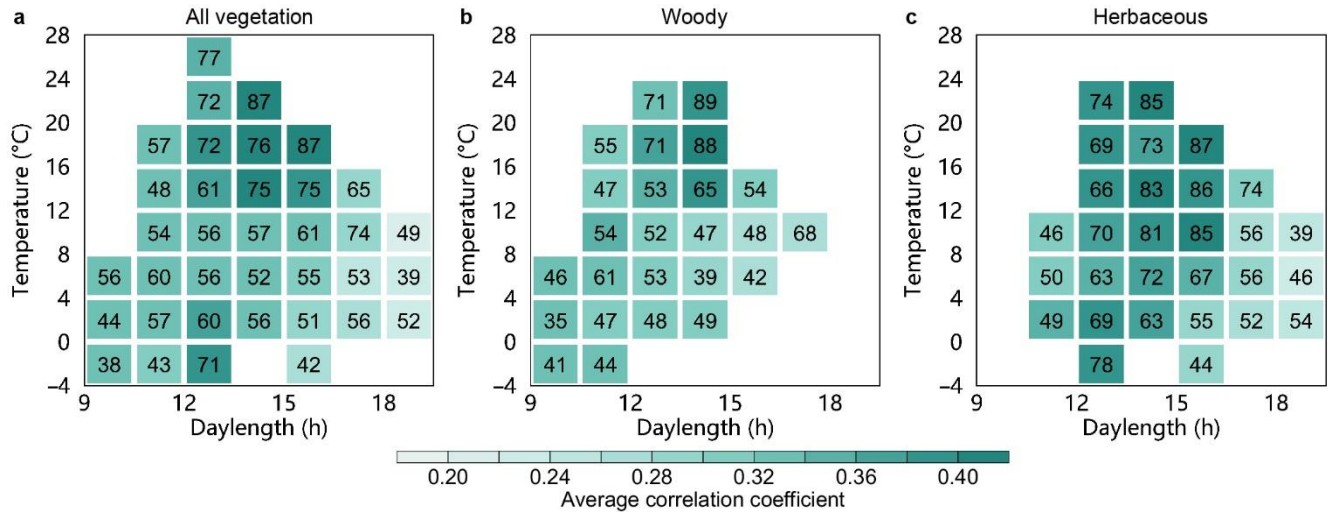


316

317

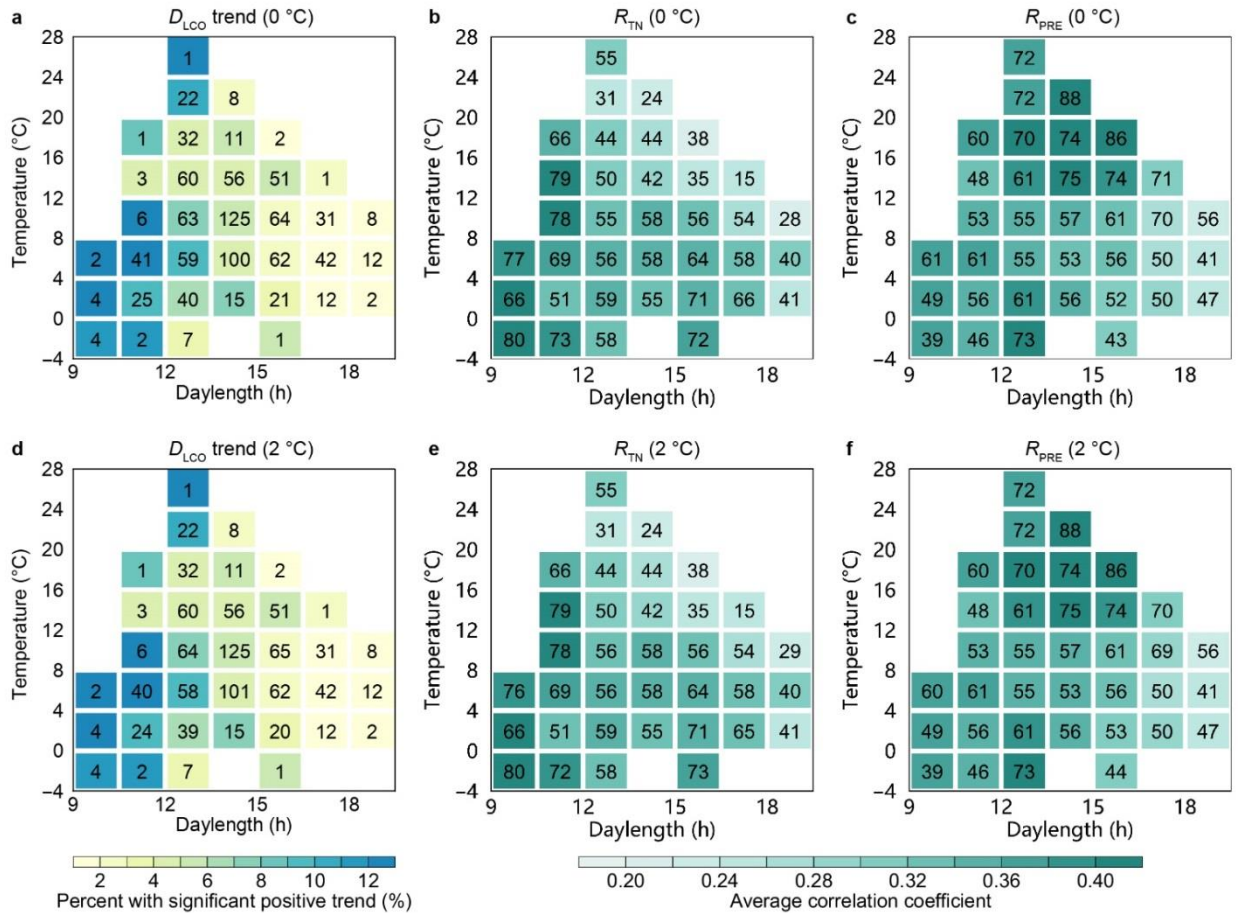
Figure S23. Dependence of temporal trends in the timing of onset of leaf coloration (D_{LCO}) on daylength and temperature at D_{LCO} over the period 2000–2018 for all (a), woody (b), and herbaceous (c) vegetation. The daylength (indicated by the horizontal axis) was calculated for each pixel (location) at multiyear mean D_{LCO} over the period 2000–2018 ($D_{LCO-MEAN}$), and the temperature (indicated by the vertical axis) is the mean daily minimum temperature of the month preceding $D_{LCO-MEAN}$. a, Color indicates the percentage of area with significant ($P < 0.05$) D_{LCO} delays in each cell (i.e., a specific temperature \times daylength combination), as indicated by the color scale at the bottom. The number in each cell indicates the ratio (unit: %) of the area in each cell to the total area with D_{LCO} retrieval (i.e., Northern Hemisphere from 30°N–75°N). Temporal trends and their significances were determined by using the Theil-Sen estimator and Mann-Kendall tests. b and c, The same as (a), but for woody and herbaceous vegetation, respectively. Each cell represents 4 °C of temperature and 1.5 h of daylength. Only cells where the ratio of the area of the cell to the total area is $>1\%$ are represented. Woody and herbaceous vegetation are merged from Classes 1–6 and Class 10, respectively, in the MODIS land-cover product (MCD12C1, Version 6) for 2009.

331



332
 333 **Figure S24.** Dependence of the partial correlation coefficient (R_{PRE}) between the timing of onset of leaf
 334 coloration (D_{LCO}) and pre- D_{LCO} total precipitation on daylength and temperature at D_{LCO} over the period
 335 2000–2018 for all (a), woody (b), and herbaceous (c) vegetation. Daylength (indicated by the horizontal
 336 axis) was calculated for each pixel (location) at multiyear mean D_{LCO} over the period 2000–2018 (D_{LCO-}
 337 $MEAN$), and temperature (indicated by the vertical axis) is the mean daily minimum temperature of the
 338 month preceding $D_{LCO-}MEAN$. a, Color indicates the average of the positive R_{PRE} , as indicated by the color
 339 scale at the bottom. The number indicates the percentage of area with a positive correlation in each cell
 340 (i.e., a specific temperature \times daylength combination); b and c, The same as (a), but for woody and
 341 herbaceous vegetation, respectively. Each cell represents 4 °C of temperature and 1.5 h of daylength.
 342 Only cells where the ratio of the area of the cell to the total area is $>1\%$ are represented. Woody and
 343 herbaceous vegetation are merged from Classes 1–6, and Class 10 in the MODIS land-cover product
 344 (MCD12C1, Version 6) for 2009.

345



346

347

348

349

350

351

352

353

354

355

356

357

358

359

360

361

362

Figure S25. Dependence of temporal trends in the timing of onset of leaf coloration (D_{LCO} , a and d), of the partial correlation coefficient (R_{TN} , b and e) between D_{LCO} and pre- D_{LCO} mean daily minimum temperature, and of the partial correlation coefficient (R_{PRE} , c and f) between D_{LCO} and pre- D_{LCO} total precipitation on daylength and temperature at D_{LCO} over the period 2000–2016 after the exclusion of years with cold events before D_{LCO} . Daylength (indicated by the horizontal axis) was calculated for each pixel (location) at multiyear mean D_{LCO} over the period 2000–2016 ($D_{LCO-_{MEAN}}$), and temperature (indicated by the vertical axis) is the mean daily minimum temperature of the month preceding $D_{LCO-_{MEAN}}$. Cold events were determined mainly by using a threshold-based method with a daily minimum temperature of 0 °C (a–c) or 2 °C (d–f). a and d, Color indicates the percentage of area with significant ($P < 0.05$) D_{LCO} delays in each cell (i.e., a specific temperature \times daylength combination), as indicated by the color scale at the bottom. The number in each cell indicates the ratio (unit: %) of the area in each cell to the total area with D_{LCO} retrieval (i.e., Northern Hemisphere from 30°N–75°N). b and e, Color indicates the average of the positive R_{TN} , as indicated by the color scale at the bottom. The number indicates the percentage of area with a positive correlation in each cell. c and f, The same as (b and e), but for the positive R_{PRE} . Each cell represents 4 °C of temperature and 1.5 h of daylength. Only cells where the ratio of the area of the cell to the total area is $>1\%$ are represented.

364
365 **Table S1.** Experiments on photoperiodic control of plant growth.

Species	Life-form	Findings from experiments	Experimental setting	Reference
<i>Acer rubrum</i> L.	Deciduous tree	Growth stopped after about four weeks of short photoperiod treatment (8 hours).	Chamber cultivating +controlled photoperiod	Downs and Borthwick (1956)
<i>Acer saccharum</i> Marsh.	Deciduous tree	Long photoperiod treatment (16 hours) resulted in delayed senescence and abscission for up to five months.	Chamber cultivating +controlled photoperiod	Olmsted (1951)
<i>Aesculus hippocastanum</i> L.	Deciduous tree	Growth stopped after about four weeks of short photoperiod treatment (8 hours).	Chamber cultivating +controlled photoperiod	Downs and Borthwick (1956)
<i>Betula mandshurica</i> [Regel] Nakai.	Deciduous tree	Growth stopped after about four weeks of short photoperiod treatment (8 hours).	Chamber cultivating +controlled photoperiod	Downs and Borthwick (1956)
<i>Betula pubescens</i> Ehrh.	Deciduous tree	Elongation growth ceased after 7–8 days of short photoperiod treatment (12 hours).	Chamber cultivating +controlled photoperiod	Rinne <i>et al.</i> (1994)
<i>Catalpa bignonioides</i> Walt.	Deciduous tree	Growth stopped after about four weeks of short photoperiod treatment (8 hours).	Chamber cultivating +controlled photoperiod	Downs and Borthwick (1956)
<i>Catalpa speciosa</i> Warder	Deciduous tree	Growth stopped after about four weeks of short photoperiod treatment (8 hours).	Chamber cultivating +controlled photoperiod	Downs and Borthwick (1956)
<i>Cornus florida</i> L.	Deciduous tree	Growth stopped after about four weeks of short photoperiod treatment (8 hours).	Chamber cultivating +controlled photoperiod	Downs and Borthwick (1956)
<i>Liquidambar styraciflua</i> L.	Deciduous tree	Growth stopped after about four weeks of short photoperiod treatment (8 hours).	Chamber cultivating +controlled photoperiod	Downs and Borthwick (1956)
<i>Liquidambar styraciflua</i> L.	Deciduous tree	The plant grew nearly all winter under a 16 hours photoperiod.	Chamber cultivating +controlled photoperiod	Kramer (1936)
<i>Liriodendron tulipifera</i> L.	Deciduous tree	Growth stopped after about ten days of short photoperiod treatment (8 hours).	Chamber cultivating +controlled photoperiod	Downs and Borthwick (1956)
<i>Liriodendron tulipifera</i> L.	Deciduous tree	The plant grew all winter under a 16 hours photoperiod.	Chamber cultivating +controlled photoperiod	Kramer (1936)
<i>Paulownia tomentosa</i> [Thunb.] Steud.	Deciduous tree	Growth stopped after about four weeks of short photoperiod treatment (8 hours).	Chamber cultivating +controlled photoperiod	Downs and Borthwick (1956)
<i>Populus trichocarpa</i> Torr. & Gray	Deciduous tree	Plant set bud after 18 days of short photoperiod treatment (13 hours), which is regulated by phytochrome.	Stem cutting + controlled photoperiod	Howe <i>et al.</i> (1996)

Species	Life-form	Findings from experiments	Experimental setting	Reference
<i>Populus tremula</i>	Deciduous tree	Shortening photoperiod was the main trigger for the initiation of autumn senescence.	Chamber cultivating +controlled photoperiod	Fracheboud <i>et al.</i> (2009)
<i>Populus tremula</i>	Deciduous tree	Photoperiod is the sole trigger for the onset of autumn senescence.	Observation under natural conditions	Keskitalo <i>et al.</i> (2005)
<i>Populus tremula x tremuloides</i>	Deciduous tree	When plants are shifted from long days (16 hours) to short days (8 hours), they respond by growth cessation and bud set after 32 days.	Chamber cultivating +controlled photoperiod	Böhlenius <i>et al.</i> (2006)
<i>Ulmus americana</i> L.	Deciduous tree	Growth stopped after about twenty weeks of short photoperiod treatment (8 hours).	Chamber cultivating +controlled photoperiod	Downs and Borthwick (1956)
<i>Picea abies</i> (L.) Karst.	Evergreen tree	Growth cessation occurred within two weeks after exposure to short photoperiods (≤ 15 hours).	Chamber cultivating +controlled photoperiod	Heide (1974)
<i>Picea glauca</i> (Moench) Voss	Evergreen tree	Growth cessation occurred after five weeks of short photoperiod treatment (8 hours) under warm temperature conditions.	Chamber cultivating +controlled photoperiod	Hamilton <i>et al.</i> (2016)
<i>Pinus sylvestris</i> L.	Evergreen tree	Northern populations grown under 50°N photoperiod (shorter) stopped growth earlier than that under 60°N photoperiod (longer).	Chamber cultivating +controlled photoperiod	Oleksyn <i>et al.</i> (1992)
<i>Pinus sylvestris</i> L.	Evergreen tree	Growth stopped after about four weeks of short photoperiod treatment (8 hours).	Chamber cultivating +controlled photoperiod	Downs and Borthwick (1956)
<i>Pinus taeda</i> L.	Evergreen tree	Growth stopped after about four weeks of short photoperiod treatment (8 hours).	Chamber cultivating +controlled photoperiod	Downs and Borthwick (1956)
<i>Pinus taeda</i> L.	Evergreen tree	The plant grew all winter with a 14.5 hours photoperiod.	Chamber cultivating +controlled photoperiod	Kramer (1936)
<i>Pinus virginiana</i> Mill.	Evergreen tree	Growth stopped after about four weeks of short photoperiod treatment (8 hours).	Chamber cultivating +controlled photoperiod	Downs and Borthwick (1956)
<i>Salix pentandra</i> L.	Deciduous small tree or shrub	Short photoperiod (≤ 22 hours for a northern ecotype and ≤ 15 hours for a southern ecotype) induced apical growth cessation.	Chamber cultivating +controlled photoperiod	Junttila (1980)
<i>Salix polaris</i> L.	Deciduous small tree or shrub	Leaf abscission in the arctic ecotype was stimulated by short photoperiod when grown at 15°C.	Collected with roots + controlled photoperiod	Paus <i>et al.</i> (1986)
<i>Syringa vulgaris</i> L.	Deciduous small tree or shrub	Photosynthetic efficiency has a more consistent relationship with photoperiod than with temperature.	Observation under natural conditions	Aikio <i>et al.</i> (2019)

Species	Life-form	Findings from experiments	Experimental setting	Reference
<i>Hibiscus rosa-sinensis</i> L.	Evergreen small tree or shrub	Leaves under long photoperiod treatment (16 hours) spend ten more days to complete senescence than that under short photoperiod treatment (8 hours).	Leaves cutting + controlled photoperiod	Misra and Biswal (1973)
<i>Hibiscus syriacus</i> L.	Deciduous shrub	Short photoperiod (8 hours) induced dormancy while long photoperiod (16 hours) delayed dormancy and resulted in considerable winter injury	Chamber cultivating +controlled photoperiod	Davidson (1957)
<i>Weigela florida</i> A. DC.	Deciduous shrub	Short photoperiod (8 hours) induced dormancy while long photoperiod (16 hours) delayed dormancy and resulted in considerable winter injury.	Chamber cultivating +controlled photoperiod	Davidson (1957)
<i>Rhododendron catawbiense</i> Michx.	Evergreen shrub	Short photoperiod (8 hours) induced dormancy while long photoperiod (16 hours) delayed dormancy and resulted in considerable winter injury.	Chamber cultivating +controlled photoperiod	Davidson (1957)
<i>Cucurbita pepo</i> Linn.	Herbaceous	After three months of growth, much larger percentage of mesophyll cell death was detected in short photoperiod (9 hours) than that in long photoperiod (18 hours).	Chamber cultivating +controlled photoperiod	Wang <i>et al.</i> (2002)
<i>Sedum telephium</i> L. subsp. <i>maximum</i> (L.) Krockner	Herbaceous	After eight weeks of growth, plants in long photoperiod (24 hours) elongated rapidly while those in short photoperiod (10 hours) became dormant.	Chamber cultivating +controlled photoperiod	Heide (2001)
<i>Vitis labruscana</i> Bailey	Herbaceous	Cane elongation was less in response to short photoperiod treatments (12 or 13 hours), as compared to natural photoperiod (13.7 or 14.3 hours).	Stem cutting + controlled photoperiod	Fennell and Hoover (1991)
<i>Vitis riparia</i> Michx.	Herbaceous	Cane elongation was less in response to short photoperiod treatments (12 or 13 hours), as compared to natural photoperiod (13.7 or 14.3 hours).	Stem cutting + controlled photoperiod	Fennell and Hoover (1991)

366
367

368 **Table S2.** *In situ* observations in China used in this study.

Site Name	Latitude	Longitude	Species number	Start year	End year	Year length
Nunkiang	49	125	5	1975±0	1993±4	17±4
Wudalianchi	48	126	11	1976±3	1995±3	18±3
Kiamusze	47	130	6	1981±1	1996±0	16±1
Minqin	38	103	29	1981±1	1996±1	12±1
Hohhot	41	112	10	1981±2	1996±1	13±2
Mutankiang	44	130	41	1980±2	1996±2	13±2
Beijing	40	116	42	1972±1	1994±3	20±4
Chengteh	41	118	5	1983±2	1996±0	12±1
Qinhuangdao	39	119	15	1980±0	1993±0	13±1
Gaizhou	40	122	12	1979±1	1996±0	17±1
Yixian	39	115	17	1980±0	1993±0	12±1
Liaocheng	36	115	5	1974±4	1993±2	15±3
Tyan	36	117	5	1974±0	1986±0	11±0
Sian	34	109	33	1977±3	1994±3	15±3
Luoyang	35	113	27	1977±4	1996±1	18±4
Yancheng	33	120	19	1981±4	1996±0	15±3
Zhengjiang	32	119	15	1976±3	1993±2	17±3
Hefei	32	117	19	1979±1	1995±1	17±2
Wuhu	31	118	16	1982±1	1996±0	13±1

369 The mean ± standard deviation of start year, end year and length of time series are provided for each site.

370

371 **Table S3.** FLUXNET2015 flux tower sites used in this study.

Fluxnet ID	Vegetation type	Latitude	Longitude	Year range	Reference
BE-Bra	Mixed Forests	51.31	4.52	1999-2002,2004-2014	Janssens (2016)
BE-Vie	Mixed Forests	50.31	6.00	1996-2014	De Ligne <i>et al.</i> (2016)
CA-Gro	Mixed Forests	48.22	-82.16	2003-2013	McCaughey (2016)
CA-Man	Evergreen Needleleaf Forest	55.88	-98.48	1994-2004,2006-2008	Amiro (2016)
CA-Oas	Mixed Forests	53.63	-106.20	1996-2010	Black (2016b)
CA-Obs	Evergreen Needleleaf Forest	53.99	-105.12	1999-2010	Black (2016a)
CA-TP3	Mixed Forests	42.71	-80.35	2003-2014	Arain (2016b)
CA-TP4	Mixed Forests	42.71	-80.36	2002-2014	Arain (2016a)
CH-Dav	Evergreen Needleleaf Forest	46.82	9.86	1997-2014	Hörtnagl <i>et al.</i> (2016b)
CH-Lae	Mixed Forests	47.48	8.37	2004-2014	Hörtnagl <i>et al.</i> (2016a)
CZ-BK1	Evergreen Needleleaf Forest	49.50	18.54	2004-2014	Šigut <i>et al.</i> (2016)
DE-Gri	Mixed Forests	50.95	13.51	2004-2014	Bernhofer <i>et al.</i> (2016b)
DE-Hai	Mixed Forests	51.08	10.45	2000-2012	Knohl <i>et al.</i> (2016)
DE-Tha	Evergreen Needleleaf Forest	50.96	13.57	1996-2014	Bernhofer <i>et al.</i> (2016a)
DK-Sor	Deciduous Broadleaf Forest	55.49	11.64	1996-2014	Ibrom and Pilegaard (2016)
DK-ZaH	Open Shrublands	74.47	-20.55	2000-2010,2012-2014	Lund <i>et al.</i> (2016)
FI-Hyy	Evergreen Needleleaf Forest	61.85	24.30	1996-2014	Mammarella <i>et al.</i> (2016)
FI-Sod	Evergreen Needleleaf Forest	67.36	26.64	2001-2014	Aurela <i>et al.</i> (2016)
FR-Fon	Deciduous Broadleaf Forest	48.48	2.78	2005-2014	Berveiller <i>et al.</i> (2016)
IT-Col	Deciduous Broadleaf Forest	41.85	13.59	1997-2002,2004-2014	Matteucci (2016)
IT-Lav	Evergreen Needleleaf Forest	45.96	11.28	2003-2014	Gianelle <i>et al.</i> (2016b)
IT-MBo	Grasslands	46.01	11.05	2003-2013	Gianelle <i>et al.</i> (2016a)
IT-Ren	Evergreen Needleleaf Forest	46.59	11.43	1999,2002-2003,2005-2013	Minerbi and Montagnani (2016)
NL-Loo	Evergreen Needleleaf Forest	52.17	5.74	1996-2014	Moors and Elbers (2016)
RU-Cok	Open Shrublands	70.83	147.49	2003-2013	Dolman <i>et al.</i> (2016)
RU-Fyo	Mixed Forests	56.46	32.92	1998-2014	Varlagin <i>et al.</i> (2016)
US-GLE	Evergreen Needleleaf Forest	41.36	-106.24	2005-2014	Massman (2016)
US-Ha1	Mixed Forests	42.54	-72.17	1992-2012	Munger (2016)
US-MMS	Deciduous Broadleaf Forest	39.32	-86.41	1999-2014	Novick and Phillips (2016)
US-Me2	Evergreen Needleleaf Forest	44.45	-121.56	2002-2014	Law (2016)
US-NR1	Evergreen Needleleaf Forest	40.03	-105.55	1999-2014	Blanken (2016)
US-Oho	Deciduous Broadleaf Forest	41.55	-83.84	2004-2013	Chen (2016)
US-PFa	Mixed Forests	45.95	-90.27	1996-2014	Desai (2016)
US-SRM	Open Shrublands	31.82	-110.87	2004-2014	Scott (2016a)
US-UMB	Deciduous Broadleaf Forest	45.56	-84.71	2000-2014	Gough <i>et al.</i> (2016)
US-Wkg	Grasslands	31.74	-109.94	2004-2014	Scott (2016b)

373 **Table S4.** Proportions of years with cold events before D_{LCO} (for satellite and *in situ* observations) and
 374 before D_{PDO} (for FLUXNET2015).

Metrics	Satellite D_{LCO} (2000–2016)	<i>in situ</i> D_{LCO} China	FLUXNET2015 D_{PDO}
Proportion (%) of years with cold events (0 °C)	1	2	1
Proportion (%) of years with cold events (2 °C)	2	3	1

375 D_{PDO} , timing of onset of the decrease in maximum canopy photosynthetic capacity in autumn; D_{LCO} , timing of onset of leaf
 376 coloration in autumn. Cold events were determined mainly by using a threshold-based method with a daily minimum
 377 temperature of 0 °C or 2 °C.
 378

379 **Table S5.** Percentage of time series for each interval of the temporal trend in D_{LCO} before and after the
 380 exclusion of years with cold events.

Metrics	Number of time-series	Cold events	Interval of significant temporal trend ($d\ y^{-1}$) ($P < 0.05$)				$P > 0.05$
			<-1	[-1, 0)	(0, 1]	>1	
Satellite D_{LCO} (2000–2016)	2.01×10^6	Not excluded	2	2	2	4	90
		Excluded (0 °C)	2	2	2	4	90
		Excluded (2 °C)	2	2	1	5	90
<i>in situ</i> D_{LCO} China	326	Not excluded	12	4	4	6	74
		Excluded (0 °C)	12	4	5	6	73
		Excluded (2 °C)	12	3	5	7	73

381 D_{LCO} , timing of onset of leaf coloration in autumn. Temporal trends were determined by using the ordinary least squares
 382 regression between D_{LCO} and the respective years, with t -tests. Only time series with at least 10 continuous years of data after
 383 exclusion of years with cold events were included. Cold events were determined mainly by using a threshold-based method
 384 with a daily minimum temperature of 0 °C or 2 °C. Data in the farthest right column indicate the percentage of area or time-
 385 series with a non-significant trend.
 386

387 **Table S6.** Percentage of time series for each interval of the temporal trend in D_{LCO} .

Metrics	Number of time-series	Interval of significant temporal trend ($d\ y^{-1}$) ($P < 0.05$)				$P > 0.05$
		<-1	$[-1, 0)$	$(0, 1]$	>1	
Satellite D_{LCO} (2000–2018)	2.07×10^6	1	2	1	3	93
<i>in situ</i> D_{LCO} China	332	8	2	3	3	84

388 D_{LCO} , timing of the onset of leaf coloration in autumn. Temporal trends were determined by using the Theil-Sen estimator
 389 between D_{LCO} and the respective years, with Mann-Kendall tests. Data in the farthest right column indicate the percentage of
 390 area or time-series with a non-significant trend.
 391

392 **Table S7.** Percentage of correlations between D_{LCO} or D_{PDO} and each climate factor for each interval of
 393 the partial correlation coefficient before and after the exclusion of years with cold events.

Metrics	Climatic Factor	Cold Events	Interval of the partial correlation coefficient ($P < 0.05$)					$P > 0.05$	
			[-1.0, -0.8)	[-0.8, -0.6)	[-0.6, 0)	(0, 0.6]	(0.6, 0.8]		(0.8, 1.0]
Satellite D_{LCO} (2000–2016)	Temperature	Not excluded	0	2	4	5	3	0	86
		Excluded (0 °C)	0	2	4	5	3	0	86
		Excluded (2 °C)	0	2	4	5	3	0	86
	Precipitation	Not excluded	0	2	3	7	5	0	83
		Excluded (0 °C)	0	2	3	7	5	0	83
		Excluded (2 °C)	0	2	3	7	5	0	83
<i>in situ</i> D_{LCO} China	Temperature	Not excluded	0	2	3	4	8	1	82
		Excluded (0 °C)	0	2	2	4	9	1	82
		Excluded (2 °C)	0	2	2	4	9	1	82
	Precipitation	Not excluded	0	3	3	4	5	0	85
		Excluded (0 °C)	0	4	3	3	6	0	84
		Excluded (2 °C)	0	4	3	3	6	0	84
FLUXNET2015 D_{PDO}	Temperature	Not excluded	0	5	3	0	3	0	89
		Excluded (0 °C)	0	5	3	0	0	0	92
		Excluded (2 °C)	0	5	3	0	0	0	92
	Precipitation	Not excluded	0	6	0	8	3	5	78
		Excluded (0 °C)	0	6	0	8	3	5	78
		Excluded (2 °C)	0	6	0	8	3	5	78

394 D_{PDO} , timing of onset of decrease in maximum canopy photosynthetic capacity in autumn; D_{LCO} , timing of onset of leaf
 395 coloration in autumn. The relationships between D_{LCO} (or D_{PDO}) and temperature were determined by using a partial
 396 correlation analysis between D_{LCO} (or D_{PDO}) and pre- D_{LCO} (or pre- D_{PDO}) mean daily minimum temperature, with concurrent
 397 total precipitation as the control variable. The relationships between D_{LCO} (or D_{PDO}) and pre- D_{LCO} (or pre- D_{PDO}) precipitation
 398 were determined similarly. Cold events were determined mainly by using a threshold-based method with a daily minimum
 399 temperature of 0 °C or 2 °C. Data in the farthest right column indicate the percentage of area or time-series with a non-
 400 significant correlation.
 401

402 **Table S8.** Percentage of correlations between D_{LCO} or D_{PDO} and each climate factor for each interval of
 403 the partial correlation coefficient.

Climatic factor	Metrics	Interval of the partial correlation coefficient ($P < 0.05$)						$P > 0.05$
		[-1.0, -0.8)	[-0.8, -0.6)	[-0.6, 0)	(0, 0.6]	(0.6, 0.8]	(0.8, 1.0]	
Temperature	FLUXNET2015 D_{PDO}	0	7	0	0	3	0	90
	Satellite D_{LCO}	0	4	3	3	3	0	87
Precipitation	FLUXNET2015 D_{PDO}	0	7	0	0	3	7	83
	Satellite D_{LCO}	0	0	0	0	7	0	93

404 D_{PDO} , timing of onset of decrease in maximum canopy photosynthetic capacity in autumn; D_{LCO} , timing of onset of leaf
 405 coloration in autumn. The relationships between D_{LCO} (or D_{PDO}) and temperature were determined by using a partial
 406 correlation analysis between D_{LCO} (or D_{PDO}) and pre- D_{LCO} (or pre- D_{PDO}) mean daily minimum temperature, with concurrent
 407 total precipitation as the control variable. The relationships between D_{LCO} (or D_{PDO}) and pre- D_{LCO} (or pre- D_{PDO}) precipitation
 408 were determined similarly. Only sites with at least 10 continuous years of valid data for both D_{LCO} and D_{PDO} were included.
 409 Data in the farthest right column indicate the percentage of area or time-series with a non-significant correlation. To make the
 410 satellite D_{LCO} and FLUXNET2015 D_{PDO} more comparable, MOD09A1 with a spatial resolution of 500 m was used for
 411 extracting satellite D_{LCO} .

412

413 **Supplementary Methods**

414 **1 Preparation of high quality 5-day NDVI time series**

415 The quality of the daily surface reflectance data from MOD09CMG was unsatisfactory owing to
 416 cloud contamination (Vermote, 2015), so we used the 5-day maximum value composite approach
 417 (Zhang, 2015), combined with a Savitzky-Golay filter (Cao *et al.*, 2018), to produce a high-quality
 418 NDVI time series before determining D_{LCO} . Details of the data preprocessing are given in the following
 419 text.

420 1) Calculating daily NDVI. We calculated the daily NDVI time series with the quality flag from
 421 surface reflectance in the red and near-infrared bands as $NDVI = (NIR - RED)/(NIR + RED)$. The
 422 quality flags for daily NDVI were derived from the two quality bands (i.e., Internal CM and State QA)
 423 of the reflectance product MOD09CMG (Vermote *et al.*, 2015). We determined four types of conditions
 424 that corresponded to the assigned quality flags: 1) clear, 2) uncertain, 3) snowy, and 4) cloudy (with
 425 deteriorating data quality), according to Cao *et al.* (2018) These were subsequently used in the Savitzky-
 426 Golay filtering (Cao *et al.*, 2018). To be precise, the quality flag was set to “cloudy” if the cloud state in
 427 either Internal CM or State QA was labeled as “yes” or “cloudy or mixed”; the quality flag was set to
 428 “snowy” if the snow/ice flag in State QA was labeled as “yes”; and the quality flag was set to “uncertain”
 429 if the cloud state in State QA was not set (assumed clear). All the other data flags were set to “clear”
 430 (see the index table below). In addition, considering that the NDVI value of a vegetation pixel ranged
 431 from -0.2 to 1.0 , NDVI data outside this range were treated as gaps in the NDVI time series.

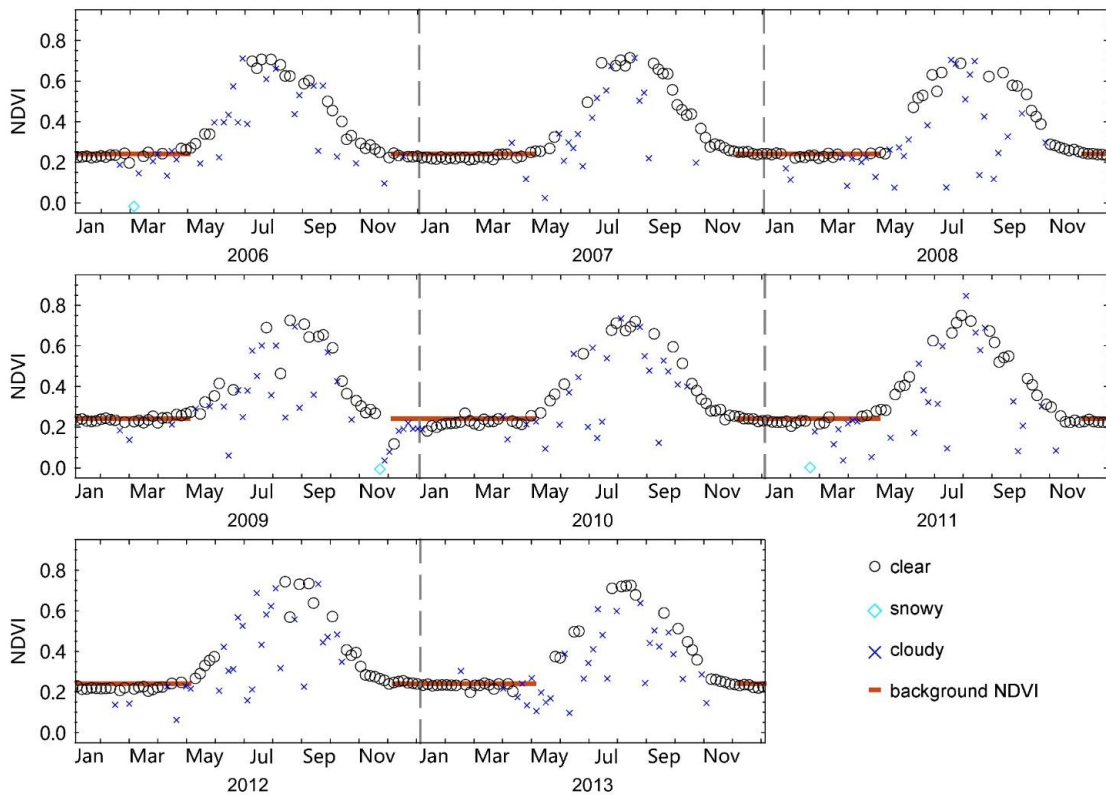
Quality flag of daily NDVI	MOD35 snow/ice flag in State QA	Cloud state in State QA	Cloud state in Internal CM
clear	no	clear	no
uncertain	no	not set (assumed clear)	no
snowy	yes	clear or not set (assumed clear)	no
cloudy	-	cloudy or mixed	-
	-	-	yes

432 “No” and “yes” in the snow/ice flag indicate absence and presence of snow or ice, respectively; “no” and “yes” in the internal
 433 CM indicate absence and presence of cloud, respectively; “-” means no specific snow/ice or cloud state was required.

434 2) Determining the background NDVI value for each pixel. The background value represents the
 435 annual minimum NDVI during winter (December–February), in which NDVI was expected to be stable
 436 for winter deciduous vegetation if there was no snow/ice or cloud contamination. The background NDVI
 437 value was calculated as the mean of high winter NDVI values, because snow/ice or cloud contamination

438 decreases NDVI owing to the uncertainties in the snow/ice and cloud flags (Beck *et al.*, 2006). To obtain
439 high winter NDVI values for a given pixel, we first calculated a time series of winter NDVI higher than
440 0.10 (snow-contaminated NDVI is usually lower than 0.10). The high winter NDVI values were
441 expected to be higher than the 50th percentile of this time series of winter NDVI and lower than the
442 mean + 2SD of this time series of winter NDVI. In some cases, there would be no winter NDVI values
443 higher than 0.10; for these cases the background NDVI value was set at 0.10.

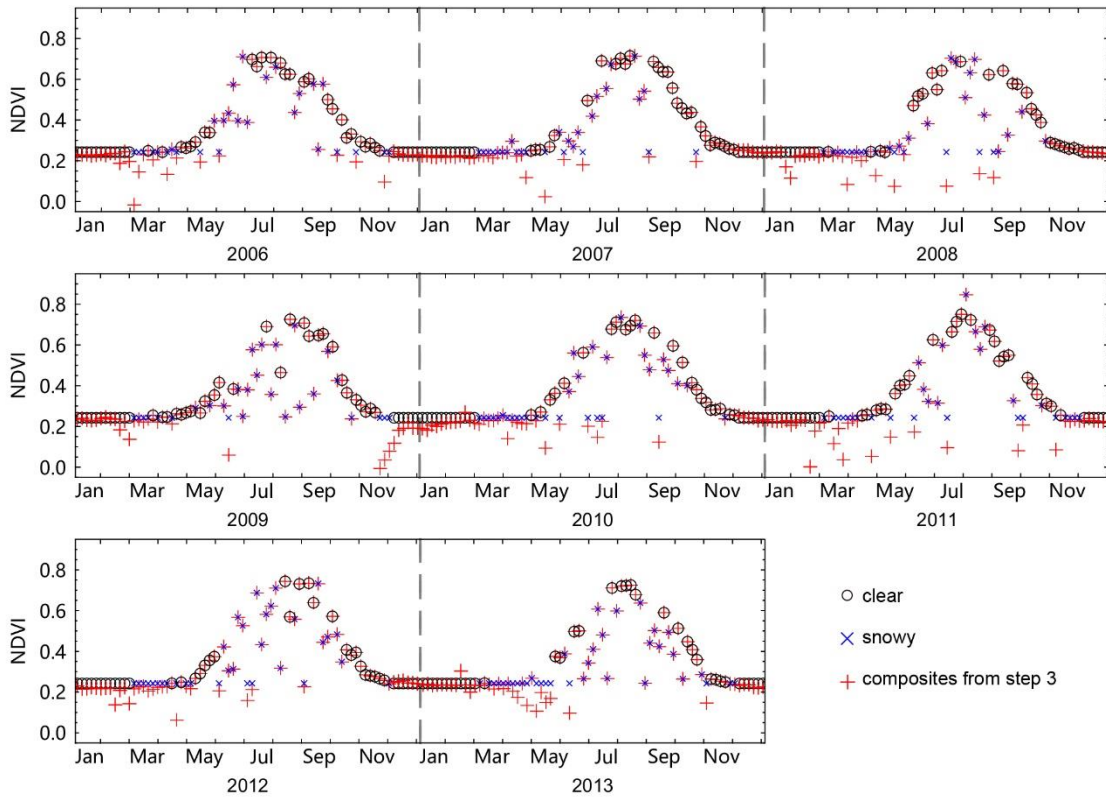
444 3) Compositing the 5-day NDVI time series from daily NDVI time series. The daily NDVI time-
445 series were aggregated to a 5-day composite as follows: if there were one or more NDVI values meeting
446 the quality level (i.e., the quality flag is “clear” in step 1) within the 5-day period, the median value was
447 used as the composite value to reduce noise, and the composite value was flagged as “clear”. If no
448 acceptable NDVI data were found in the 5-day period, the maximum value was used as the composite
449 value (see Figure SM1), and the composite value was flagged as the corresponding daily quality flag of
450 the maximum value.



451

452 **Figure SM1.** An example (31.325°N, 98.125°E) showing composite 5-day NDVI time series from
453 daily NDVI time series.

454 4) Eliminating snow cover contamination in NDVI data. NDVI values in winter (December–
 455 February) were all replaced by the background NDVI value, and their flag was set to “clear”, meaning
 456 that those NDVI values were not changed in the Savitzky-Golay filtering. In the other three seasons
 457 (March–November), the NDVI values lower than this background NDVI value were then substituted for
 458 the latter one (see Figure SM2) and their flag values were set to “cloudy”.



459
 460 **Figure SM2.** An example showing the elimination of snow cover contamination in NDVI data.

461
 462 5) Identifying irregularly high and low NDVI values. Disturbances in surface reflectance data,
 463 which are caused by cloud contamination, bidirectional effects, and data transmission errors, result in
 464 irregularly high and low NDVI values. Most of these irregular NDVI values could be marked by using
 465 the quality flag in step 1. However, because of the uncertainty of the quality flag, there was still a sharp
 466 increase or sudden large decrease of NDVI values flagged as “clear” in the 5-day NDVI profile from
 467 March to November. Because vegetation growth is a continuous process without large increases or
 468 decreases in greenness over a few days, NDVI values that showed sharp decreases or increases were
 469 defined as irregularly low or high NDVI values, respectively, and they were identified by using the

470 shape of the NDVI curve and an outlier detection method.

471 The irregularly low NDVI values were identified by using the shape of the NDVI curve.
472 Assuming that the 5-day NDVI increased or decreased gradually in a seasonal course, for any 5-day
473 NDVI at time t , denoted as $NDVI(t)$, an $NDVI(t)$ was identified as an irregularly low value, if there
474 existed two positive integers k and m satisfying

$$475 \quad NDVI(t) - NDVI(t - k) \leq -k \times (0.15 \times \max NDVI)$$

$$476 \quad NDVI(t) - NDVI(t + m) \leq -m \times (0.15 \times \max NDVI)$$

477 where $1 \leq k \leq 6$, $1 \leq m \leq 6$, and $\max NDVI$ was the 75th percentile of the time series of annual maximum
478 NDVI from 2000 to 2018. In a few cases, there may have been two consecutive irregularly low values,
479 which were identified as follows. Two consecutive NDVI values, $NDVI(t)$ and $NDVI(t + 1)$, were
480 identified as consecutive irregularly low values if they satisfied the following inequalities:

$$481 \quad NDVI(t) - NDVI(t - 1) \leq -1 \times (0.15 \times \max NDVI)$$

$$482 \quad NDVI(t + 1) - NDVI(t - 1) \leq -0.9 \times (0.15 \times \max NDVI)$$

$$483 \quad NDVI(t + 1) - NDVI(t + 2) \leq -2 \times (0.15 \times \max NDVI).$$

484 The irregularly high NDVI values were identified by using the shape of the NDVI curve and an
485 outlier detection method. The NDVI curve shape-based method included two procedures. Procedure 1
486 was to detect non-consecutive irregularly high NDVI values. Assuming that the 5-day NDVI increased
487 or decreased gradually in a seasonal course, an NDVI value at time t , $NDVI(t)$, was identified as an
488 irregularly high value if it satisfied

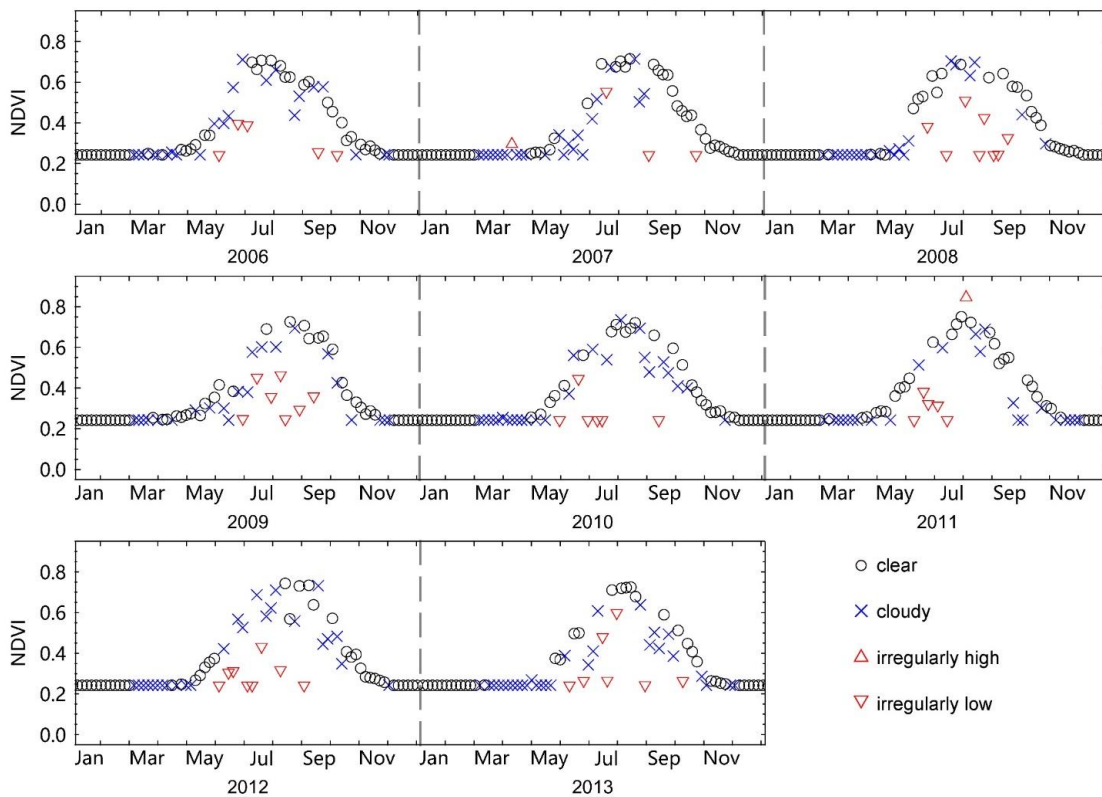
$$489 \quad NDVI(t) \geq 1.15 \times \max\{NDVI(t - 6), NDVI(t - 5), \dots, NDVI(k), \dots, NDVI(t + 6)\}$$

490 where $t - 6 \leq k \leq t + 6$ and $k \neq t$.

491 In some cases, there could be two or more irregularly high NDVI values within 1 month around
492 peak season that could not be detected by using the above algorithm. Such irregularly high NDVI values
493 were identified in Procedure 2, which used the information of a non-consecutive irregularly high NDVI
494 value identified in Procedure 1. We first constructed an array by selecting non-consecutive irregularly
495 high NDVI values in Procedure 1, which were the annual maximum values (denoted as $NDVI_{IHM}$). Then,
496 the NDVI values were identified as irregularly high NDVI values if they were 15% higher than the
497 median value of the array of $NDVI_{IHM}$.

498 Because the NDVI values around the peak season were essential for retrieving D_{LCO} , to be more
 499 robust, the irregularly high NDVI values were also identified by using Grubb's test (Grubbs, 1950). We
 500 first composed an array by using the three highest NDVI values of each year. The outliers in this array
 501 were then detected by using Grubb's test at a significance level of $\alpha = 0.05$. Owing to inter-annual
 502 variations in the annual maximum greenness, the outliers detected by Grubb's test may not necessarily
 503 have been the irregularly high NDVI values. Therefore, in a given year, only outliers that were 15%
 504 higher than the mean of the three highest non-outlier NDVI values for that year were identified as
 505 irregularly high NDVI values. Finally, all the irregularly high NDVI values identified above were used
 506 as irregularly high NDVI values.

507 The figure SM3 gives examples of irregularly low and high NDVI values.



508
 509 **Figure SM3.** An example showing irregularly high and low NDVI values identified in the 5-day
 510 composited NDVI time series.

511
 512 6) Processing the NDVI values flagged as “cloudy”. Because clouds are overestimated by the
 513 cloud flag (Wilson *et al.*, 2014), there were a considerable number of high NDVI values during March–

514 November that were flagged as “cloudy” but that appeared to be reasonable in the seasonal NDVI
515 profile. We detected these NDVI values and promoted their flags to be “uncertain” (“uncertain”
516 indicates a quality higher than “cloudy” but lower than “clear”, see Cao *et al.* (2018) for details). First, a
517 pixel-year was excluded from our study if each of the NDVI values from May to September was either
518 “cloudy” or “irregular”. Second, for NDVI values lower than 90% of their annual range plus the
519 background NDVI value, the NDVI at time t , $NDVI(t)$, was flagged as “uncertain” if it satisfied the
520 following,

$$521 \quad NDVI(t) \geq \max\{NDVI(t-2), NDVI(t-1), NDVI(t), NDVI(t+1), NDVI(t+2)\},$$

522 where $NDVI(t)$ had been flagged as “cloudy”, and $NDVI(t-2)$, $NDVI(t-1)$, $NDVI(t+1)$, and $NDVI(t+2)$
523 had all been flagged as “cloudy” or “irregular”.

524 Moreover,

$$525 \quad NDVI(t) \geq 0.85 \times \max\{NDVI(t-12), NDVI(t-11), \dots, NDVI(t-1)\}$$

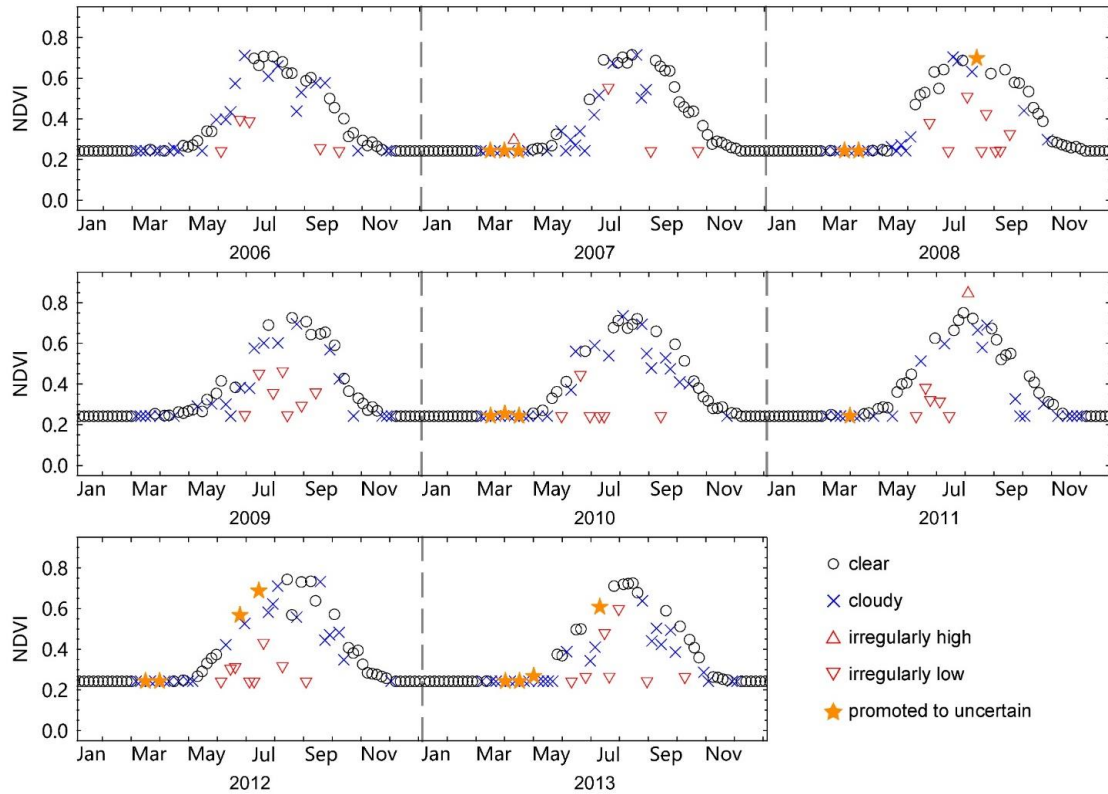
526 for $NDVI(t)$ in an ascending period (i.e., from early March to the time of annual maximum NDVI), and

$$527 \quad NDVI(t) \geq 0.85 \times \max\{NDVI(t+1), NDVI(t+2), \dots, NDVI(t+12)\}$$

528 for $NDVI(t)$ in a descending period (i.e., from the time of annual maximum NDVI to late November).

529 The figure SM4 gives an example of NDVI values that were promoted from “cloudy” to “uncertain”.

530

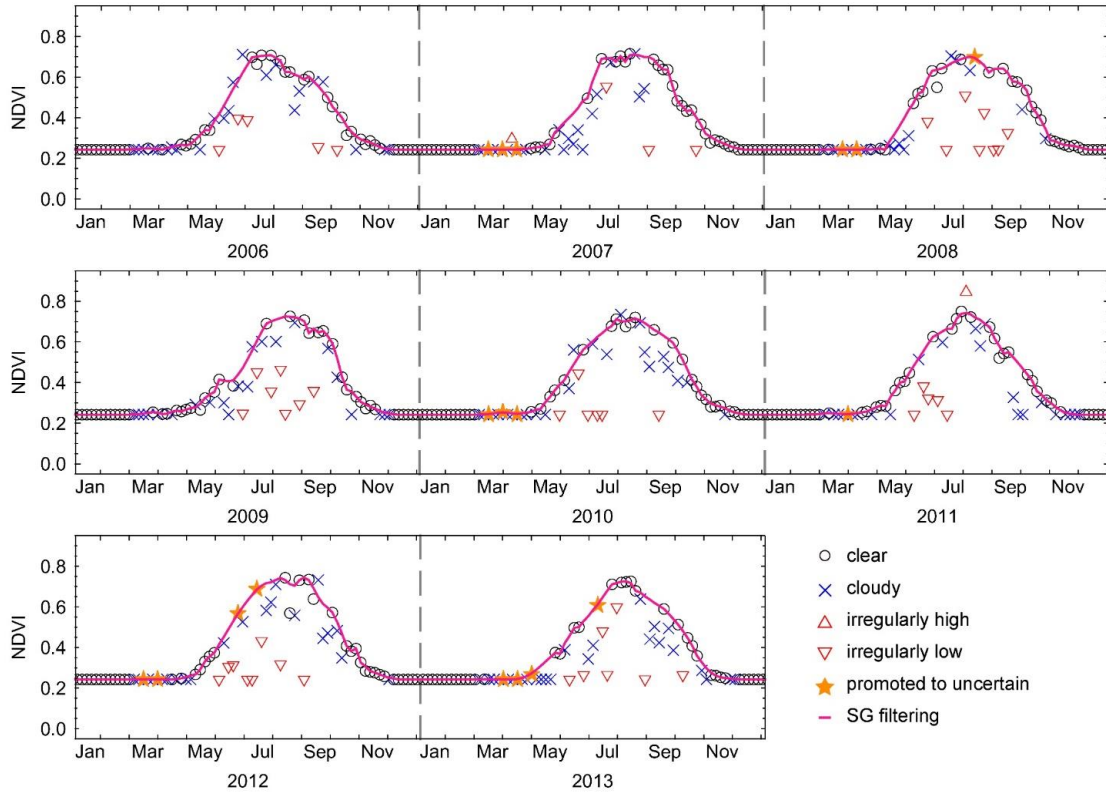


531

532 **Figure SM4.** An example showing NDVI values with flags promoted from “cloudy” to “uncertain”.

533

534 7) Reconstructing 5-day continuous high-quality NDVI time series. Because clouds and poor
 535 atmospheric conditions contaminate NDVI values, we applied a Savitzky-Golay filter to reconstruct a
 536 high-quality NDVI time-series as described by Cao *et al.* (2018) and Shen *et al.* (2014). The source code
 537 of Spatial-Temporal Savitzky-Golay (STSG) is available at [https://github.com/cao-](https://github.com/cao-sre/STSG_IDL_program)
 538 [sre/STSG_IDL_program](https://github.com/cao-sre/STSG_IDL_program) (assessed on 19 December 2018). Before we applied the filter, the “irregular”
 539 quality flags were merged to “cloudy”. In our study, we used the same parameter setting as Cao *et al.*
 540 (2018), except that the half width of the search window and the half width of the smoothing window
 541 were both set to 5. The figure SM5 gives an example of the filtering.



542

543 **Figure SM5.** An example showing the output of SG filtering.

544

545

546

547 **2 Comparison between satellite D_{LCO} and D_{LCO} from PhenoCam dataset**

548 To better match the PhenoCam images, we used the satellite MOD09A1 dataset (collection 6)
549 which has a spatial resolution of 500 m and temporal resolution of 8 days. The dataset was downloaded
550 from <https://modis.ornl.gov/globalsubset/> on March 10, 2021. The PhenoCam dataset V2.0 was
551 downloaded from https://daac.ornl.gov/cgi-bin/dsviewer.pl?ds_id=1674 on August 29, 2020. From the
552 high-frequency (typically, 30 minute) imagery collected over several years, the GCC (green chromatic
553 coordinate) time series of a region-of-interest (ROI) that delineates an area of specific vegetation type
554 was provided by the PhenoCam dataset. The VCI (vegetation contrast index) time series was calculated
555 as the ratio of the green to the sum of the red and blue bands (Zhang *et al.*, 2018). For the comparison
556 between satellite D_{LCO} and D_{LCO} from the PhenoCam dataset, processing steps are as follows:

557 Step 1, the sites for agricultural lands, urban areas, or heterogeneous landscape within the area of
558 a 500 m \times 500 m pixel were excluded by visually examining the images in Google Earth. Then, daily
559 time series were created by calculating the 90th percentile of GCC or VCI for each day. After that, 5-day
560 medium value filtering was used to smooth the short term fluctuations and noises.

561 Step 2, a time series was excluded if there was no data in any consecutive 30 days from annual
562 maximum and to the end of year.

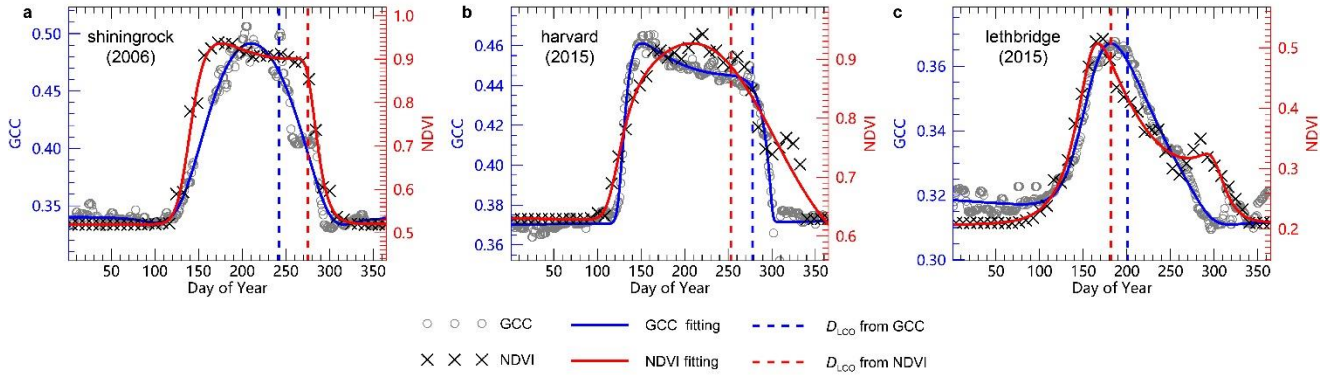
563 Step 3, the annual time series were fitted to a generalized sigmoid function (eq 7 in Klosterman *et al.*
564 al (Klosterman *et al.*, 2014)).

565 Step 4, in many of the sites, there was considerable mismatch between the annual NDVI and GCC
566 (or VCI) trajectories. To remove some of those mismatched annual trajectories, we excluded the site-
567 years for which the date of annual maximum NDVI differed by more than 30 days from that of GCC (or
568 VCI) or the Pearson's correlation coefficient between NDVI and GCC (or VCI) lower than 0.75. In this
569 step, the date of annual maximum NDVI (or GCC, VCI) was determined using 25-day smoothed times
570 series of the fitted curves to eliminate short time variations. The Pearson's correlation coefficient was
571 calculated between fitted daily NDVI and GCC (or VCI) for the period from the date of annual
572 maximum greenness and the date when greenness dropped by 60%. The period for calculating
573 correlation coefficient was determined using the earlier one of the dates of annual maximum NDVI and
574 GCC (or VCI) and the later one of the dates when NDVI and GCC (or VCI) dropped by 60%. This
575 criterion was not applied to deciduous broadleaf forest, because annual maximum of GCC or VCI
576 usually occurred in late May or early June whereas annual maximum of NDVI was usually in late July
577 or early August. After that, we excluded the annual NDVI time series for which the mean NDVI of the

578 31 days period with annual maximum NDVI in the 16th day was less than 1.15 times the mean NDVI of
579 December.

580 The satellite D_{LCO} explained about 80% of the variations in PhenoCam derived D_{LCO} (Fig. 2 in the
581 main text), although the mismatch between the annual NDVI and GCC trajectories leads to large D_{LCO}
582 difference between NDVI and GCC (Figure SM6) or VCI (Figure SM7).

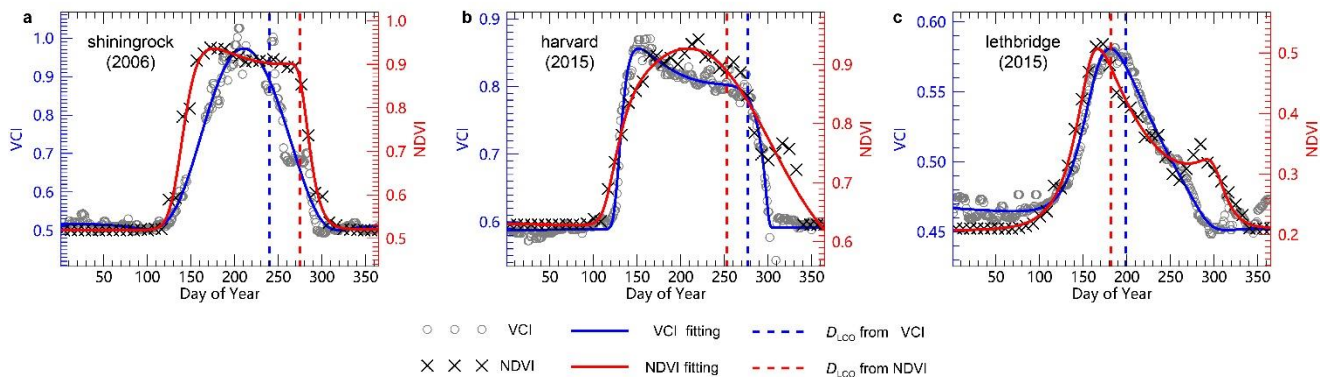
583



584

585 **Figure SM6.** Examples that mismatch between the annual NDVI and GCC trajectories leads to large
586 D_{LCO} difference between NDVI and GCC.

587



588

589 **Figure SM7.** Examples that mismatch between the annual NDVI and VCI trajectories leads to large
590 D_{LCO} difference between NDVI and VCI.

591

592

593 **Supplementary References**

- 594 Aikio, S., Taulavuori, K., Hurskainen, S., Taulavuori, E. & Tuomi, J. (2019) Contributions of day
595 length, temperature and individual variability on the rate and timing of leaf senescence
596 in the common lilac *Syringa vulgaris*. *Tree Physiology*, **39**, 961-970.
- 597 Amiro, B. (2016) FLUXNET2015 CA-Man Manitoba - Northern Old Black Spruce (former
598 BOREAS Northern Study Area). In. FluxNet; University of Manitoba
- 599 Arain, M.A. (2016a) FLUXNET2015 CA-TP4 Ontario - Turkey Point 1939 Plantation White
600 Pine. In. FluxNet; McMaster University
- 601 Arain, M.A. (2016b) FLUXNET2015 CA-TP3 Ontario - Turkey Point 1974 Plantation White
602 Pine. In. FluxNet; McMaster University
- 603 Aurela, M., Tuovinen, J.-P., Hatakka, J., Lohila, A., Mäkelä, T., Rainne, J. & Lauria, T. (2016)
604 FLUXNET2015 FI-Sod Sodankyla. In. FluxNet; Finnish Meteorological Institute
- 605 Beck, P.S.A., Atzberger, C., Høgda, K.A., Johansen, B. & Skidmore, A.K. (2006) Improved
606 monitoring of vegetation dynamics at very high latitudes: A new method using MODIS
607 NDVI. *Remote Sensing of Environment*, **100**, 321-334.
- 608 Bernhofer, C., Grünwald, T., Moderow, U., Hehn, M., Eichelmann, U. & Prasse, H. (2016a)
609 FLUXNET2015 DE-Tha Tharandt. In. FluxNet; TU Dresden
- 610 Bernhofer, C., Grünwald, T., Moderow, U., Hehn, M., Eichelmann, U. & Prasse, H. (2016b)
611 FLUXNET2015 DE-Gri Grillenburg. In. FluxNet; TU Dresden
- 612 Berveiller, D., Delpierre, N., Dufrêne, E., Pontailier, J.-Y., Vanbostal, L., Janvier, B., Mottet, L. &
613 Cristinacce, K. (2016) FLUXNET2015 FR-Fon Fontainebleau-Barbeau. In. FluxNet;
614 CNRS
- 615 Black, T.A. (2016a) FLUXNET2015 CA-Obs Saskatchewan - Western Boreal, Mature Black
616 Spruce. In. FluxNet; The University of British Columbia
- 617 Black, T.A. (2016b) FLUXNET2015 CA-Oas Saskatchewan - Western Boreal, Mature Aspen.
618 In. FluxNet; The University of British Columbia
- 619 Blanken, P. (2016) FLUXNET2015 US-NR1 Niwot Ridge Forest (LTER NWT1). In. FluxNet;
620 University of Colorado
- 621 Böhlenius, H., Huang, T., Charbonnel-Campaa, L., Brunner, A.M., Jansson, S., Strauss, S.H. &
622 Nilsson, O. (2006) CO/FT regulatory module controls timing of flowering and seasonal
623 growth cessation in trees. *Science*, **312**, 1040-1043.
- 624 Cao, R., Chen, Y., Shen, M., Chen, J., Zhou, J., Wang, C. & Yang, W. (2018) A simple method
625 to improve the quality of NDVI time-series data by integrating spatiotemporal
626 information with the Savitzky-Golay filter. *Remote Sensing of Environment*, **217**, 244-
627 257.
- 628 Chen, J. (2016) FLUXNET2015 US-Oho Oak Openings. In. FluxNet; University of Toledo /
629 Michigan State University
- 630 Davidson, H. (1957) *Photoperiodic responses on selected woody ornamental shrubs*. Michigan
631 State University of Agriculture and Applied Science. Department of Horticulture,
- 632 De Ligne, A., Manise, T., Heinesch, B., Aubinet, M. & Vincke, C. (2016) FLUXNET2015 BE-Vie
633 Vielsalm. In. FluxNet; University of Liege - Gembloux Agro-Bio Tech; University catholic
634 of Louvain-la-Neuve
- 635 Desai, A. (2016) FLUXNET2015 US-PFa Park Falls/WLEF. In. FluxNet; University of
636 Wisconsin
- 637 Dolman, H., Van Der Molen, M., Parmentier, F.-J., Marchesini, L.B., Dean, J., Van Huissteden,
638 K. & Maximov, T. (2016) FLUXNET2015 RU-Cok Chokurdakh. In. FluxNet; Vrije

639 Universiteit Amsterdam

640 Downs, R.J. & Borthwick, H.A. (1956) Effects of photoperiod on growth of trees. *Botanical*
641 *Gazette*, **117**, 310-326.

642 Elmore, A.J., Guinn, S.M., Minsley, B.J. & Richardson, A.D. (2012) Landscape controls on the
643 timing of spring, autumn, and growing season length in mid-Atlantic forests. *Global*
644 *Change Biology*, **18**, 656-674.

645 Fennell, A. & Hoover, E. (1991) Photoperiod influences growth, bud dormancy, and cold
646 acclimation in *Vitis labruscana* and *V. riparia*. *Journal of the American Society for*
647 *Horticultural Science. American Society for Horticultural Science*, **116**, 270-273.

648 Fracheboud, Y., Luquez, V., Björkén, L., Sjödin, A., Tuominen, H. & Jansson, S. (2009) The
649 control of autumn senescence in European aspen. *Plant Physiology*, **149**, 1982-1991.

650 Gianelle, D., Cavagna, M., Zampedri, R. & Marcolla, B. (2016a) FLUXNET2015 IT-MBo Monte
651 Bondone. In. FluxNet; Edmund Mach Foundation

652 Gianelle, D., Zampedri, R., Cavagna, M. & Sottocornola, M. (2016b) FLUXNET2015 IT-Lav
653 Lavarone. In. FluxNet; Edmund Mach Foundation

654 Gough, C., Bohrer, G. & Curtis, P. (2016) FLUXNET2015 US-UMB Univ. of Mich. Biological
655 Station. In. FluxNet; Ohio State University; Virginia Commonwealth University

656 Grubbs, F.E. (1950) Sample criteria for testing outlying observations. *Annals of Mathematical*
657 *Statistics*, **21**, 27-58.

658 Hamilton, J.A., El, K.W., Hart, A.T., Runcie, D.E., Arango-Velez, A. & Cooke, J.E. (2016) The
659 joint influence of photoperiod and temperature during growth cessation and
660 development of dormancy in white spruce (*Picea glauca*). *Tree Physiology*, **36**, tpw061.

661 Heide, O.M. (1974) Growth and Dormancy in Norway Spruce Ecotypes (*Picea abies*) I.
662 Interaction of Photoperiod and Temperature. *Physiologia Plantarum*, **30**, 1-12.

663 Heide, O.M. (2001) Photoperiodic control of dormancy in *Sedum telephium* and some other
664 herbaceous perennial plants. *Physiologia Plantarum*, **113**, 332-337.

665 Hörtnagl, L., Eugster, W., Buchmann, N., Paul-Limoges, E., Etzold, S. & Haeni, M. (2016a)
666 FLUXNET2015 CH-Lae Laegern. In. FluxNet; ETH Zurich

667 Hörtnagl, L., Eugster, W., Merbold, L., Buchmann, N., Etzold, S., Haesler, R. & Haeni, M.
668 (2016b) FLUXNET2015 CH-Dav Davos. In. FluxNet; ETH Zurich

669 Howe, G.T., Gardner GHackett, W.P. & Furnier, G.R. (1996) Phytochrome control of short-day-
670 induced bud set in black cottonwood. *Physiologia Plantarum*, **97**, 95-103.

671 Ibrom, A. & Pilegaard, K. (2016) FLUXNET2015 DK-Sor Soroe. In. FluxNet; Technical
672 University of Denmark (DTU)

673 Janssens, I. (2016) FLUXNET2015 BE-Bra Brasschaat. In. FluxNet; University of Antwerp

674 Junttila, O. (1980) Effect of photoperiod and temperature on apical growth cessation in two
675 ecotypes of *Salix* and *Betula*. *Physiologia Plantarum*, **48**, 347-352.

676 Keskitalo, J., Bergquist, G., Gardeström, P. & Jansson, S. (2005) A cellular timetable of autumn
677 senescence. *Plant Physiol*, **139**, 1635-1648.

678 Klosterman, S.T., Hufkens, K., Gray, J.M., Melaas, E., Sonnentag, O., Lavine, I., Mitchell, L.,
679 Norman, R., Friedl, M.A. & Richardson, A.D. (2014) Evaluating remote sensing of
680 deciduous forest phenology at multiple spatial scales using PhenoCam imagery.
681 *Biogeosciences*, **11**, 4305-4320.

682 Knohl, A., Tiedemann, F., Kolle, O., Schulze, E.-D., Kutsch, W., Herbst, M. & Siebicke, L.
683 (2016) FLUXNET2015 DE-Hai Hainich. In. FluxNet; University of Goettingen,
684 Bioclimatology

685 Kramer, P.J. (1936) Effect of variation in length of day on growth and dormancy of trees. *Plant*
686 *Physiology*, **11**, 127-137.

687 Law, B. (2016) FLUXNET2015 US-Me2 Metolius mature ponderosa pine. In. FluxNet; Oregon
688 State University

689 Lund, M., Jackowicz-Korczynski, M. & Abermann, J. (2016) FLUXNET2015 DK-ZaH
690 Zackenberg Heath. In. FluxNet; Aarhus University

691 Mammarella, I., Vesala, T., Keronen, P., Kolari, P., Launiainen, S., Pumpanen, J., Rannik, Ü.,
692 Siivola, E., Levula, J. & Pohja, T. (2016) FLUXNET2015 FI-Hyy Hyytiala. In. FluxNet;
693 University of Helsinki

694 Massman, B. (2016) FLUXNET2015 US-GLE GLEES. In. FluxNet; USDA Forest Service

695 Matteucci, G. (2016) FLUXNET2015 IT-Col Collelongo. In. FluxNet; Istituto di Ecologia e
696 Idrologia Forestale CNR

697 McCaughey, H. (2016) FLUXNET2015 CA-Gro Ontario - Groundhog River, Boreal Mixedwood
698 Forest. In. FluxNet; Queen's University

699 Minerbi, S. & Montagnani, L. (2016) FLUXNET2015 IT-Ren Renon. In. FluxNet; Autonomous
700 Province of Bolzano, Forest Services

701 Misra, G. & Biswal, U.C. (1973) Factors Concerned in Leaf Senescence. I. Effects of Age,
702 Chemicals, Petiole, and Photoperiod on Senescence in Detached Leaves of *Hibiscus*
703 *rosa-sinensis* L. *Botanical Gazette*, **134**, 5-11.

704 Moors, E. & Elbers, J. (2016) FLUXNET2015 NL-Loo Loobos. In. FluxNet; ALTErrA /
705 Wageningen Environmental Research

706 Munger, J.W. (2016) FLUXNET2015 US-Ha1 Harvard Forest EMS Tower (HFR1). In. FluxNet;
707 Harvard University

708 Novick, K. & Phillips, R. (2016) FLUXNET2015 US-MMS Morgan Monroe State Forest. In.
709 FluxNet; Indiana University

710 Oleksyn, J., Tjoelker, M.G. & Reich, P.B. (1992) Growth and biomass partitioning of
711 populations of European *Pinus sylvestris* L. under simulated 50° and 60°N daylengths:
712 evidence for photoperiodic ecotypes. *New Phytologist*, **120**, 561-574.

713 Olmsted, C.E. (1951) Experiments on Photoperiodism, Dormancy, and Leaf Age and
714 Abscission in Sugar Maple. *Botanical Gazette*, **112**, 365-393.

715 Paus, E., Nilsen, J. & Junntila, O. (1986) Bud dormancy and vegetative growth in *Salix-Polaris*
716 as affected by temperature and photoperiod. *Polar Biology*, **6**, 91-95.

717 Rinne, P., Saarelainen, A. & Junntila, O. (1994) Growth cessation and bud dormancy in relation
718 to ABA level in seedlings and coppice shoots of *Betula pubescens* as affected by a short
719 photoperiod, water stress and chilling. *Physiologia Plantarum*, **90**, 451-458.

720 Scott, R. (2016a) FLUXNET2015 US-SRM Santa Rita Mesquite. In. FluxNet; United States
721 Department of Agriculture

722 Scott, R. (2016b) FLUXNET2015 US-Wkg Walnut Gulch Kendall Grasslands. In. FluxNet;
723 United States Department of Agriculture

724 Shen, M., Zhang, G., Cong, N., Wang, S., Kong, W. & Piao, S. (2014) Increasing altitudinal
725 gradient of spring vegetation phenology during the last decade on the Qinghai–Tibetan
726 Plateau. *Agricultural and Forest Meteorology*, **189-190**, 71-80.

727 Šigut, L., Havrankova, K., Jocher, G., Pavelka, M. & Janouš, D. (2016) FLUXNET2015 CZ-BK1
728 Bily Kriz forest. In. FluxNet; Global Change Research Institute CAS

729 Varlagin, A., Kurbatova, J. & Vygodskaya, N. (2016) FLUXNET2015 RU-Fyo Fyodorovskoye.
730 In. FluxNet; A.N. Severtsov Institute of Ecology and Evolution

- 731 Vermote, E.F. (2015) MOD09CMG MODIS/Terra Surface Reflectance Daily L3 Global 0.05Deg
732 CMG V006. In: *NASA EOSDIS Land Processes DAAC*
- 733 Vermote, E.F., Roger, J.C. & Ray, J.P. (2015) MODIS Surface Reflectance User's Guide,
734 Collection 6, Version 1.4. *MODIS Land Surface Reflectance Science Computing*
735 *Facility*,
- 736 Wang, D.Y., Hu, S., Li, Q., Cui, K.M. & Zhu, Y.X. (2002) Photoperiod control of apical bud and
737 leaf senescence in pumpkin (*Cucurbita pepo*) strain 185. *Acta Botanica Sinica*, **44**, 55-
738 62.
- 739 Wilson, A.M., Parmentier, B. & Jetz, W. (2014) Systematic land cover bias in Collection 5
740 MODIS cloud mask and derived products — A global overview. *Remote Sensing of*
741 *Environment*, **141**, 149-154.
- 742 Zhang, X. (2015) Reconstruction of a complete global time series of daily vegetation index
743 trajectory from long-term AVHRR data. *Remote Sensing of Environment*, **156**, 457-472.
- 744 Zhang, X., Jayavelu, S., Liu, L., Friedl, M.A., Henebry, G.M., Liu, Y., Schaaf, C.B., Richardson,
745 A.D. & Gray, J. (2018) Evaluation of land surface phenology from VIIRS data using time
746 series of PhenoCam imagery. *Agricultural and Forest Meteorology*, **256-257**, 137-149.
747